

Advanced Digital Signal Processing for Next-Generation Flexible Optical Networks

by

© *Xiang Lin*, BSc, MEng

Huazhong University of Science and Technology

A thesis submitted to the
School of Graduate Studies
in partial fulfilment of the
requirements for the degree of
Doctor of Philosophy

Faculty of Engineering & Applied Science
Memorial University of Newfoundland

May 2020

St. John's

Newfoundland

Abstract

To keep pace with the rapid expansion in data-exchange traffic around the world, optical networks are anticipated to provide flexibility to maximize utilization of the deployed optical fiber resources. On the other hand, digital signal processing (DSP) has been employed in coherent optical systems to enable 100G and beyond optical fiber networks. The goal of the thesis is to develop advanced DSP techniques for the flexible optical networks.

With the reconfigured modulation formats in the systems, modulation classification (MC) is essential in the DSP to facilitate the sequential compensation modules which are modulation format-dependent. Based on the cumulative distribution function (CDF) of received signal's amplitude, an MC algorithm for M -ary quadrature amplitude modulation (M -QAM) formats with $M = 4, 8, 16, 32,$ and 64 is proposed. Results show that the proposed algorithm achieves accurate classification at optical signal-to-noise ratio (OSNR) of interest and is robust to frequency offset and laser phase noise. Relying on the CDF of received signal's amplitude, a non-data-aided (NDA) OSNR estimation algorithm is developed for coherent optical systems employing multilevel constellations. It outperforms the state-of-the-art NDA algorithm in terms of performance and complexity. Furthermore, a joint OSNR estimation and MC algorithm enabled by support vector machine is designed. Compared to deep neural network-based joint estimation approach, the proposed algorithm achieves better performance with comparable complexity.

In addition, a low-complexity two-stage carrier phase estimation algorithm is proposed for coherent optical systems with 16-QAM format. The proposed algorithm exploits the second power operation instead of the conventional fourth power to remove the modulation phase, which is enabled by constellation partition and rotation. Optical back-to-back experiments and numerical simulations are carried out to evaluate the performance of the algorithm. Results show that, compared with the conventional fourth power-based CPE al-

gorithm, the proposed algorithm provides comparable tolerance to the carrier phase noise, with reduced complexity.

Lastly, a novel transmission scheme is investigated for the open and disaggregated metro coherent optical networks, which impose the requirements for multiple user connectivities on the limited orthogonal frequency resources. Thus, it is desirable to provide connections simultaneously to various users in a non-orthogonal way. A transmission scheme based on the non-orthogonal sparse code multiple access in a digital subcarrier multiplexing is proposed. Compared to power domain-based counterpart, the proposed scheme supports more than 2 users without user pairing and clustering. The feasibility of the proposed scheme is verified through numerical simulations. Three scenarios with 2, 4, and 6 users over 1, 2, and 4 subcarriers, respectively, are considered. Performance evaluations show that in all scenarios, the proposed scheme attains bit error ratio lower than the forward error correction limits with the transmission ranges of interest in metro applications.

Acknowledgements

This thesis means a lot to me. As a relatively “old” PhD student who worked in a different discipline priorly, I would have not be able to finish the thesis without the support from many people. I am very grateful to them.

First of all, I would like to express my deepest gratitude to my supervisor, Prof. Octavia Dobre for her encouragement, trust, and support. She has helped me with research directions identification and research work implementation. Besides this priceless guidance in the academic world, she has shown me how to be a great person in life. Having Prof. Dobre as my PhD supervisor was the luckiest thing in my life. In addition, I would like to thank Adrian Dobre, for the family moments he provided me with.

Many thanks to the co-supervisors: Dr. Cheng Li and Dr. Telex Ngatched. During the program, they have provided many valuable suggestions, which help me significantly. Moreover, I am thankful to Memorial University and the Faculty of Engineering and Applied Science for offering me a scholarship, as well as providing the outstanding research environment and facilities.

I owe thanks to many people who gave me precious advice. I would particularly like to thank the people in Prof. Dobre’s group: Dr. Deyuan Chang, Dr. Oluyemi Omomukuyo, Dr. Shu Zhang, Dr. Abdelkerim Amari, Dr. Stanley Johnson, Dr. Yahia Eldemerdash, Ms. Lori Hogan, and Ms. Suchita Yadav. Many thanks go to my friends in St John’s as well. I enjoyed the time we spent together and thank you for those sweet moments. Specifically, I would like to say thanks to Sunish, Fan, Qingyun, Zijun, and Xinwei. You made St John’s feel like home.

I have to give my final thanks to my family. To them this thesis is dedicated. Thanks to my mother, who has always encouraged me to fulfil my dreams and who supported me wholeheartedly. I would like to thank Yankai for always standing with me in difficult times.

Your love, trust and encouragement have blessed and supported me. Thanks for my parents in law for their generous support. Finally, special thanks to Matthew and Felix. I love you and your smile always makes me stronger.

— Xiang Lin

Co-Authorship Statement

I, Xiang Lin, hold a principle author status for all the manuscript chapters (Chapter 3 - 7) in this thesis. However, each manuscript is co-authored by my supervisors and co-researchers, whose contributions have facilitated the development of this work as described below.

- Paper 1 in Chapter 3: Xiang Lin, Yahia Eldemerdash, Octavia A. Dobre, Shu Zhang, Cheng Li, “Modulation classification using received signal’s amplitude distribution for coherent receivers,” *IEEE Phontonic Technology Letter*, Vol. 29, no. 21, pp. 1872-1875, Nov. 2017.

I was the primary author, with authors 2 - 5 contributing to the idea, its formulation and development, and refinement of the presentation.

- Paper 2 in Chapter 4: Xiang Lin, Octavia A. Dobre, Oluyemi Omomukuyo, Yahia Eldemerdash, Shu Zhang, Cheng Li, “OSNR estimation algorithm for higher-order modulation formats in coherent optical systems,” *IEEE/OSA Asia Communications and Photonics Conference 2017*, Paper Su2A, Nov. 2017.

I was the primary author, with authors 2 - 5 contributing to the idea, its formulation and development, and refinement of the presentation.

- Paper 3 in Chapter 4: Xiang Lin, Octavia A. Dobre, Telex M. N. Ngatched, Cheng Li, “A non-data-aided OSNR estimation algorithm for coherent optical fiber communication systems employing multilevel constellations,” *IEEE/OSA Journal of Lightwave Technology*, Vol. 37, no. 15, pp. 3815 - 3825, Aug. 2019.

I was the primary author, with authors 2 - 4 contributing to the idea, its formulation and development, and refinement of the presentation.

- Paper 4 in Chapter 5: Xiang Lin, Octavia A. Dobre, Telex M. N. Ngatched, Yahia El-demerdash, Cheng Li, “Joint modulation classification and OSNR estimation enabled by support vector machine,” IEEE Phontonic Technology Letter, vol. 30, no.24, pp. 2127 - 2130, Dec 2018.

I was the primary author, with authors 2 - 5 contributing to the idea, its formulation and development, and refinement of the presentation.

- Paper 5 in Chapter 6: Xiang Lin, Octavia A. Dobre, Telex M. N. Ngatched, Cheng Li, “A reduced-complexity carrier phase estimation algorithm for 16-QAM coherent optical systems,” under preparation.

I was the primary author, with authors 2 - 4 contributing to the idea, its formulation and development, and refinement of the presentation.

- Paper 6 in Chapter 7: Xiang Lin, Octavia A. Dobre, Telex M. N. Ngatched, Cheng Li, “Introducing sparse code multiple access for metro coherent optical networks,” under preparation.

I was the primary author, with authors 2 - 4 contributing to the idea, its formulation and development, and refinement of the presentation.

Xiang Lin

Date

Table of Contents

Abstract	ii
Acknowledgements	iv
Co-Authorship Statement	vi
Table of Contents	viii
List of Tables	xii
List of Figures	xiv
Acronyms	xvii
1 Introduction	1
1.1 Research Motivation	1
1.2 Thesis Outline	4
1.3 Published and Submitted Work	7
2 Review of Digital Coherent Receivers	9
2.1 Coherent Detection	9
2.2 Digital Coherent Receiver	12

2.3	Subsystems of Digital Coherent Receivers	13
2.3.1	IQ Imbalance Compensation	15
2.3.2	Resampling	15
2.3.3	Static Equalization	15
2.3.3.1	Time Domain Equalizer	16
2.3.3.2	Frequency Domain Equalizer	17
2.3.4	Timing Recovery	17
2.3.5	Adaptive Equalizer	17
2.3.5.1	Constant Modulus Algorithm	18
2.3.5.2	Radius Directed Equalizer	19
2.3.6	Frequency Offset Estimation and Compensation	20
2.3.7	Carrier Phase Recovery	21
2.3.8	Symbol Decision	21
2.4	Concluding Remark	21
3	Modulation Classification Using Received Signal's Amplitude Distribu-	
	tion for Coherent Optical Receivers	22
3.1	Background	22
3.2	Proposed Algorithm	23
3.2.1	Extracted Discriminating Feature	23
3.2.2	CDF-based MC Algorithm	26
3.3	Performance Evaluation	28
3.3.1	Experiments and Results	28
3.3.2	Further Investigations with Numerical Simulations	30
3.4	Summary	35

4	OSNR Estimation for Coherent Optical Receivers Employing Multi-level Constellations	36
4.1	Background	36
4.2	Principle of Operation	38
4.2.1	System Model	38
4.2.2	OSNR and SNR	39
4.2.3	Proposed Estimation Algorithm	40
4.3	Estimation Error Analysis and CRLB on the Variance of the Proposed Estimator	43
4.3.1	Measurement Error of the Empirical CDF	43
4.3.2	Estimation Error Analysis	43
4.3.3	CRLB on the Variance of the Proposed Estimator	45
4.4	Numerical Investigations and Discussion	46
4.4.1	Discussion on the CRLB	47
4.4.2	Convergence of the Newton's Method	49
4.4.3	Selection of z	54
4.4.4	Performance vs. SNR	54
4.4.5	Performance vs. Number of Observed Samples	55
4.5	Numerical Results and Discussions for Nyquist WDM System	55
4.6	Complexity Analysis	61
4.7	Feasibility to PCS Systems and TDHM Systems	63
4.8	Summary	64
5	Joint Modulation Classification and OSNR Estimation for Coherent Optical Systems	65
5.1	Background	65

5.2	Proposed Algorithm	67
5.3	Performance Evaluation	70
5.3.1	Simulation Results and Discussion	70
5.3.2	Experimental Results and Discussion	78
5.3.3	Complexity	79
5.4	Conclusion	80
6	Carrier Phase Estimation for Coherent 16-QAM Systems	81
6.1	Background	81
6.2	Proposed Algorithm	82
6.2.1	QPSK Partition for 16-QAM	83
6.2.2	Proposed Two-stage CPE Algorithm for 16-QAM	83
6.3	Performance Evaluation	86
6.3.1	Simulation Results	86
6.3.2	Experimental Results	88
6.4	Complexity Analysis	90
6.5	Summary	90
7	Flexible Transmission Scheme for Optical Metro Networks	92
7.1	Introduction	92
7.2	Principle of Operation	94
7.2.1	Proposed Scheme	94
7.2.2	Codebook Design	95
7.2.3	DSP Subsystems in the Receiver	97
7.2.4	MPA Detection	99
7.3	Performance Evaluation	102

7.4	Summary	105
8	Conclusion	106
8.1	Summary	107
8.2	Future Directions of Research	108
8.2.1	Effective SNR Estimation	108
8.2.2	SCMA Codebook Design	109
	Appendix	110
	References	114

List of Tables

3.1	Required OSNR (dB) for 100% successful classification.	34
3.2	Computational cost for the proposed algorithm and one of its counterparts.	34
4.1	Complexity for the proposed algorithm and M2M4.	62
4.2	Complexity with typical values for the proposed algorithm and M2M4.	62
5.1	Parameters of optimized DNNs.	72
5.2	Experimental results for MC.	78
6.1	Optimal block lengths at SNR = 16 dB.	88
6.2	Complexity comparison for the CPE algorithms.	90

List of Figures

2.1	Diagram of an optical receiver with coherent detection.	10
2.2	Diagram of a homodyne receiver with phase diversity.	11
2.3	Diagram of a digital coherent receiver with polarization and phase-diversity homodyne detection.	13
2.4	The subsystems of DSP in coherent optical receivers.	14
2.5	The butterfly structure of an adaptive equalizer.	18
3.1	DSP structure including the MC subsystem.	24
3.2	Constellations of M -ary QAM formats affecting by frequency offset and laser phase noise ($M = 4, 8, 16, 32, 64$).	25
3.3	CDFs for M -ary QAM signals with an OSNR of 30 dB.	26
3.4	Experimental B2B system setup.	28
3.5	Probability of correct classification vs. SNR (bottom) and OSNR (top) ob- tained from experiments.	29
3.6	Probability of correct classification vs. SNR (bottom) and OSNR (top) ob- tained from simulations.	31
3.7	Probability of correct classification vs. number of samples obtained from simulations.	31
3.8	Probability of correct classification vs. launch power.	33

4.1	CRLB for different QAMs and SNRs.	47
4.2	CDFs for two QAM formats with different SNRs.	48
4.3	Convergence behavior for the four QAM modulation formats.	51
4.4	Choice of location by investigating derivative with respect to z	53
4.5	OSNR estimation performance versus SNR.	56
4.6	OSNR estimation performance versus number of observed samples.	57
4.7	Simulation setup for Nyquist WDM system. Tx: transmitter; PBC: polarization beam combiner; IQM: in-phase quadrature modulator; MUX: multiplexer.	58
4.8	OSNR estimation error (dB) versus launch power. CS: channel spacing.	60
4.9	Constellations for TDHM with 4-QAM and 16-QAM.	64
5.1	DSP structure including the joint MC and OSNR estimation subsystem.	67
5.2	CDFs for different modulation formats and OSNRs.	68
5.3	SVM-based classifier and regressor.	68
5.4	Illustration of the 5-fold cross validation.	71
5.5	Correct modulation classification rate vs. OSNR.	72
5.6	Mean of estimated OSNR vs. actual OSNR.	73
5.7	Impact of residual CD on CDF.	75
5.8	MC performance when the residual CD is 100 ps/nm.	76
5.9	OSNR estimation performance when the residual CD is 100 ps/nm.	76
5.10	The OSNR estimation error when modulation misclassification occurs.	77
5.11	Experimental results for OSNR estimation.	78
6.1	Illustrative diagram for the proposed CPE algorithm.	84
6.2	Principle of the proposed two-stage algorithm.	85

6.3	SNR versus linewidth-symbol duration product at $\text{BER} = 10^{-2}$ for different CPE algorithms.	87
6.4	The BER vs. OSNR for different CPE algorithms.	89
7.1	System model for the proposed transmission scheme.	97
7.2	The structure of the decision-directed adaptive equalizer.	99
7.3	Factor graph of MPA with 2 function nodes and 4 resources nodes.	101
7.4	Simulation results for 2 users.	103
7.5	Simulation results for 4 users.	104
7.6	Simulation results for 6 users.	104

List of Acronyms and Abbreviations

ADC	analog-to-digital converter
ASE	amplified spontaneous emission
AWG	arbitrary waveform generator
AWGN	additive white Gaussian noise
B2B	back-to-back
BER	bit error rate
BPS	blind phase search
CD	chromatic dispersion
CDF	cumulative distribution function
CFO	carrier frequency offset
CMA	constant modulus algorithm
CPE	carrier phase estimation
CRLB	Cramer-Rao lower bound
DA	data-aided
DAC	digital-to-analog converter
DNN	deep neural network
DSP	digital signal processing
ECL	external cavity lasers
EDFA	erbium doped fiber amplifier
EON	elastic optical network
FDE	frequency domain equalizer
FEC	forward error correction
FFT	fast Fourier transform

FIR	finite impulse response
FN	function node
FOE	frequency offset estimation
FWM	four wave mixing
GSOP	Gram-Schmidt orthogonalization procedure
HD	hard decision
ICR	integrated coherent receiver
IF	intermediate frequency
IP	internet protocol
IFFT	inverse fast Fourier transform
IQ	in-phase-quadrature
LLR	log-likelihood-ratio
LMS	least mean squares
LO	local oscillator
LPF	low-pass filter
M2M4	second-order moment and fourth-order moment
MAP	maximum a posterior
MC	modulation classification
ML	machine learning
MPA	message passing algorithm
MSE	mean square error
MUX	multiplexer
NDA	non-data-aided
NF	noise figure

NLI	non-linear interference
NOMA	non-orthogonal multiple access
OBPF	optical bandpass filter
OPM	optical performance monitoring
OSA	optical spectrum analyzer
OSNR	optical signal-to-noise ratio
PBS	polarization beam splitter
PC	polarization controller
PCS	probabilistic constellation shaping
PDM	polarization division multiplexing
PMD	polarization mode dispersion
QAM	quadrature amplitude modulation
QPSK	quadrature phase-shift-keying
RDE	radius directed equalizer
ROADMs	reconfigurable optical add-drop multiplexers
RRC	root raised cosine
SCM	subcarrier multiplexing
SCMA	sparse code multiple access
SD	soft decision
SE	spectral efficiency
SNR	signal-to-noise ratio
SOP	state of polarization
SSMF	standard single mode fiber
SVC	support vector classifier

SVM	support vector machine
SVR	support vector regressor
TDE	time domain equalizer
TDHM	time domain hybrid modulation
TIA	trans-impedance amplifier
TS	training sequence
VN	variable node
VOA	variable optical attenuator
VVPE	Viterbi-Viterbi phase estimation
WDM	wavelength-division multiplexing

Chapter 1

Introduction

1.1 Research Motivation

The influence of Internet on all aspects of today's society is unchallengeable: the fast expansion of bandwidth-hungry applications across all areas (e.g., social networking, cloud computing, and virtual reality) is profoundly shaping the world. The growing Internet traffic generated by such applications is prompting an unprecedented demand for bandwidth. According to Cisco's recent white paper, the network traffic will increase nearly three-fold over the next three years [1]. Optical fiber has demonstrated its incomparable superiority over other media in terms of capacity and transmission reach to support data transmission. Dated back to 1970, the first low-loss silica fiber was fabricated and the era of optical fiber communications started [2,3]. The early optical fiber communication systems suffered slow progress owing to low efficient opto-electronical regeneration in a span-by-span way. Since 1990s, the cost-effective wavelength-division multiplexing (WDM) technique significantly boosted the transmission capacity, thanks to the advent of wide-band optical fiber amplifiers [4,5]. Along with the rise of WDM systems, optical networking and resource management emerged and improved the system efficiency dramatically. This situation was

driven by the fact that the capacity of WDM systems remarkably exceeded that of electronic devices such as switches and routers. Reconfigurable optical add-drop multiplexing (ROADM) was introduced to incorporate the functions of aggregating, disaggregating, and switching signal path in the optical domain [6, 7]. By 1997, commercial WDM systems achieved an aggregate capacity of 40 Gb/s consisting of sixteen 2.5 Gb/s wavelengths [8]. Afterwards, optical fiber communication systems faced a slow-down in capacity increase because the bandwidth of wide-band optical amplifiers has been used to a maximum possible extent and the available optical bandwidth had been completely saturated. Since 2000s, the commercialization of high speed analog-to-digital converters (ADCs) and digital-to-analog converters (DACs) paved the way to a new era of optical fiber communications: coherent optical systems. With the help of the local oscillator (LO), the signal can be down-converted to baseband and the amplitude and phase information of the signal can be acquired. Combined with polarization division multiplexing (PDM) technique, the spectral efficiency (SE) is increased by a factor of 4 when compared to direct detection systems. It is worth mentioning that digital signal processing (DSP) plays an essential role in this context, since it is the foundation for fiber channel impairment compensation, frequency and phase synchronization, and polarization demultiplexing [9]. Although coherent optical systems involve higher cost and receiver complexity due to the requirements of one more laser at the receiver and powerful DSP, they have attracted very intensive attentions from both academic and industrial sides for their outstanding benefits [10–12]. A 40 Gb/s coherent transmission system employing polarization-division multiplexing quadrature phase-shift-keying (PDM-QPSK) modulation format was demonstrated by Nortel in 2008, where DSP was used to compensate chromatic dispersion and polarization effects [12]. The optical communications systems progressively evolved into 100 Gb/s shortly and were widely deployed commercially, most of which were in long-haul networks [13–15]. The community then focused on more

complex, bandwidth-efficient solutions to increase capacity and achieve higher SE, such as higher-order modulation formats and faster-than-Nyquist signaling [16–18]. For a given system bandwidth, higher SE is mainly achieved by employing higher-order quadrature amplitude modulation (QAM) formats. Ideally, $2\log_2(M)$ bits per symbol can be carried on the M -QAM format. In order to achieve an adaptation of SE with a much finer granularity, probabilistic constellation shaping (PCS) has been proposed very recently [19–23]. In PCS systems, higher energy symbols are sent less frequently than lower energy ones. A commercial long-haul C + L-band optical fiber PCS system has been reported; the system consists of 192 channels and each channel is up to 250 Gb/s on a 50-GHz grid, leading to an aggregate capacity of about 48 Tb/s with an SE of 5 bit/s/Hz [22].

To date, coherent optical systems with DSP techniques have dominated long-haul optical transmission networks and are extending their domination to optical metro networks and even short-reach data center interconnect [24]. However, the tremendous investment cost for optical fiber infrastructure obliges the utilization of current networks resource to maximum extent. In such a context, flexible optical networks or elastic optical networks (EON) are considered as a promising solution. Specifically, ROADMs, adaptive grid, flexible modulation format, and bandwidth have been considered to achieve high efficient utilizations of the current network capacity [25]. The dynamic feature of EON emphasizes the importance of estimating various optical network transmission parameters, such as modulation format and optical signal-to-noise ratio (OSNR) [26]. On one hand, M -QAM formats are widely used in coherent optical fiber systems, due to their high SE and compatibility to high speed DAC. This makes classification of different QAM formats very important. On the other hand, optical amplifiers like erbium-doped fiber amplifier (EDFA) are employed in optical links to compensate for the transmission power loss over long distances. However, EDFA introduces amplified spontaneous emission (ASE) noise into the optical signal.

OSNR quantifies the impact of ASE noise and is thus an important parameter describing the signal quality. Successful modulation classification (MC) and OSNR estimation play a pivotal role in EON.

In addition, the DSP design becomes more challenging as the modulation format evolves from PDM-QPSK to higher-order QAM formats. For example, in QPSK-based systems, carrier phase can be efficiently estimated by the feed-forward Viterbi-Viterbi algorithm, which employs the rotational symmetry of QPSK constellations to map onto a single point of the in-phase-quadrature (IQ) plane when raised to the 4th power (an operation known as modulation phase removal). Unfortunately, higher-order QAM formats do not show such property. Thus, advanced carrier phase estimation (CPE) algorithms for higher-order QAM formats in terms of good performance and low-complexity are desired [27].

Lastly, researches on providing high diversity and flexible solutions for optical metro network have attracted interest recently [28]. Metro-access and metro-regional applications, such as data center interconnect, mobile transport, and enterprise connectivity services, prefer open, flexible, and disaggregated systems. This is in line with the general perception that service providers are more willing to trade performance for interoperability and cost savings. Other than transmitting data over orthogonal resources, non-orthogonal transmission schemes are favored, as they can improve the flexibility of time-frequency resources utilization.

1.2 Thesis Outline

The main objective of this thesis is to investigate advanced DSP techniques for coherent systems in flexible optical networks. On the basis of coherent optical systems, whose concept is introduced briefly in Chapter 2, two categories of work has been performed. The former is related to parameter estimation and is covered in Chapters 3 to 6, while the latter is on

a novel flexible transmission scheme, and is covered in Chapter 7. Each chapter is detailed as follows:

In Chapter 2, the digital coherent receiver and each subsystem is reviewed, respectively. After giving an overview of the subsystems, DSP algorithms widely employed in the subsystems are introduced. The algorithms are required to overcome the optical front-end imperfections, compensate transmission impairments such as chromatic dispersion (CD) and polarization mode dispersion (PMD), and synchronize the carrier frequency offset (CFO) and carrier phase.

In Chapter 3, an MC algorithm is proposed for coherent optical receivers, which is based on the received signal's amplitude. The proposed algorithm classifies the modulation format from several possible candidates by differentiating the cumulative distribution function (CDF) of their normalized amplitudes. The candidate with the most similar CDF to the received signal is selected. The measure of similarity is the average distance between these CDFs. Five commonly used QAM formats are considered. Optical back-to-back (B2B) experiments and extended simulations are carried out to investigate the performance of the proposed algorithm. Results show that the proposed algorithm achieves accurate classification at OSNR of interest. Furthermore, it does not require carrier recovery.

In Chapter 4, a novel non-data-aided (NDA) OSNR estimation algorithm is proposed, which provides enhanced performance for coherent optical systems employing multilevel constellations. The proposed algorithm utilizes the empirical CDF of the signal's amplitude to extract the information on the noise variance. Analytical and extensive simulation results show the feasibility and advantages of the algorithm. For the studied systems employing multilevel constellations such as 8-QAM, 16-QAM, 32-QAM, and 64-QAM, the proposed algorithm attains the derived Cramér-Rao lower bound. Further, it achieves a lower mean square error with significantly lower complexity when compared to the conven-

tional moment-based NDA estimation approach. Moreover, the impact of fiber nonlinearity is investigated with a 5-channel Nyquist wavelength division multiplexing system, and the proposed algorithm outperforms the moment-based counterpart.

In Chapter 5, a support vector machine (SVM)-based algorithm is proposed to jointly classify the modulation format and estimate the OSNR, by adopting the amplitude's CDF as feature. Three commonly-used QAM formats are considered. Numerical simulations have been carried out in the OSNR ranges from 5 dB to 30 dB, and results show that the proposed algorithm achieves a very good MC performance, as well as high OSNR estimation accuracy with a maximum estimation error of 0.8 dB. Optical B2B experiments are also conducted in OSNR ranges of interest. A 99% average correct MC rate is attained, and mean OSNR estimation errors of 0.38 dB, 0.68 dB, and 0.62 dB are observed for 4-QAM, 16-QAM, and 64-QAM, respectively. Furthermore, compared with neural networks-based joint estimation algorithm, the proposed algorithm attains better performance with comparable complexity.

In Chapter 6, a low-complexity two-stage CPE algorithm for coherent optical systems with 16-QAM is proposed. The proposed algorithm uses the second power operation instead of the conventional fourth power to remove the modulation phase, which is enabled by constellation partition and rotation. Simulations and optical B2B experiments are carried out to investigate the performance of the proposed algorithm. Results show that, compared with the conventional fourth power-based CPE algorithm, the proposed algorithm provides a comparable performance with reduced complexity.

In Chapter 7, a transmission scheme based on the non-orthogonal sparse code multiple access technique in a digital subcarrier multiplexing system is proposed. Compared to the power domain-based counterpart, the proposed scheme supports more than 2 users without user pairing and clustering. The feasibility of the proposed scheme is verified through

numerical simulations. Three scenarios with 2, 4, and 6 users over 1, 2, and 4 subcarriers, respectively, are considered. Performance evaluations show that in all scenarios, the bit error rate (BER) is lower than the forward error correction limits with the transmission ranges of interest in metro applications. The proposed scheme is helpful to avoid large buffer and long connection waiting time by providing connections simultaneously to various users in a non-orthogonal way.

In Chapter 8, conclusions are reached by presenting a summary of the main findings, as well as possible future research topics.

1.3 Published and Submitted Work

- **Journal Articles**

- [J1] X. Lin, O. Dobre, T. Ngatched, C. Li, “A non-data-aided OSNR estimation algorithm for coherent optical fiber communication systems employing multilevel constellations,” *J. Lightw. Technol.*, 2019.
- [J2] A. Amari, X. Lin, O. Dobre, R. Venkatesan, A. Alvarado, “A machine learning-based detection technique for optical fiber nonlinearity mitigation,” *IEEE Photon. Technol. Lett.*, 2019.
- [J3] X. Lin, O. Dobre, T. Ngatched, Y. Eldemerdash, C. Li, “Joint modulation classification and OSNR estimation enabled by support vector machine,” *IEEE Photon. Technol. Lett.*, 2018.
- [J4] X. Lin, Y. Eldemerdash, O. Dobre, S. Zhang, C. Li, “Modulation classification using received signal’s amplitude distribution for coherent receivers,” *IEEE Photon. Technol. Lett.*, 2017.
- [J5] S. Zhang, D. Chang, O. Dobre, O. Omomukuyo, X. Lin, R. Venkatesan, “Training

symbol-based equalization for quadrature duobinary PDM-FTN systems,” *IEEE Photon. Technol. Lett.*, 2017.

- [J6] D. Chang, O. Omomukuyo, X. Lin, S. Zhang, O. Dobre, R. Venkatesan, “Robust faster-than-Nyquist PDM-mQAM systems with Tomlinson–Harashima precoding,” *IEEE Photon. Technol. Lett.*, 2016.

• **Conference Articles**

- [C1] A. Amari, X. Lin, O. Dobre, R. Venkatesan, A. Alvarado, “Machine learning-based detection for fiber nonlinearity mitigation,” in *Proc. IEEE ICTON*, 2019.
- [C2] S. Zhang, O. Omomukuyo, O. Dobre, X. Lin, D. Chang, “Training-aided joint frame and frequency synchronization for THP FTN coherent optical systems,” in *Proc. IEEE ICTON*, 2018.
- [C3] X. Lin, O. Dobre, O. Omomukuyo, Y. Eldemerdash, C. Li, “OSNR estimation algorithm for higher-order modulation formats in coherent optical systems,” in *Proc. OSA ACP*, 2017.

Chapter 2

Review of Digital Coherent Receivers

As mentioned in the previous chapter, coherent optical systems have attracted intensive attention due to their high SE and tolerance to fiber channel impairments such as dispersion and nonlinearity [29]. In this chapter, the structure of digital coherent receivers is briefly discussed. To begin with, the concept of coherent detection is introduced.

2.1 Coherent Detection

An optical receiver employing coherent detection is shown in Fig. 2.1. After passing the polarization controller (PC), the optical signal, E_s , enters a 3-dB coupler; while the other input of the coupler connects to a continuous-wave optical laser, which is the LO. Without loss of generality, it is assumed that the state of polarization (SOP) of the transmitted signal and the LO are aligned. The two incident electric field for the signal and LO are

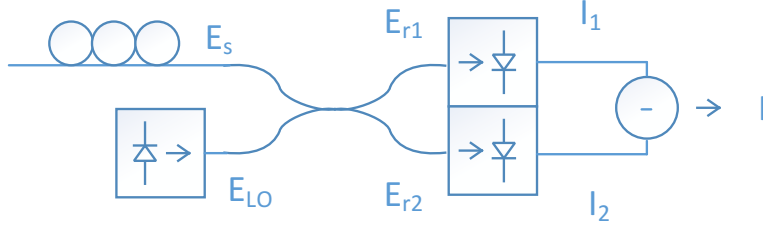


Fig. 2.1: Diagram of an optical receiver with coherent detection.

given by

$$\begin{aligned}
 E_s(t) &= \sqrt{P_s} \exp(j(\omega_s t + \phi_s(t))), \\
 E_{LO}(t) &= \sqrt{P_{LO}} \exp(j(\omega_{LO} t + \phi_{LO}(t))),
 \end{aligned} \tag{2.1}$$

where P_s and P_{LO} are the powers of the signal and the LO, respectively; ω_s and ω_{LO} are the angular frequencies of the signal and the LO, respectively; ϕ_s and ϕ_{LO} are the phases of the signal and the LO, respectively. The 3-dB optical coupler introduces a 180° phase shift between the two output ports. The electric fields incident on the upper and lower photodiodes are given by

$$\begin{aligned}
 E_{r1} &= \frac{1}{\sqrt{2}}(E_s + E_{LO}), \\
 E_{r2} &= \frac{1}{\sqrt{2}}(E_s - E_{LO}).
 \end{aligned} \tag{2.2}$$

The balanced detector output is then calculated as

$$\begin{aligned}
 I(t) &= I_1(t) - I_2(t) \\
 &= 2R\sqrt{P_s(t)P_{LO}(t)} \cos(\omega_{IF}t + \phi_s(t) - \phi_{LO}(t)),
 \end{aligned} \tag{2.3}$$

where R is the responsivity of the photodiode, $\omega_{IF} = |\omega_s - \omega_{LO}|$ is the intermediate frequency (IF). If $\omega_{IF} = 0$, the current is

$$I(t) = 2R\sqrt{P_s(t)P_{LO}(t)} \cos(\phi_s(t) - \phi_{LO}(t)), \tag{2.4}$$

which implies that the receiver measures the inner product between the signal phasor and the LO phasor. This kind of coherent receiver is called *homodyne* receiver. In general, an optical phase lock loop is required to ensure that the LO phase tracks the signal phase. However, the implementation is complicated in practice. In addition, only the cosine component or the projection of the signal on the LO is available, and thus, the *homodyne* receiver cannot extract full information of the signal.

In order to obtain the sine component, another LO input with 90° shift is required. By separating the signal and the LO into two branches respectively and adding a 90° shift on one branch, both in-phase and quadrature components can be detected. This scheme is shown in Fig. 2.2. Accordingly, the four electric field outputs are given by

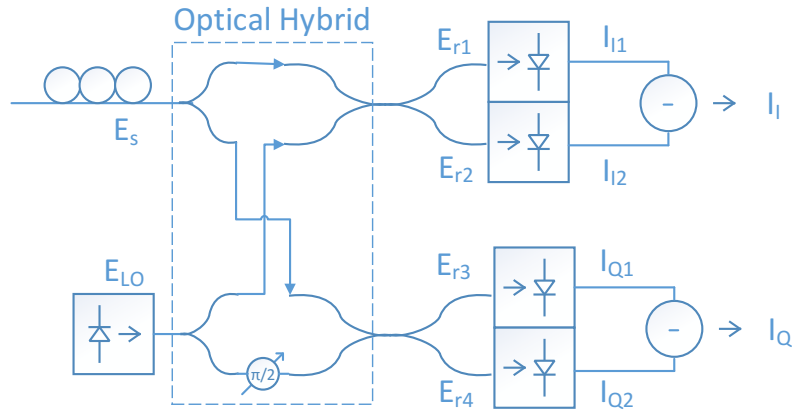


Fig. 2.2: Diagram of a homodyne receiver with phase diversity.

$$\begin{aligned}
 E_{r1} &= \frac{1}{\sqrt{2}}(E_s + E_{LO}), \\
 E_{r2} &= \frac{1}{\sqrt{2}}(E_s - E_{LO}), \\
 E_{r3} &= \frac{1}{\sqrt{2}}(E_s + iE_{LO}), \\
 E_{r4} &= \frac{1}{\sqrt{2}}(E_s - iE_{LO}),
 \end{aligned} \tag{2.5}$$

where $i^2 = -1$. Then, the photocurrents of the in-phase and quadrature parts are calculated by

$$\begin{aligned} I_I(t) &= R\sqrt{P_s(t)P_{LO}(t)} \cos(\phi_s(t) - \phi_{LO}(t)), \\ I_Q(t) &= R\sqrt{P_s(t)P_{LO}(t)} \sin(\phi_s(t) - \phi_{LO}(t)). \end{aligned} \quad (2.6)$$

The complex amplitude of the optical signal is obtained by such *phase-diversity homodyne* receiver or *indradyne* receiver [30]. It should be noted that it is difficult to keep the SOP of the signal identical to the LO due to the birefringence of the optical fiber in practice. The polarization-diversity receiver is then introduced to address this issue. Two *phase-diversity homodyne* receivers are incorporated by separating the signal and the LO into two linear polarizations with the polarization beam splitter (PBS).

2.2 Digital Coherent Receiver

The schematic diagram of a digital coherent receiver with *polarization and phase-diversity homodyne* detection is shown in Fig. 2.3. The PBS separates the signal and the LO wave into two orthogonal polarizations. Then, the co-polarized signal and LO wave are mixed in the optical hybrids to generate the in-phase and quadrature components. Signal with complex amplitudes in two polarizations is then fed into linear trans-impedance amplifiers (TIA). After sampling by ADCs, the four signals are digitalized and sent into DSP for further processing.

The DSP can be split to several modules or subsystems to deal with different impairments, as shown in Fig. 2.4. Firstly, the four digitalized signals pass through the subsystem for front-end imperfection compensation. Basically, the imperfections include the skew between the four channels because of the differences among the paths; the power difference between the output signal because of the difference in photodiodes of the four channels;

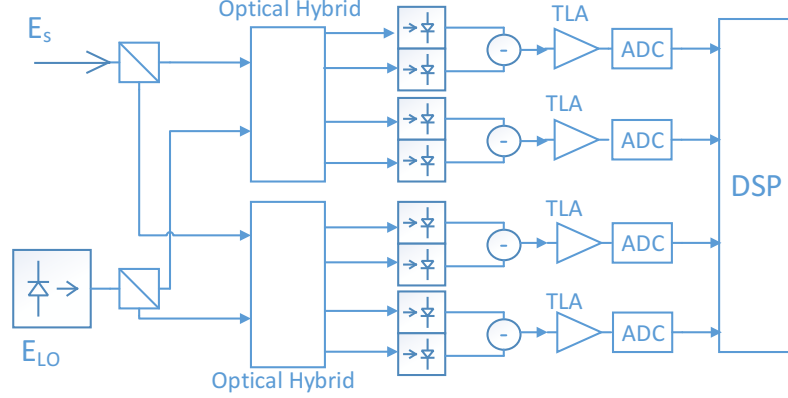


Fig. 2.3: Diagram of a digital coherent receiver with polarization and phase-diversity homodyne detection.

the IQ imbalance because of the imperfect optical hybrids. Then, the signal is resampled to 2 samples per symbol in the resampling subsystem. After that, equalizers are employed to compensate for the channel impairments. The static equalizer deals with chromatic dispersion, while the adaptive equalizer realizes polarization-demultiplexing and handles the residual dispersive effect. Timing recovery is performed in between the two equalizers. After equalizing the channel impairments, carrier recovery is required, which includes frequency offset compensation and laser phase noise compensation. The former deals with the frequency offset between the transmit laser and the LO, while the latter corrects the phase noise caused by both lasers. Finally, the symbol decision is performed and BER is calculated.

2.3 Subsystems of Digital Coherent Receivers

In this section, each subsystems along with the typical DSP algorithms are introduced.

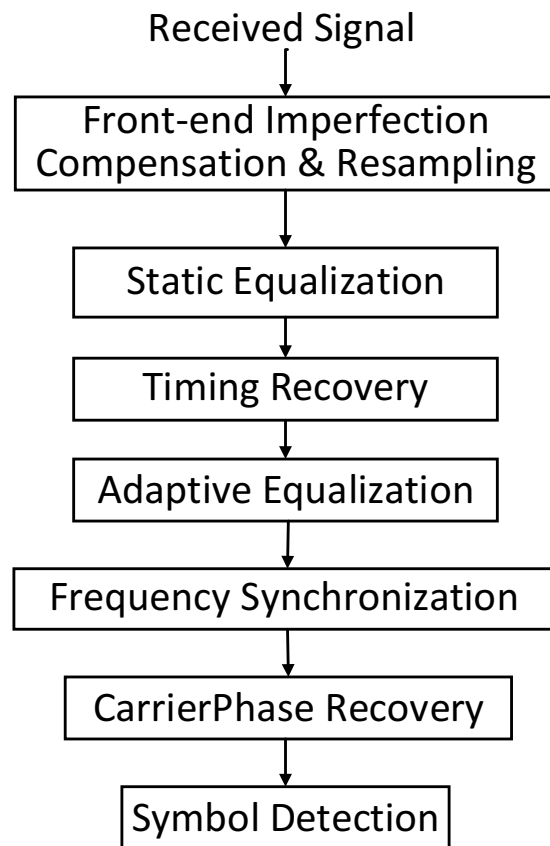


Fig. 2.4: The subsystems of DSP in coherent optical receivers.

2.3.1 IQ Imbalance Compensation

The received signal on the two polarizations can experience amplitude and phase imbalance due to differences of the photodiode responsivity or incorrect bias point of the modulator setup. This imbalance damages the orthogonality and degrades the system performance. To compensate for this impairment, the Gram-Schmidt orthogonalization procedure (GSOP) is usually employed [31]. The GSOP converts a set of non-orthogonal samples to orthogonal samples. Given two non-orthogonal components of the received signal, denoted by $I'(t)$ and $Q'(t)$, the GSOP generates a new pair of orthogonal signals by

$$\begin{bmatrix} I(t) \\ Q(t) \end{bmatrix} = \begin{bmatrix} \frac{1}{\sqrt{P_I}} & 0 \\ -\frac{a}{\sqrt{P_Q}} & \frac{1}{\sqrt{P_Q}} \end{bmatrix} \begin{bmatrix} I'(t) \\ Q'(t) \end{bmatrix}, \quad (2.7)$$

where $a = \mathbf{E}\{I'(t)Q'(t)\}$ is the correlation coefficient between the two received signals; P_I and P_Q are the powers of the two signals, respectively. Note that \mathbf{E} denotes the expectation operation.

2.3.2 Resampling

After compensating for front-end imperfections, the signal is resampled to 2 samples per symbol. For a digital communication system transmitting symbols at a rate S symbols/s, the minimum sampling rate is S Hz. However, a sampling rate of $2S$ Hz is advantageous for the purpose of digital timing recovery [9].

2.3.3 Static Equalization

It is beneficial to separate the channel equalization into static and dynamic equalization due to their differences in implementation. Typically, the former involves large static filters, while the latter needs relatively short but adaptive filters to compensate for time-varying effects. Here, static equalization is mainly to compensate for the CD. The transfer function

of the CD is given by [32]

$$H(\omega, z) = \exp\left(-j \frac{D\lambda^2}{4\pi c} \omega^2 z\right), \quad (2.8)$$

where D is the dispersion coefficient of the fiber, λ is the wavelength, c is the speed of the lightwave, ω is the angular frequency, and z is the transmission distance. The static equalizer is considered an all-pass filter with transfer function $H_s(\omega) = \frac{1}{H(\omega)}$, which is approximately realized by a finite impulse response (FIR) filter. This can be realized either in time domain, and thus referred to as time domain equalizer (TDE) [33], or in the frequency domain, referred to as frequency domain equalizer (FDE) [34]. TDE and FDE show different performance and complexity, and the selection depends on the dispersion of the channel and the required filter length [35]. Next, TDE and FDE are introduced, respectively.

2.3.3.1 Time Domain Equalizer

Equation (2.8) is used to generate the impulse response of a dispersive fiber by inverse Fourier transform, and the result is given by

$$h(z, t) = A \exp\left(j \frac{\pi c}{D\lambda^2 z} t^2\right), \quad (2.9)$$

where $A = \sqrt{\frac{c}{jD\lambda^2 z}}$. Now the impulse function of the TDE is

$$h_s(z, t) = A \exp\left(-j \frac{\pi c}{D\lambda^2 z} t^2\right). \quad (2.10)$$

Based on Eq (2.10), the impulse response is non-casual and infinite in duration. Therefore, the impulse response is truncated to accommodate practical implementation. If the signal is sampled at 2 samples per symbol, a fractionally spaced equalizer can effectively be realized with the tap spacing equal to the sampling interval, $T/2$ (T denotes the symbol period).

Assuming that the tap number is N , the tap weights are given as [33]

$$a_n = \sqrt{\frac{j c T^2}{D \lambda^2 z}} \exp\left(-j \frac{\pi c T^2}{D \lambda^2 z} n^2\right), \quad \left[\frac{N}{2}\right] < n < \left[\frac{N}{2}\right]. \quad (2.11)$$

Note that pulse shaping filters limit the effective bandwidth of the signal; as a result, the filter design for CD compensation can be performed over a smaller frequency range, leading to a reduction of complexity. Such consideration has been investigated in [36], where the least square criterion is applied to design FIR filter. Infinite impulse response (IIR) filter is also proposed; however, it is challenging to implement IIR filter in high speed applications with parallelized signal processing [37].

2.3.3.2 Frequency Domain Equalizer

When the number of taps, N , is large, it is more efficient to implement the FIR in frequency domain [38]. In principle, the received signals are converted to frequency domain by the fast Fourier transform (FFT), then multiply by the inverse of (2.8). Finally, the inverse FFT (IFFT) operation returns the signal to time domain.

2.3.4 Timing Recovery

Timing recovery deals with estimating the delay in order to realize the optimal detection of data. Gardner's algorithm [39] is widely used, owing to its low-complexity. Given the slow change of the delay, block by block processing is typically employed by assuming constant delay within each block [40]. It should be noted that Gardner's timing recovery algorithm is sensitive to high dispersion, and hence, it is performed after CD compensation.

2.3.5 Adaptive Equalizer

The adaptive equalizer aims to separate the two polarizations, as well as to compensate for the residual CD and PMD. Different from CD, the polarization effect is time-varying and thus requires an adaptive equalizer [9]. The structure of a butterfly equalizer is shown in Fig. 2.5, where \mathbf{E}_{hi} , \mathbf{E}_{vi} , \mathbf{E}_{ho} , and \mathbf{E}_{vo} are the input signal and output signal on the two

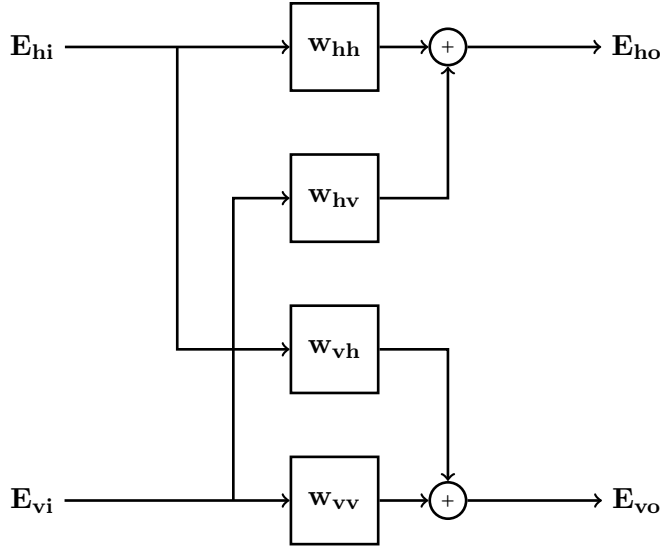


Fig. 2.5: The butterfly structure of an adaptive equalizer.

polarizations, respectively; \mathbf{w}_{hh} , \mathbf{w}_{hv} , \mathbf{w}_{vh} , \mathbf{w}_{vv} are the tap weights. The output of the equalizer is calculated by

$$\begin{aligned} \mathbf{E}_{ho} &= \mathbf{w}_{hh}^T \mathbf{E}_{hi} + \mathbf{w}_{hv}^T \mathbf{E}_{vi}, \\ \mathbf{E}_{vo} &= \mathbf{w}_{vh}^T \mathbf{E}_{hi} + \mathbf{w}_{vv}^T \mathbf{E}_{vi}. \end{aligned} \quad (2.12)$$

Depending on the use of a training sequence (TS), the adaptive equalizer can be either TS-based or blind. In general, a blind equalizer is used owing to increased spectral efficiency and simplicity. Two blind algorithms, namely the constant modulus algorithm (CMA) [9] and the radius directed equalizer (RDE) [41], are widely used in the transmission systems.

2.3.5.1 Constant Modulus Algorithm

In CMA, the cost function based on the constant modulus criterion is minimized. For example, the cost function for the h polarization is given by

$$J_{cma}[n] = \mathbf{E}\{(|E_{ho}[n]|^2 - R_h)^2\}, \quad (2.13)$$

where $R_h = \frac{\mathbb{E}\{|E_{hi}[n]|^4\}}{\{E_{hi}[n]\}^2}$ is the reference. The stochastic gradient descent is usually employed for CMA to update the filter coefficients on a symbol basis by

$$w_{hh}[n+1] = w_{hh}[n] - \mu \nabla J_{cma}[n], \quad (2.14)$$

where μ is the step size and ∇ is the gradient operator. Accordingly, the tap weights are updated by

$$\begin{aligned} w_{hh} &= w_{hh} + \mu \epsilon_h E_{hi} E_{ho}^* \\ w_{hv} &= w_{xy} + \mu \epsilon_h E_{hi} E_{vo}^* \\ w_{vh} &= w_{yx} + \mu \epsilon_v E_{vi} E_{vo}^* \\ w_{vv} &= w_{yy} + \mu \epsilon_v E_{vi} E_{vo}^* \end{aligned} \quad (2.15)$$

where $\epsilon_h = |E_{ho}|^2 - R_h$ and $\epsilon_v = |E_{vo}|^2 - R_v$.

2.3.5.2 Radius Directed Equalizer

CMA works for modulation formats with constant modulus; however, for higher-order modulation formats such as 16-QAM, the CMA cost function does not converge to zero. In order to ensure that the error tends to zero, RDE is employed. The principle is to partition the constellations into 3 classes based on the amplitude. Considering a power-normalized 16-QAM constellations, the reference amplitudes R_i ($i = 1, 2$, and 3) are $2/10$, 1 , and $18/10$, respectively. If $|E_{ho}[n]| \leq (\sqrt{R_1} + \sqrt{R_2})/2$, the symbol belongs to the inner ring and the reference R_h in (2.13) is R_1 ; if $|E_{ho}[n]| \leq (\sqrt{R_2} + \sqrt{R_3})/2$, the symbol belongs to the outer ring and the reference R_h in (2.13) is R_3 ; otherwise, the symbol is consider to be in the middle ring, and the reference R_h in (2.13) is R_2 . In general, CMA is still a good choice to achieve a pre-convergence for 16-QAM [41].

2.3.6 Frequency Offset Estimation and Compensation

After the aforementioned processing, the signal is expressed as

$$y_n = x_n \exp(j(2\pi \Delta f n T + \phi_n)) + w_n, \quad (2.16)$$

where y_n is the corrupted signal, x_n is the transmitted signal, Δf is the frequency offset, T is the symbol duration, ϕ_n is the carrier phase noise, and w_n is the additive zero-mean Gaussian noise (AWGN) [9]. To compensate for the frequency offset, it is required to first obtain an estimate as accurate as possible. Significant efforts have been made to develop feed-forward frequency offset estimation (FOE) algorithms for real-time implementation in M -QAM systems, aiming to improve the accuracy and reduce the complexity. A training symbol-based algorithm which utilizes Golay sequence is proposed in [42]. To reduce the complexity, the differential phase-based FOE avoids the FFT operation at the price of degrading the tracking speed, since only the consecutive pairs of the QPSK symbols are utilized [43]. Fourth-power FFT-based algorithms achieve higher accurate FOE by finding the peak of the power spectrum, at the cost of higher complexity [44, 45]. Taking advantage of QPSK partitioning and quasi-linear approximation, an FOE algorithm which balances the complexity and performance is proposed in [46]. In the sequel, the details of the FFT-based algorithm are provided as this achieves a good performance. To begin with, the received signal is raised to the 4th-power as

$$y_n^4 = E\{x_n^4\} \exp(j2\pi 4(n\Delta f T + \phi_n)) + e_n, \quad (2.17)$$

where e_n is a zero-mean process considered as a noise process [45]. FOE is then obtained by maximizing the periodogram of y_n^4 , being expressed as

$$\hat{\Delta f} = \frac{1}{4} \arg \max_{\Delta f \in [-1/2T, 1/2T]} \left| \frac{1}{N} \sum_{n=1}^{n=N} y_n^4 \exp^{-2j\pi n \Delta f T} \right|^2. \quad (2.18)$$

2.3.7 Carrier Phase Recovery

The phase caused by the lasers is modeled as a random walk process; more specifically, the difference between adjacent symbols' phase is Gaussian distributed with zero-mean, and the variance relates to the baud rate and laser linewidth. CPE algorithms with high linewidth tolerance and low-complexity are important. After CFO compensation, the task remains to estimate ϕ_n in (2.16). The CPE algorithms can be classified as blind or data-aided. More details about CPE algorithms will be provided in Chapter 6.

2.3.8 Symbol Decision

After carrier recovery, the signal could be decoded by using a soft decision (SD) forward error correction (FEC) or hard decision (HD) FEC. For hard decision, symbol estimation and bit decoding is required. It should be noted that in the presence of nonlinear phase noise, non-rectangular decision boundaries can improve the performance [47].

2.4 Concluding Remark

DSP-based coherent detection has led a revolution in the development of optical long haul networks. With an anticipation that advanced DSP algorithms could relax the pressure on photonic devices significantly, digital coherent transceivers will dominate the optical networks from long-haul to access scenarios in the near future. In this context, DSP algorithms will play an even more important role in the next-generation optical networks.

Chapter 3

Modulation Classification Using Received Signal's Amplitude Distribution for Coherent Optical Receivers

3.1 Background

The modern optical fiber communication networks are faced with challenges due to the significant demand for bandwidth. Furthermore, the fluctuating nature of the network traffic reflects the inefficiency of the fixed spectrum grid in current WDM systems. Recently, the EONs have been considered to deal with this dilemma by maximizing spectral and energy efficiencies [25]. Multiple parameters such as the modulation format, bit rate, and channel spacing can be changed dynamically to achieve flexibility for different scenarios. As most digital coherent receivers are adopting modulation format-dependent signal processing

algorithms, as well as due to the dynamic change of the modulation format, automatic MC becomes an essential part of re-configurable coherent receivers.

Research on MC in wireless communications has been carried out for decades [48–50]. In coherent optical communications, various techniques have been proposed in the most recent years. For example, machine learning-based techniques are applied to recognize signal’s amplitude histograms [51] or the Stokes space-based signal representation [52]; however, they require either prior training or iterative processing. Image processing techniques like the connected component analysis are employed in [53] to perform MC in the Stokes space domain, but such features are appropriate only for lower-order modulation formats. A non-iterative clustering algorithm is proposed in [54]; however, tracking the state of polarization and recovering the initial polarization state are required before the MC stage. Algorithms relying on the received signal’s power distribution have been also employed. The peak-to-average power ratio is chosen as a feature to distinguish different modulation formats in [55]; however, different thresholds need to be established for each OSNR. Certain ratios obtained from the normalized power distribution are selected to characterize the modulation formats in [56]; nevertheless, selection of these ratios is necessary for different candidate modulation formats. An MC algorithm is proposed, which requires relatively small number of samples and is robust to frequency offset and carrier phase noise.

3.2 Proposed Algorithm

3.2.1 Extracted Discriminating Feature

The schematic diagram of a digital receiver including the MC module is shown in Fig. 3.1. The IQ imbalance, resampling, and chromatic dispersion compensation are performed first. Then, CMA is applied to separate the two polarizations. The proposed MC algorithm fol-

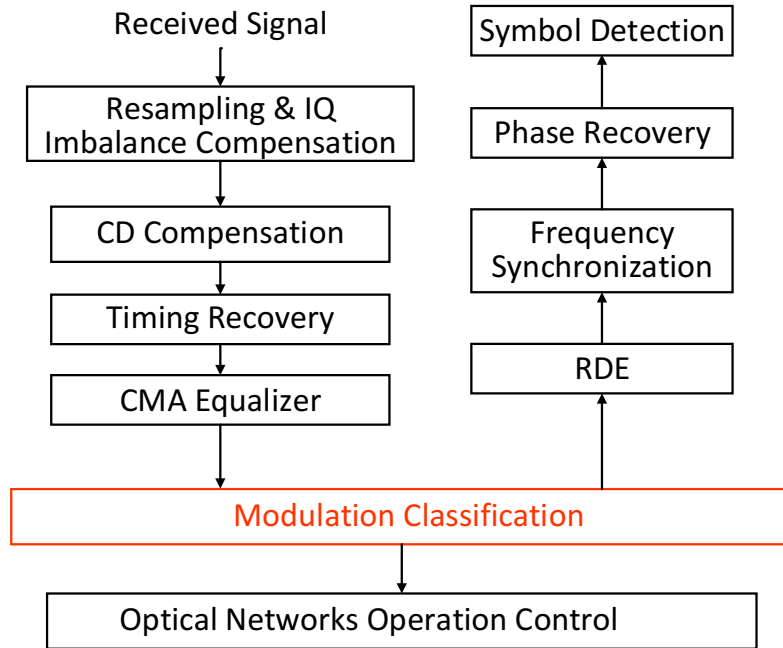


Fig. 3.1: DSP structure including the MC subsystem.

lows, which employs the CDF of signal's normalized amplitudes. After the MC module, the RDE, frequency synchronization, and phase recovery are applied sequentially. The MC algorithm is signal's amplitude-based, and thus, does not require carrier recovery. On the other hand, knowledge of the modulation format is beneficial for the succeeding digital processing steps, such as frequency offset and phase noise compensation. The constellations of different modulation formats affecting by frequency offset and laser phase noise are shown in Fig. 3.2. To perform low-complexity classification, this two-dimensional pattern is converted into the one-dimensional CDF of the constellations' normalized amplitudes.

The CDF for M -QAM formats ($M=4, 8, 16, 32,$ and 64) are shown in Fig. 3.3. In order to highlight the discriminating feature, an OSNR of 30 dB is considered. These recognizable curves are employed as the feature for the proposed MC algorithm.

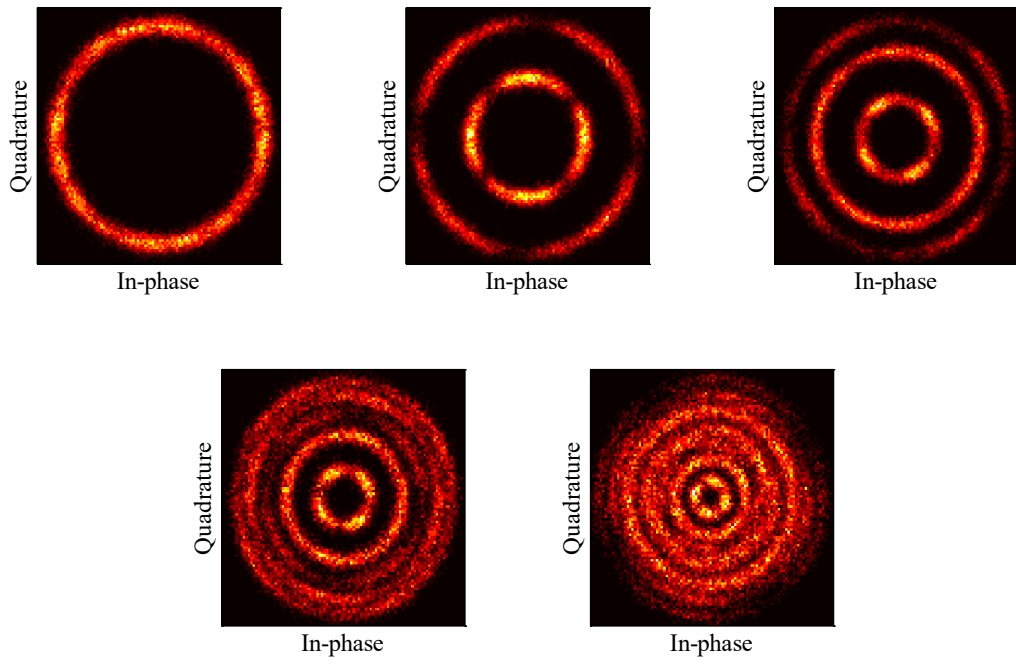


Fig. 3.2: Constellations of M -ary QAM formats affecting by frequency offset and laser phase noise ($M = 4, 8, 16, 32, 64$).

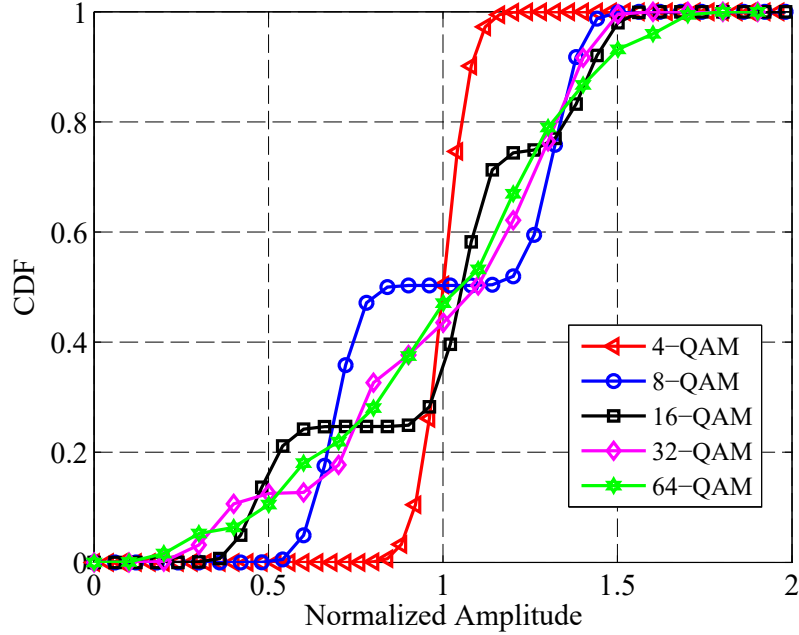


Fig. 3.3: CDFs for M -ary QAM signals with an OSNR of 30 dB.

3.2.2 CDF-based MC Algorithm

Before MC is performed, it is assumed that CD is compensated and the two polarizations are separated. Therefore, the primary source of signal corruption is the AWGN. Similar to [55], the OSNR of the received signal is assumed to be known. Hence, the receiver is able to emulate the signals' CDFs of all possible candidate modulation formats with the known OSNR. The reference signal's samples can be expressed as

$$y_{k,n} = x_{k,n} + w_n, 1 \leq n \leq N, \quad (3.1)$$

where $y_{k,n}$ and $x_{k,n}$ are the n th symbol of the received and transmitted signals with the k th modulation format, respectively, w_n represents AWGN with variance σ^2 , and N is the number of samples. Here are five candidates: $k = 1$ (4-QAM); $k = 2$ (8-QAM); $k = 3$ (16-QAM); $k = 4$ (32-QAM), and $k = 5$ (64-QAM). To add the corresponding noise, the OSNR

should be converted into signal-to-noise ratio (SNR) according to [57]

$$\text{SNR}(\text{dB}) = \text{OSNR}(\text{dB}) - 10\log_{10}(R_s/B_{ref}), \quad (3.2)$$

where B_{ref} is the reference bandwidth (≈ 12.5 GHz at 1550 nm) and R_s is the symbol rate. Once all possible signals are generated, their CDFs can be obtained as references. Then, comparisons are carried out between the received signal's CDF and each reference CDF. The one with the most similar CDF shape to the received signal's CDF is decided as the transmitted modulation format.

To measure this similarity, the average distances between the received signal's CDF and each candidate reference CDF are calculated. In (3.3), $F_{1,k}(z_n)$ is the CDF of the k th candidate, and the received signal's CDF is represented by $F_0(z_n)$. Next, the average distance is calculated by (3.4), where μ_k is the average distance between the received signal's CDF and the k th candidate CDF. The minimum average distance indicates the most likely transmitted modulation format, according to (3.5).

$$F_k(z_n) = |F_{1,k}(z_n) - F_0(z_n)|, 1 \leq n \leq N. \quad (3.3)$$

$$\mu_k = N^{-1} \sum_{n=1}^N F_k(z_n). \quad (3.4)$$

$$\hat{k} = \arg \min_k (\mu_k). \quad (3.5)$$

The amplitude-based feature of the proposed algorithm is appealing because it tolerates the constellation rotation caused by the frequency offset and carrier phase noise. This enables the application of MC at an earlier stage in the digital coherent receiver. However, the similarity of the CDFs for different modulation formats increases when the OSNR decreases. Therefore, investigations are needed to verify the MC performance in the OSNR range of practical interest.

3.3 Performance Evaluation

The performance of the proposed algorithm is evaluated by both experiments and simulations.

3.3.1 Experiments and Results

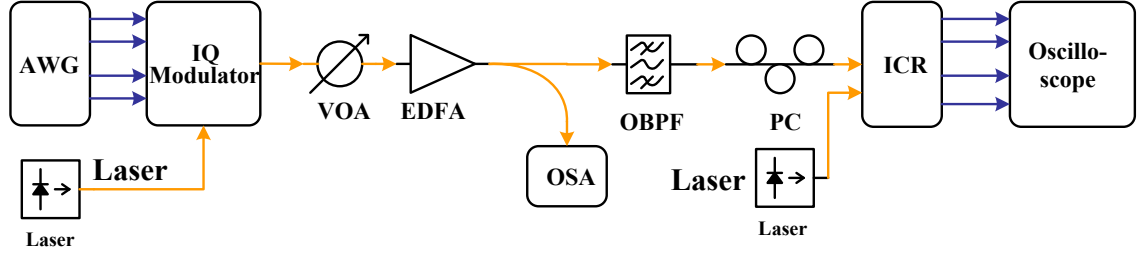


Fig. 3.4: Experimental B2B system setup.

The proposed algorithm is implemented in optical B2B experiments. The setup is shown in Fig. 3.4. The arbitrary waveform generator (AWG) operates at 12.5 GBd. The sampling rate of the oscilloscope is 50 Gsamples/s. Two free running lasers with 1550.12 nm wavelength are acting as transmit laser and LO, respectively. The linewidth of each laser is about 100 kHz, and the frequency offset is around 200 MHz. An EDFA with fixed output power and a variable optical attenuator (VOA) are combined to adjust the OSNR values from 10 dB to 20 dB. An optical bandpass filter (OBPF) with 0.6 nm bandwidth is placed after the EDFA. The power entering the integrated coherent receiver (ICR) is around -2 dBm, while the output power of the local oscillator is 13.5 dBm. The OSNR is measured with the optical spectrum analyzer (OSA), and the PC is used to adjust the polarization state. The data is collected from the oscilloscope and processed offline. After the resampling and the IQ imbalance compensation modules, a symbol-spaced butterfly-type adaptive filter is employed to separate the two polarizations. During the MC stage, similar to [56], 10000

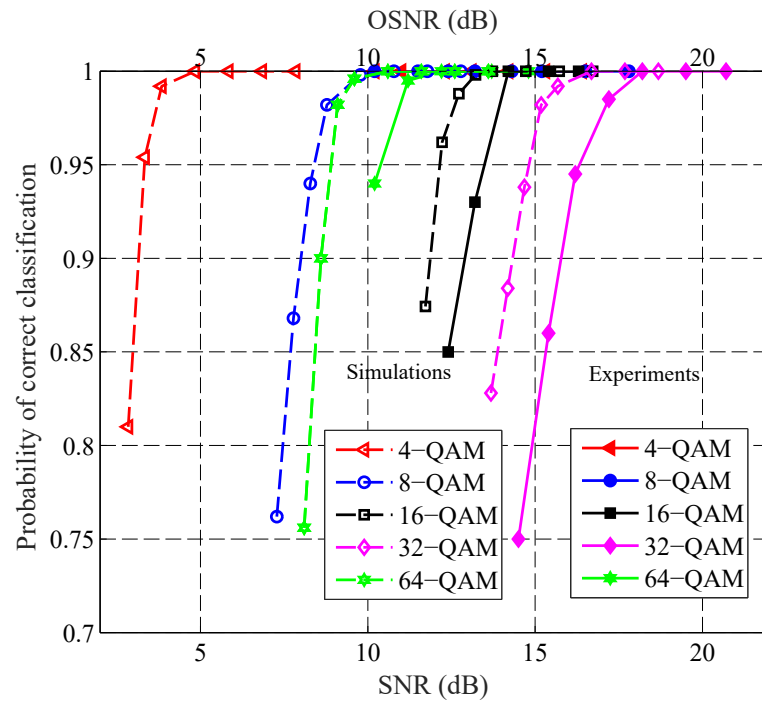


Fig. 3.5: Probability of correct classification vs. SNR (bottom) and OSNR (top) obtained from experiments.

samples of the received signal are collected to derive the empirical CDF of the normalized amplitude.

The probability of correct classification obtained from 200 realizations for each modulation format is shown in Fig. 3.5. The simulation results of back-to-back are also shown in this figure. We can see that the experimental results have around 1.5 dB penalty compared to simulation results for 16-QAM, 32-QAM and 64-QAM cases. This is mainly caused by the additional electrical noise from imperfect devices such as AWG and ICR, as well as the error introduced by the OSNR readings from the OSA. Note that 64-QAM can be detected with lower OSNR than 16-QAM and 32-QAM; this can be explained as follows. From Fig. 3.3, it can be seen that the CDFs of 16-QAM, 32-QAM and 64-QAM are close to each other. As the noise level increases, the received signal's CDF curves corresponding to 16-QAM and 32-QAM are likely to be decided as 64-QAM.

It is worth to note that feature-based MC algorithms do not provide all optimal performance; the features are usually selected in an ad-hoc way, and the corresponding algorithms can be simple to implement and robust to transmission impairments such as frequency offset and phase noise. Another category of MC algorithms is likelihood-based, which provide an optimal solution. However, these are sensitive to transmission impairments and suffer of high computational complexity.

3.3.2 Further Investigations with Numerical Simulations

In order to extend our investigation with optical fiber and higher data rate, the VPItransmissionMaker 9.7 is used to carry out simulations. PDM 4-QAM, 8-QAM, 16-QAM, 32-QAM, and 64-QAM signal at 32 GBd rate are considered. The laser linewidth is 100 kHz and the fiber is 800 km long.

To simplify the simulations, the fiber nonlinearity is ignored. 500 independent simula-

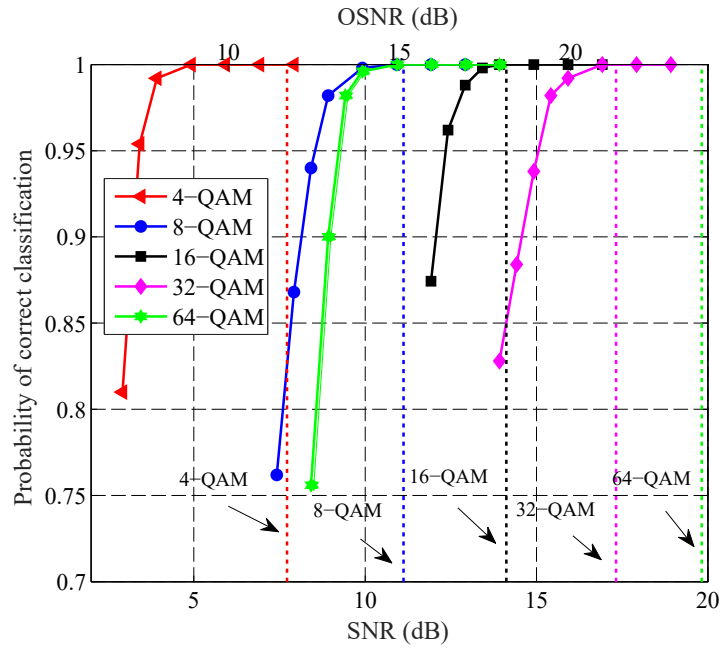


Fig. 3.6: Probability of correct classification vs. SNR (bottom) and OSNR (top) obtained from simulations.

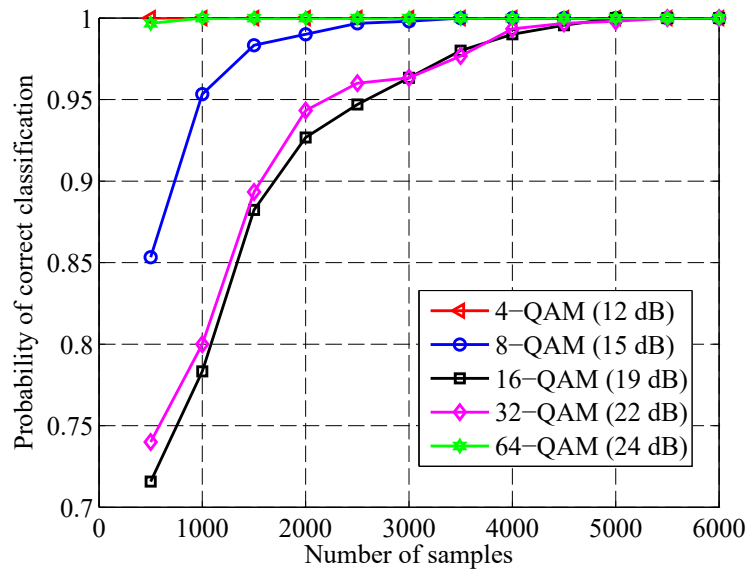


Fig. 3.7: Probability of correct classification vs. number of samples obtained from simulations.

tions with different noise seeds are carried out for each OSNR. Figure 3.6 illustrates the required SNR and OSNR when the successful classification rate is larger than 0.75. The OSNR ranges of different modulation formats are chosen based on practical operation of coherent optical systems. The SD FEC thresholds for 28 GBd rate PDM system with 4-QAM, 8-QAM, 16-QAM, 32-QAM, and 64-QAM are illustrated by the vertical dash lines [54]. It can be seen from Fig. 3.6 that the proposed algorithm can achieve 100% successful classification rate with lower OSNR values than the SD FEC thresholds. According to Figs. 3.5 and 3.6, simulation results show the same tendency of correct classification rate as experimental results.

Another important factor considered in MC is the number of samples needed to achieve a good performance [53]. Figure 3.7 shows the successful classification rate with different number of samples for 4-QAM, 8-QAM, 16-QAM, 32-QAM, and 64-QAM when the OSNR equals 12 dB, 15 dB, 19 dB, 22 dB, and 24 dB, respectively. Note that the same OSNR values as in [54] are utilized. To achieve 100% successful classification rate for all of these five modulation formats, the proposed algorithm requires $N = 5500$ samples, while 8000 samples are needed for the algorithm in [54]. More specifically, the proposed algorithm needs 500, 3500, 5500, 5500, and 1000 samples to successfully classify 4-QAM, 8-QAM, 16-QAM, 32-QAM, and 64-QAM, respectively. On the other hand, the algorithm in [54] requires about 3000, 3000, 4000, 1000, and 8000 samples to successfully identify 4-QAM, 8-QAM, 16-QAM, 32-QAM, and 64-QAM, respectively. The proposed algorithm utilizes less samples to attain the same performance, which is an added advantage. Furthermore, the algorithm in [54] employs a multi-dimensional tree to search among the neighbour points required for the clustering process, which has a complexity of $O(N \log N)$, while the proposed algorithm has a complexity of the order $O(N)$.

The effect of fiber nonlinearity on MC is also investigated. The fiber nonlinearity is

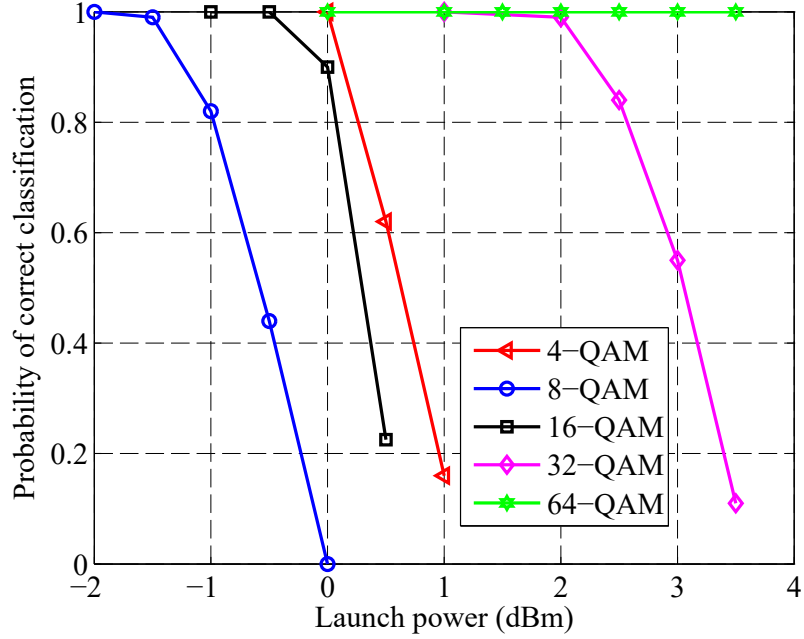


Fig. 3.8: Probability of correct classification vs. launch power.

related to the launch power and fiber length, and results in additional distortions that can become indistinguishable from the amplified spontaneous emission noise [58]. The fiber lengths are 11200 km, 7600 km, 2800 km, 1040 km, and 560 km for 4-QAM, 8-QAM, 16-QAM, 32-QAM, and 64-QAM, respectively. In this case, the BER for each modulation format is at the SD-FEC threshold when the launch power is 0 dBm. Then, the launch power is varied from -2 dBm to 3.5 dBm to see the impact of fiber nonlinearity. According to Fig. 3.8, 64-QAM has 100% successful classification due to the relatively short link length, while 8-QAM suffers mostly from the fiber nonlinearity. In general, results show that the modulation formats can be classified 100% successfully when the launch power is below -2 dBm.

Additionally, the performance comparison is provided versus the MC scheme in [56], since this also utilizes the received signal's amplitude. When the number of samples is 10000, the required OSNRs for PDM 4-QAM, 16-QAM, 32-QAM, and 64-QAM are listed

in Table 3.1. It can be seen that the proposed algorithm requires higher OSNR for 16-QAM only, while a lower OSNR is needed for 4-QAM, 32-QAM, and especially 64-QAM, when compared with the algorithm in [56]. The complexity of the two algorithms is compared in Table 3.2. It is assumed that N samples are observed, and the number of bins for CDF plotting is 1000. It can be seen that both algorithms need only few real multiplications, while the proposed algorithm requires more real additions. However, it is worth noting that the extra processing time caused by the additions is not significant with high speed micro-processors. Also note that the complexity for amplitude extraction is not considered here because both algorithms use features based on the signal's amplitude.

Table 3.1: Required OSNR (dB) for 100% successful classification.

Classification algorithm	4-QAM	16-QAM	32-QAM	64-QAM
Algorithm in [56]	11.2	16.5	22	24
Proposed algorithm	9	18	21	15

Table 3.2: Computational cost for the proposed algorithm and one of its counterparts.

Classification algorithm	Real multiplications	Real additions
Algorithm in [56]	3	$4N$
Proposed algorithm	5	$44N + 4000$

3.4 Summary

An MC algorithm based on the CDF of the received signal's normalized amplitude for coherent optical receivers is proposed. The proposed algorithm requires a fairly small number of samples and can be performed in the presence of frequency offset and phase noise. Optical B2B experiments and extensive numerical simulations show that 100% successful MC is achieved among PDM 4-QAM, 8-QAM, 16-QAM, 32-QAM and 64-QAM signals within the OSNR range of practical interests. Furthermore, the MC algorithm works well for launch powers below -2 dBm. Such results are achieved with modest computational cost.

Chapter 4

OSNR Estimation for Coherent Optical Receivers Employing Multi-level Constellations

4.1 Background

Optical performance monitoring (OPM) has emerged as an indispensable module for intelligent and flexible next-generation WDM optical fiber transmission systems [26]. As an important mechanism to improve the control of transmission and fault management, OPM involves evaluating the optical channel quality by measuring various optical characteristics, such as the channel power and OSNR. The OSNR indicates a degree of impairment in a transmission system caused by optical amplifiers. This is important because optical fiber transmission systems work properly only when the link OSNR is above a certain threshold. On the other hand, the ever-increasing demand for high-speed data services has led to a super-channel transmission architecture, with reduced or even no guard bands.

In this context, the conventional optical spectrum-based OSNR measurement is not suitable [59]. Therefore, the OSNR estimation has been integrated in the coherent digital receivers [57–67]. Three types of digital approaches have been proposed for in-band OSNR estimation: DA [59–61], supervised machine learning-based [62], [63], and NDA [57,58,64–67]. The DA approaches require frame synchronization to extract pilots, and the overhead results in reduced SE. Supervised machine learning-based techniques need extensive training data and computational resources. On the other hand, NDA methods have the advantage of in-service estimation without reducing the SE. The existing NDA methods exploit the statistical moments from the signal’s amplitude after polarization demultiplexing [57,64–66]. Using the correlation functions of the received symbols, the moment-based methods can further be applied in the presence of fiber nonlinearity [68]. However, as proved in [69], such moment-based OSNR approaches suffer performance degradation for multilevel constellations such as 16-QAM. More specifically, the variance of these estimators considerably departs from the Cramér-Rao lower bound (CRLB). Since multilevel constellations are essential for optical fiber transmissions requiring high SE, more accurate estimation algorithms are required [27].

In this chapter, a novel NDA OSNR estimation algorithm for multilevel constellation, M-QAM ($M = 8, 16, 32, \text{ and } 64$), is proposed. The CDF of the received signal’s amplitude after polarization demultiplexing is used as the statistical feature instead of the moments. The proposed algorithm consists of two stages: a coarse and a fine estimation stage, respectively. The first stage generates a coarse estimate from several predefined candidates, and the result is used as the initial value to facilitate the convergence for the second stage. At the second stage, the Newton’s method is employed to obtain a fine estimate based on the empirical CDF. It is shown that the proposed algorithm provides an asymptotically unbiased estimator which attains the CRLB. Moreover, a lower mean square error (MSE) is

attained when compared to the popular NDA second-moment and fourth-moment (M2M4) estimator [57,64–66]. Furthermore, the proposed estimation algorithm involves significantly lower complexity than M2M4.

The remainder of this chapter is organized as follows: Section 4.2 introduces the system model and the proposed estimation algorithm. Section 4.3 presents the error analysis of the proposed algorithm and the CRLB derivation. Numerical results for the algorithm, as well as comparisons with M2M4 are provided in Section 4.4, while simulation results in the presence of fiber nonlinearity are given in Section 4.5. Section 4.6 discusses the complexity of the proposed algorithm and M2M4. Finally, this chapter is summarized in Section 4.7.

4.2 Principle of Operation

4.2.1 System Model

In the coherent digital receiver, static and adaptive channel equalizers are applied sequentially to compensate for the linear impairments, such as CD and PMD. Then, timing recovery is performed. Without loss of generality, the signal after the above-mentioned processing in the receiver is primarily impacted by frequency offset, phase noise, and ASE noise from EDFA [9]. Accordingly, the signal of one polarization can be expressed by

$$y_n = x_n e^{j(2\pi\Delta f nT + \phi_n)} + w_n, 1 \leq n \leq N, \quad (4.1)$$

where y_n is the n th symbol of the received signal, x_n is the n th symbol of the transmitted signal drawn from unit-energy constellations, Δf is the frequency offset, T is the symbol duration, ϕ_n is the phase noise, w_n is complex circular independently and identically distributed (i.i.d) Gaussian noise sample with zero mean and unknown variance of σ^2 , and N is the number of samples.

The sets of possible amplitudes for the constellations are denoted as \mathcal{M}_k , where $k =$

1, 2, 3, and 4 represents 8-QAM, 16-QAM, 32-QAM, and 64-QAM, respectively. More specifically, $\mathcal{M}_1 = \{1/\sqrt{3+\sqrt{3}}(\sqrt{2}, \sqrt{4+2\sqrt{3}})\}$, $\mathcal{M}_2 = \{1/\sqrt{10}(\sqrt{2}, \sqrt{10}, \sqrt{18})\}$, $\mathcal{M}_3 = \{1/\sqrt{20}(\sqrt{2}, \sqrt{10}, \sqrt{18}, \sqrt{26}, \sqrt{34})\}$, $\mathcal{M}_4 = \{1/\sqrt{42}(\sqrt{2}, \sqrt{10}, \sqrt{18}, \sqrt{26}, \sqrt{34}, \sqrt{50}, \sqrt{58}, \sqrt{74}, \sqrt{98})\}$. Accordingly, the amplitudes of the transmitted signal, \mathbf{a}_n , represent a sequence drawn from \mathcal{M}_k with probability \mathbf{p}_k . The probabilities for the elements in \mathcal{M}_k are $\mathbf{p}_1 = [1/2, 1/2]$, $\mathbf{p}_2 = [1/4, 1/2, 1/4]$, $\mathbf{p}_3 = [1/8, 1/4, 1/8, 1/4, 1/4]$, and $\mathbf{p}_4 = [1/16, 1/8, 1/16, 1/8, 1/8, 3/16, 1/8, 1/8, 1/16]$.

4.2.2 OSNR and SNR

Based on the above model, the SNR estimation is achieved by $\hat{\text{SNR}} = 1/\hat{\sigma}^2$, given the estimate of the noise variance. To obtain the OSNR, the relationship between OSNR and SNR needs to be considered. Ideally, the OSNR can be calculated based on the SNR as

$$\text{OSNR} = R_s/(B_{ref}) \cdot \text{SNR}, \quad (4.2)$$

where R_s is the baud rate and B_{ref} is a reference bandwidth, which equals 12.5 GHz (0.1 nm). Several existing algorithms employ this relationship [57, 65]. However, it should be noted that the received signal is affected by other kinds of noise from the transceiver in addition to the ASE noise.

In the presence of transceiver noise, an alternative approach is based on

$$\frac{1}{\text{SNR}} = \zeta \cdot \frac{1}{\text{OSNR}} + \eta, \quad (4.3)$$

where ζ denotes a proportional constant between SNR and OSNR, and η is attributed to the background noise of the transmitter and receiver [59]. The coefficients ζ and η uniquely depend on the specific configuration, and can be obtained by fitting the estimated SNR and known OSNR linearly. On the other hand, the OSNR estimation accuracy is determined by the SNR estimation if ζ and η are obtained accurately. Throughout the chapter, the

estimation of the SNR is studied, and (4.2) is employed in the simulations to convert OSNR into SNR.

4.2.3 Proposed Estimation Algorithm

The empirical CDF of the received signal's amplitude is generated according to [70]

$$F_E(z) = \frac{1}{N} \sum_{n=1}^N C(a_n \leq z). \quad (4.4)$$

Here z denotes the discrete amplitude of the signal, ranging from 0 to Z with a step of Z/B . B is the number of bins, set to 100 in the following simulations. Z is set to 3.5 to guarantee that, within the considered SNR range, the CDFs of the four modulation formats is 1 when z approaches Z . In addition, C is a specific function, which equals one if the input is true and zero if the input is false. Then, assuming that the k th modulation is transmitted, the theoretical CDF of the signal's amplitude for AWGN channel is given by

$$F_k(z, \sigma) = 1 - \sum_{m=1}^{dim(\mathbf{p}_k)} \mathbf{p}_k[m] Q_1 \left(\frac{\sqrt{2}\mathbf{a}_k[m]}{\sigma}, \frac{\sqrt{2}z}{\sigma} \right), \quad (4.5)$$

where $dim(\cdot)$ means the dimension of the vector, and Q_1 is the Marcum-Q function [71]. Thus, σ can be determined based on equation (4.5), given the information on z and F_k .¹ The details are provided in the sequel.

Firstly, using the empirical CDF, the following equation is established:

$$F_k(z, \sigma) = F_E(z). \quad (4.6)$$

Assuming z is determined, then the only unknown σ can be obtained by solving (4.6). In Section 4.3, it is shown that z impacts the estimation accuracy. To solve (4.6), the Newton's method, which is a powerful technique to solve nonlinear equations and has the merit of

¹The estimate of SNR can be obtained, given the estimate of σ . Henceforth, focus will be placed on the estimation of σ .

Algorithm 1 Newton's method for (4.6).

Input:Obtained empirical CDF, $F_E(z)$;**Output:** $\hat{\sigma}$, estimate of σ ;

- 1: The initial value of $\hat{\sigma}$ is $\hat{\sigma}^{(0)}$;
the initial iteration counter $i = 0$;
the iteration threshold is $TH = 0.0005$;
maximum iteration $i_{max} = 10$;
 - 2: **while** ($|\Delta\sigma| \geq TH$) *and* ($i \leq i_{max}$) **do**
 - 3: $\Delta F_E(z) = F_E(z) - F_k(z, \hat{\sigma}^{(i)})$;
 - 4: $\Delta\sigma = \left(\frac{\partial F_k(z, \sigma)}{\partial \sigma} \right)^{-1} \Big|_{\sigma=\hat{\sigma}^{(i)}} \Delta F_E(z)$;
 - 5: $\hat{\sigma}^{(i+1)} = \hat{\sigma}^{(i)} + \Delta\sigma$;
 - 6: $i = i + 1$;
 - 7: **end while**
 - 8: $\hat{\sigma} = \hat{\sigma}^{(i)}$;
 - 9: **return** $\hat{\sigma}$;
-

quadratic convergence speed [72–74], is employed. To begin with, the differential equation of (4.6) with respect to σ is given by

$$\Delta F_E(z) = \frac{\partial F_k(z, \sigma)}{\partial \sigma} \times \Delta\sigma. \quad (4.7)$$

The general expression of the gradient $\frac{\partial F_k(z, \sigma)}{\partial \sigma}$ for different QAMs is given in (4.8) at the top of the next page. To obtain the expression, some important features of Marcum Q function is needed [75] and they are given in the appendix. In this equation, $I_\alpha(\alpha = 0, 1)$ is the modified Bessel function of the first kind, and the value of α represents the order.

$$\begin{aligned}
\frac{\partial F_k(z, \sigma)}{\partial \sigma} &= \frac{\partial(1 - \sum_{m=1}^{\dim(\mathbf{p}_k)} \mathbf{p}_k[m] \cdot Q_1(\frac{\sqrt{2}\mathbf{a}_k[m]}{\sigma}, \frac{\sqrt{2}z}{\sigma}))}{\partial \sigma} \\
&= - \sum_{m=1}^{\dim(\mathbf{p}_k)} \mathbf{p}_k[m] \left(\frac{\sqrt{2}z}{\sigma} I_1 \left(\frac{2z \cdot \mathbf{a}_k[m]}{\sigma^2} \right) \exp \left(-\frac{2z^2}{\sigma^2} + \frac{2\mathbf{a}_k[m]^2}{\sigma^2} \right) \left(-\frac{\sqrt{2}\mathbf{a}_k[m]}{\sigma^2} \right) - \right. \\
&\quad \left. \frac{\sqrt{2}z}{\sigma} I_0 \left(\frac{2z \cdot \mathbf{a}_k[m]}{\sigma^2} \right) \exp \left(-\frac{2z^2}{\sigma^2} + \frac{2\mathbf{a}_k[m]^2}{\sigma^2} \right) \left(-\frac{\sqrt{2}z}{\sigma^2} \right) \right) \\
&= \sum_{m=1}^{\dim(\mathbf{p}_k)} \mathbf{p}_k[m] \left[\frac{2z}{\sigma^3} \exp \left(-\frac{z^2 + \mathbf{a}_k[m]^2}{\sigma^2} \right) \left(\mathbf{a}_k[m] I_1 \left(\frac{2z \cdot \mathbf{a}_k[m]}{\sigma^2} \right) - z I_0 \left(\frac{2z \cdot \mathbf{a}_k[m]}{\sigma^2} \right) \right) \right].
\end{aligned} \tag{4.8}$$

Assuming that the initial estimate of σ is $\hat{\sigma}^{(0)}$, the details of the Newton's method are shown in Algorithm 1 on the previous page. Although the speed of convergence is quadratic, the Newton's method requires an initial estimate that is sufficiently closed to the true value to guarantee the convergence. Supposing that $F_k(z, \sigma)$ is a twice differentiable function on an interval containing the root of interest, β , and supposing that $\frac{\partial F_k(z, \sigma)}{\partial \sigma} \neq 0$, to ensure convergence, the initial estimate needs to satisfy

$$T = \frac{|\beta - \hat{\sigma}^{(0)}| \cdot \left| \frac{\partial^2 F_k(z, \sigma)}{\partial^2 \sigma} \right|_{\sigma=\beta}}{\left| 2 \frac{\partial F_k(z, \sigma)}{\partial \sigma} \right|_{\sigma=\beta}} < 1. \tag{4.9}$$

As T relates to the actual value of σ which is unknown, it is very challenging to provide a closed-form solution to determine the initial estimate. Instead, a practical approach is to introduce a coarse estimation stage before applying the Newton's method. At this stage, the most likely candidate is selected from several predefined variances; the procedure is similar to that in our previous work [67]. CDFs corresponding to these predefined variances are generated, and the average distances between these CDFs and the empirical CDF are used to determine the likelihood. More concisely, a group of J possible initial estimates are defined as $[\hat{\sigma}_1^{(0)}, \hat{\sigma}_2^{(0)}, \dots, \hat{\sigma}_J^{(0)}]$. Then, the corresponding CDFs are generated accordingly as $F_k(z, \hat{\sigma}_j^{(0)})$, where $j = 1, 2, \dots, J$. After that, the average distances between the generated

CDFs and the empirical CDF are calculated as $d_j = \sum_{z=0}^Z [F_k(z, \hat{\sigma}_j^{(0)}) - F_E(z)]/B$. Finally, the candidate $\hat{\sigma}_j^{(0)}$ that attains the minimum average distance, d_j , is selected as the coarse estimate.

4.3 Estimation Error Analysis and CRLB on the Variance of the Proposed Estimator

In this section, the estimation error is analyzed and the CRLB on the variance of the proposed estimator is derived.

4.3.1 Measurement Error of the Empirical CDF

Because measurement error of the empirical CDF is inevitable, it is important to review the statistical characteristic of the measurement error before performing analysis on the estimation error. The measurement error of the empirical CDF is denoted as ϵ_{FE} . It is shown in [76] that the measurement error of the empirical CDF is asymptotically normal distributed with mean $E\{\epsilon_{FE}\} = 0$ and variance

$$\sigma_F^2 = \frac{F_k(z, \sigma) \cdot [1 - F_k(z, \sigma)]}{N}. \quad (4.10)$$

According to (4.10), the variance of the measurement error of the empirical CDF is determined by the number of samples, N , and the actual CDF, $F_k(z, \sigma)$. In addition, the variance depends on z . When N is fixed, the variance attains its maximum at z_m , where $F_k(z_m, \sigma) = 1/2$. On the other hand, the variance is 0 when $F_k(z, \sigma)$ is 0 or 1.

4.3.2 Estimation Error Analysis

According to Step 4 in Algorithm 1, the estimation error is approximately

$$\epsilon_\sigma = \hat{\sigma} - \sigma \approx \left(\frac{\partial F_k(z, \sigma)}{\partial \sigma} \right)^{-1} \epsilon_{FE}. \quad (4.11)$$

This approximation is accurate when the variance, σ_F^2 , is relatively small. Based on (4.10), σ_F^2 is small when N is relatively large, since $F_k(z, \sigma)$ ranges from 0 to 1. Under such conditions, the proposed estimator is asymptotically unbiased because $E\{\epsilon_\sigma\} = \left(\frac{\partial F_k(z, \sigma)}{\partial \sigma}\right)^{-1} E\{\epsilon_{FE}\} = 0$. Based on (4.10) and (4.11), the variance of $\hat{\sigma}$ is obtained as

$$var(\hat{\sigma}) = E\{\epsilon_\sigma \epsilon_\sigma\} = \frac{\sigma_F^2}{\left(\frac{\partial F_k(z, \sigma)}{\partial \sigma}\right)^2} = \frac{F_k(z, \sigma) \cdot [1 - F_k(z, \sigma)]}{N \left(\frac{\partial F_k(z, \sigma)}{\partial \sigma}\right)^2}. \quad (4.12)$$

It can be seen that the variance of the estimates is inversely proportional to the number of samples. In addition, it is important to choose a proper value for z , as it impacts the value of $F_k(z, \sigma)$ and its derivative with respect to σ . A typical approach to choose z is finding the extrema of (4.12), by setting the derivative of (4.12) with respect to z to zero. This is given in (4.13), with the second and first partial derivatives of $F_k(z, \sigma)$ with respect to σ and z provided in (4.14) and (4.15), respectively. Lastly, it is noted that the estimation accuracy relates to the actual σ , which is unknown.

$$\begin{aligned} & \frac{\partial \left(F_k(z, \sigma) \cdot [1 - F_k(z, \sigma)] / \left(\frac{\partial F_k(z, \sigma)}{\partial \sigma}\right)^2 \right)}{N \cdot \partial z} \\ &= \frac{\partial \left(F_k(z, \sigma) \cdot [1 - F_k(z, \sigma)] / \left(\frac{\partial F_k(z, \sigma)}{\partial \sigma}\right)^2 \right)}{N \cdot \partial \sigma} \cdot \frac{\partial \sigma}{\partial F_k(z, \sigma)} \cdot \frac{\partial F_k(z, \sigma)}{\partial z} \\ &= \frac{[1 - 2F_k(z, \sigma)] \left(\frac{\partial F_k(z, \sigma)}{\partial \sigma}\right)^2 - 2F_k(z, \sigma)[1 - F_k(z, \sigma)] \frac{\partial^2 F_k(z, \sigma)}{\partial^2 \sigma}}{N \left(\frac{\partial F_k(z, \sigma)}{\partial \sigma}\right)^4} \cdot \frac{\partial F_k(z, \sigma)}{\partial z}. \end{aligned} \quad (4.13)$$

$$\begin{aligned}
\frac{\partial^2 F_k(z, \sigma)}{\partial^2 \sigma} &= \frac{\partial \left(\sum_{m=1}^{dim(\mathbf{p}_k)} \mathbf{p}_k[m] \left[\frac{2z}{\sigma^3} \exp\left(-\frac{z^2 + \mathbf{a}_k[m]^2}{\sigma^2}\right) \left(\mathbf{a}_k[m] I_1\left(\frac{2z \cdot \mathbf{a}_k[m]}{\sigma^2}\right) - z I_0\left(\frac{2z \cdot \mathbf{a}_k[m]}{\sigma^2}\right) \right) \right] \right)}{\partial \sigma} \\
&= \sum_{m=1}^{dim(\mathbf{p}_k)} \mathbf{p}_k[m] \left\{ \left[\frac{-6z}{\sigma^4} \exp\left(-\frac{z^2 + \mathbf{a}_k[m]^2}{\sigma^2}\right) \left(\mathbf{a}_k[m] I_1\left(\frac{2z \cdot \mathbf{a}_k[m]}{\sigma^2}\right) - z I_0\left(\frac{2z \cdot \mathbf{a}_k[m]}{\sigma^2}\right) \right) \right] \right. \\
&\quad + \left[\frac{2z}{\sigma^3} \left(2 \frac{z^2 + \mathbf{a}_k[m]^2}{\sigma^3} \right) \exp\left(-\frac{z^2 + \mathbf{a}_k[m]^2}{\sigma^2}\right) \left(\mathbf{a}_k[m] I_1\left(\frac{2z \cdot \mathbf{a}_k[m]}{\sigma^2}\right) - z I_0\left(\frac{2z \cdot \mathbf{a}_k[m]}{\sigma^2}\right) \right) \right] \\
&\quad + \left[\frac{-8z^2 \mathbf{a}_k[m]}{\sigma^6} \exp\left(-\frac{z^2 + \mathbf{a}_k[m]^2}{\sigma^2}\right) \left(\mathbf{a}_k[m] I_0\left(\frac{2z \cdot \mathbf{a}_k[m]}{\sigma^2}\right) - \frac{\sigma^2}{2z \cdot \mathbf{a}_k[m]} I_1\left(\frac{2z \cdot \mathbf{a}_k[m]}{\sigma^2}\right) \right) \right. \\
&\quad \left. \left. - z I_1\left(\frac{2z \cdot \mathbf{a}_k[m]}{\sigma^2}\right) \right] \right\}. \tag{4.14}
\end{aligned}$$

$$\begin{aligned}
\frac{\partial F_k(z, \sigma)}{\partial z} &= \frac{\partial \left(1 - \sum_{m=1}^{dim(\mathbf{p}_k)} \mathbf{p}_k[m] \cdot Q_1\left(\frac{\sqrt{2} \mathbf{a}_k[m]}{\sigma}, \frac{\sqrt{2} z}{\sigma}\right) \right)}{\partial z} \\
&= \sum_{m=1}^{dim(\mathbf{p}_k)} \mathbf{p}_k[m] \left[\frac{2z}{\sigma^2} I_0\left(\frac{2z \cdot \mathbf{a}_k[m]}{\sigma^2}\right) \exp\left(-\frac{z^2 + \mathbf{a}_k[m]^2}{\sigma^2}\right) \right]. \tag{4.15}
\end{aligned}$$

4.3.3 CRLB on the Variance of the Proposed Estimator

After gaining the information on the mean and variance of the proposed estimator, the CRLB is derived as a performance reference. Because the measurement error of the empirical CDF is asymptotically normal distributed, the probability density function of the empirical CDF F_E , conditioned on the unknown parameter σ , is given by

$$f(F_E|\sigma) = \frac{1}{\sqrt{2\pi\sigma_F^2}} \cdot \exp\left(-\frac{(F_E - F_k(z, \sigma))^2}{2\sigma_F^2}\right). \tag{4.16}$$

Then, the logarithm of (4.16) is

$$\begin{aligned}
\ln f(F_E|\sigma) &= -\frac{1}{2}\ln 2\pi\sigma_F^2 - \frac{(F_E - F_k(z, \sigma))^2}{2\sigma_F^2} \\
&= -\frac{1}{2}\ln 2\pi - \frac{1}{2}\ln \frac{F_k(z, \sigma)[1 - F_k(z, \sigma)]}{N} \\
&\quad - \frac{N(F_E - F_k(z, \sigma))^2}{2F_k(z, \sigma)[1 - F_k(z, \sigma)]}.
\end{aligned} \tag{4.17}$$

Through tedious but straightforward calculations (given in the appendix), the *Fisher Information* is finally obtained, as presented in (4.18). Then, the CRLB is the inverse of the *Fisher Information*, i.e., $\text{CRLB}(\hat{\sigma}) = 1/I(\hat{\sigma})$. Based on (4.12) and (4.18), the proposed algorithm can achieve the CRLB when the aforementioned assumption holds and the Newton's method converges.

$$\begin{aligned}
I(\hat{\sigma}) &= \text{E} \left[\left(\frac{\partial \ln f(F_E|\sigma)}{\partial \sigma} \right)^2 \right] \\
&= \text{E} \left[\left(\frac{\partial F_k(z, \sigma)}{2 \cdot \partial \sigma} \right)^2 \times \right. \\
&\quad \left. \left(\frac{(N - 2NF_k(z, \sigma))F_E^2 + 2NF_k(z, \sigma)^2 F_E - 2F_k(z, \sigma)^3 + 3F_k(z, \sigma)^2 - F_k(z, \sigma) - NF_k(z, \sigma)^2}{F_k(z, \sigma)^2(1 - F_k(z, \sigma))^2} \right)^2 \right] \\
&= \frac{N \left(\frac{\partial F_k(z, \sigma)}{\partial \sigma} \right)^2}{F_k(z, \sigma)[1 - F_k(z, \sigma)]}.
\end{aligned} \tag{4.18}$$

4.4 Numerical Investigations and Discussion

The performance of the proposed algorithm is firstly investigated through simulations for AWGN channel (i.e., an optical system with only ASE noise and $R_s = B_{ref}$). Throughout this section, the number of samples to build the empirical CDF is 10000, unless otherwise specified. The number of realizations for obtaining the mean and MSE is 50. The investigation is performed for a typical SNR range from 1 dB to 25 dB. On one hand, the ability to

accurately estimate SNR in a low range is vital as it provides alerts of signal quality degradation. On the other hand, the FEC thresholds for the four modulation formats are within this range. More specifically, the SNRs corresponding to a BER of 10^{-2} are approximately 9 dB, 12 dB, 14 dB, and 16 dB for 8-QAM, 16-QAM, 32-QAM, and 64-QAM, respectively.

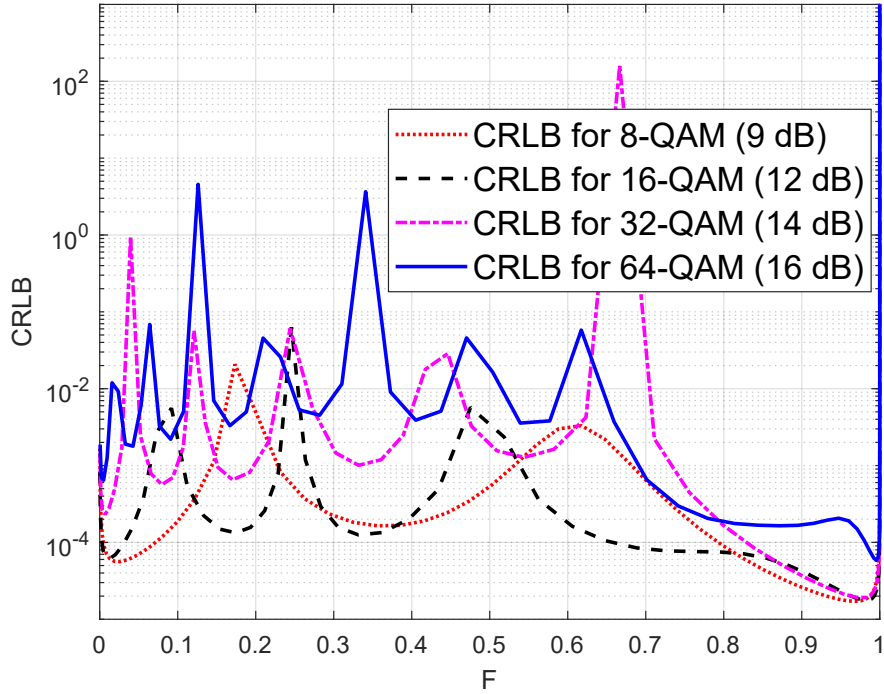
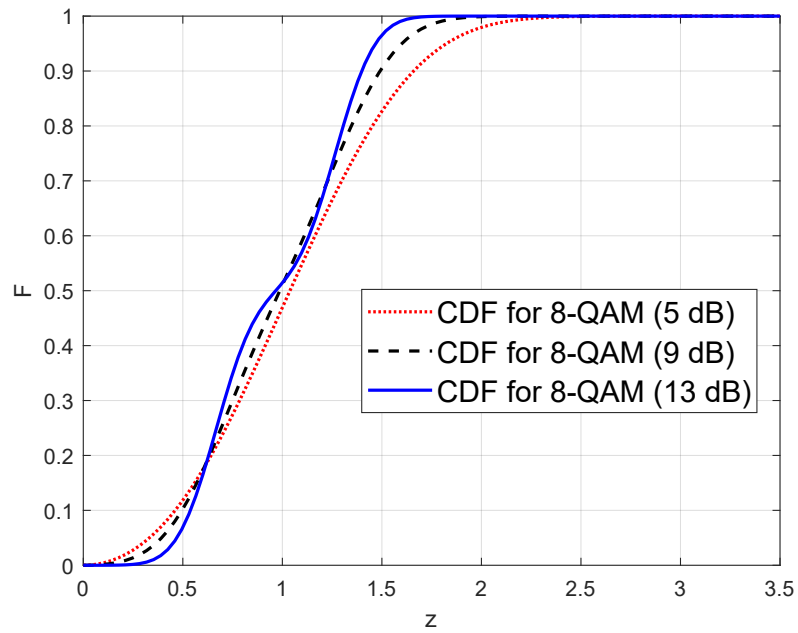


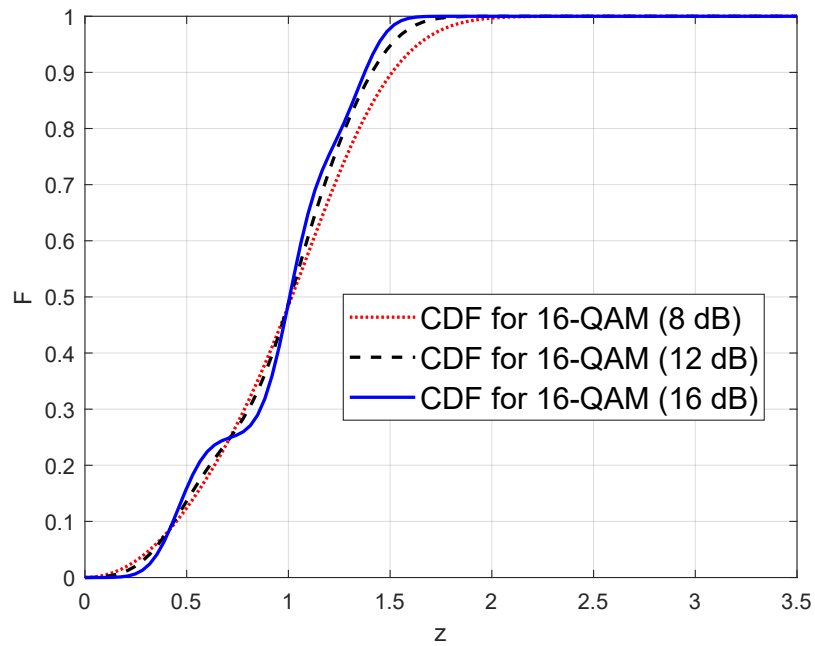
Fig. 4.1: CRLB for different QAMs and SNRs.

4.4.1 Discussion on the CRLB

Based on (4.18), the CRLB relates to the number of samples, the CDF location point z , and the actual σ . 8-QAM, 16-QAM, 32-QAM, and 64-QAM with their FEC threshold SNRs are investigated, respectively. The CRLBs for the four QAM formats are shown in Fig. 4.1. Note that for a more intuitive demonstration, the x-axis here is F instead of z . It can be seen that a smaller CRLB can be attained when F is close to 1 for all the four QAM



(a) CDFs for 8-QAM with different SNRs.



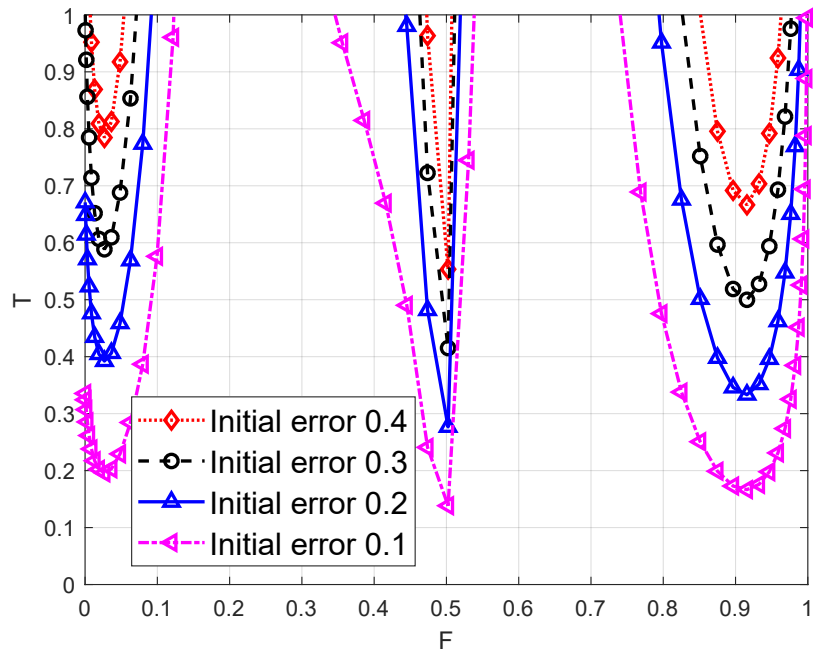
(b) CDFs for 16-QAM with different SNRs.

Fig. 4.2: CDFs for two QAM formats with different SNRs.

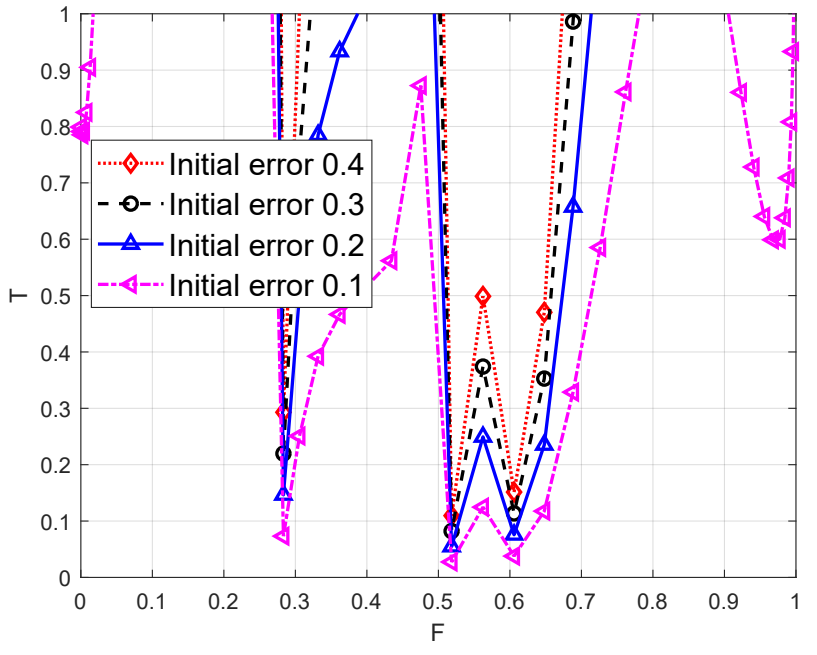
formats. It is also worth noting that several spikes occur at some particular points of F . To explain this observation, the CDFs for different SNRs are shown in Figs. 4.2(a) and 4.2(b) for 8-QAM and 16-QAM, respectively. It can be noticed that the CDFs for different SNRs are close to each other at some particular locations of F , which correspond to the locations of spikes in Fig. 4.1. Similar observations are made for 32-QAM and 64-QAM. It is obvious that using z at these spikes provides limited information for estimating σ , and should be avoided.

4.4.2 Convergence of the Newton's Method

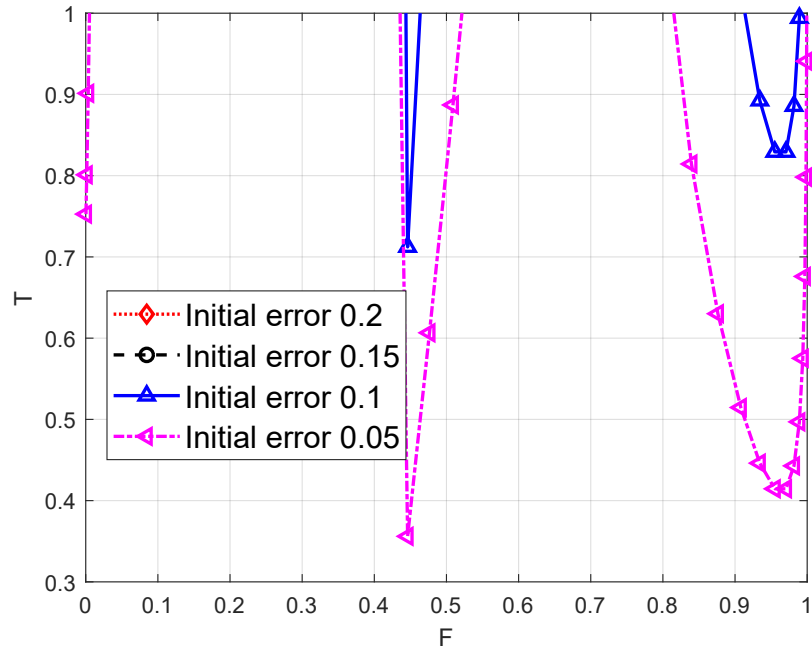
As aforementioned, the initial estimate should be close to the actual value to guarantee the convergence of the Newton's method. The term "close to the actual value" in this context means that (4.9) should be valid. Since T depends on several factors including the unknown actual σ , the cases with typical SNRs of 9 dB, 12 dB, 14 dB, and 16 dB for 8-QAM, 16-QAM, 32-QAM, and 64-QAM are studied, respectively. Figure 4.3 shows the numerical results of T for the four QAM formats with different initial estimate error. It can be seen that an initial estimate closer to the actual value leads to convergence with a wider selection of F (or z alternatively). Furthermore, for higher-order modulation formats such as 64-QAM, it is more important to have an accurate initial estimate. Therefore, a coarse estimation stage is necessary and essential. In the simulations, the coarse estimation includes 4 possible values as $\hat{\sigma}_{coarse} = [0.1, 0.15, 0.3, 0.5]$. Because the convergence requires better initial estimate when the SNR is high, the pre-defined values are not evenly spaced. When the convergence condition is guaranteed, the number of iterations is small due to the quadratic convergence speed. In all simulations, the maximum number of iterations is set to 10.



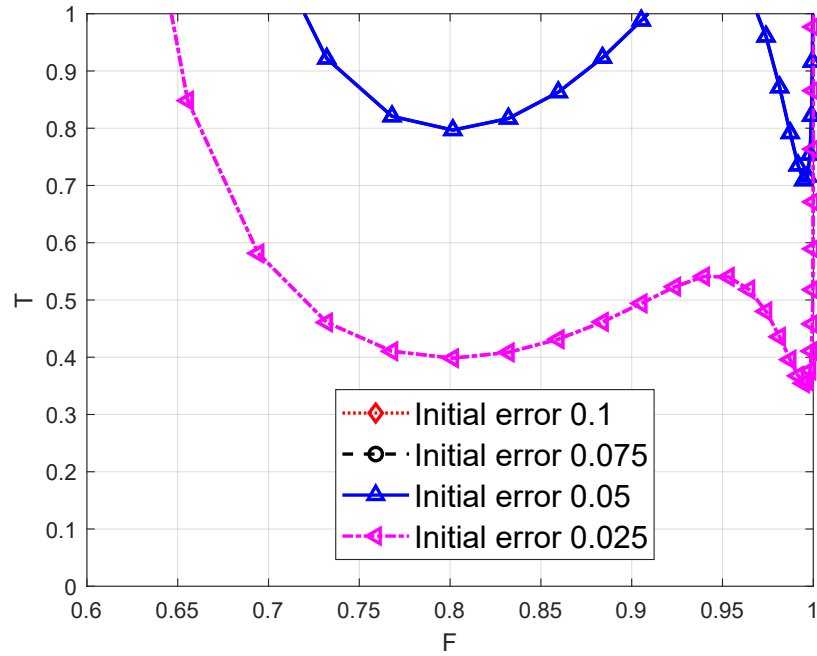
(a) 8-QAM.



(b) 16-QAM.

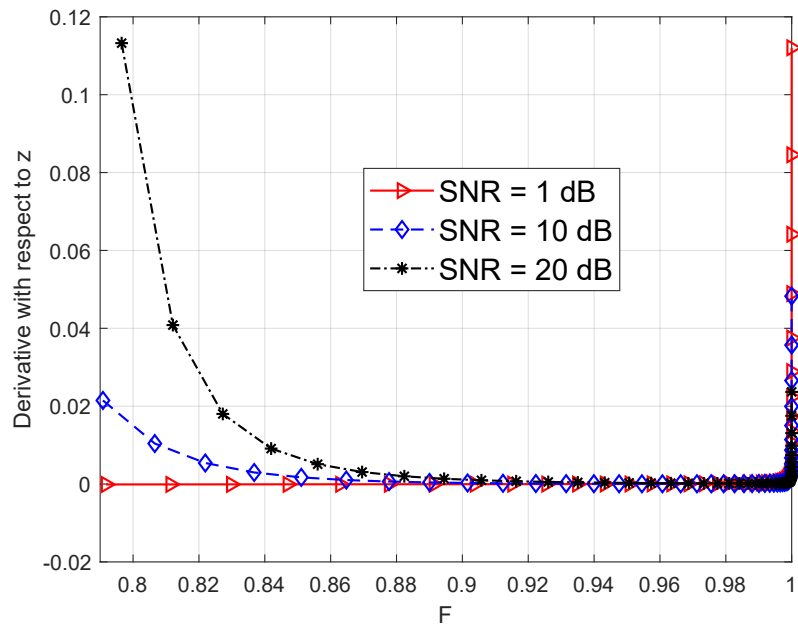


(c) 32-QAM.

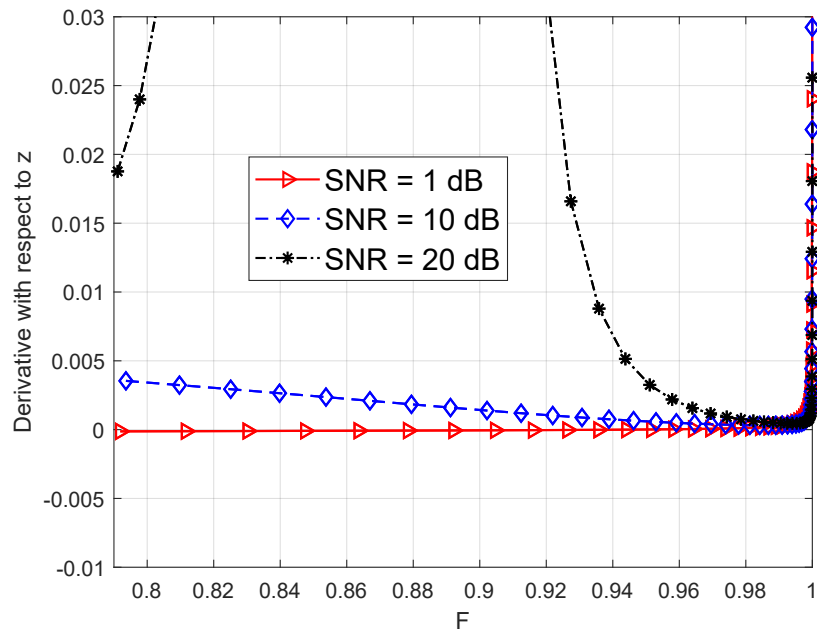


(d) 64-QAM.

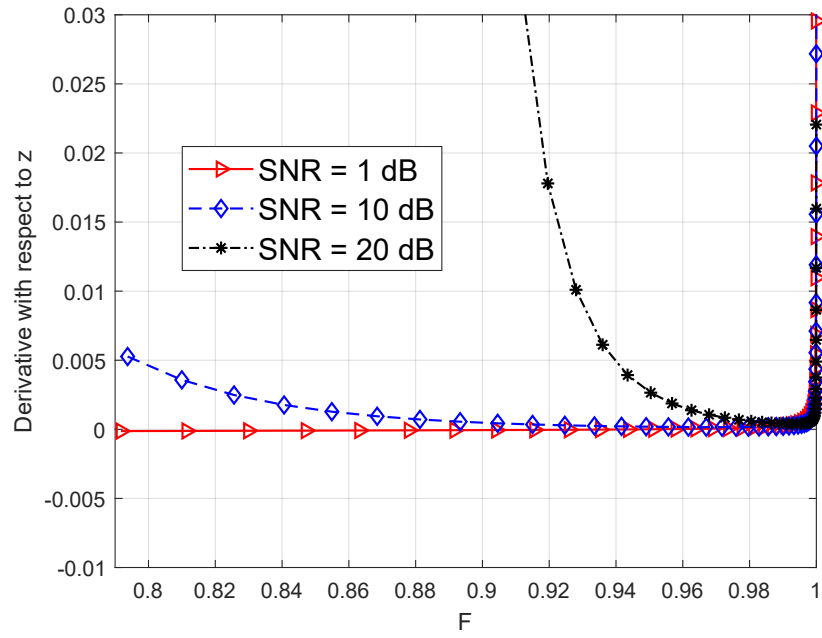
Fig. 4.3: Convergence behavior for the four QAM modulation formats.



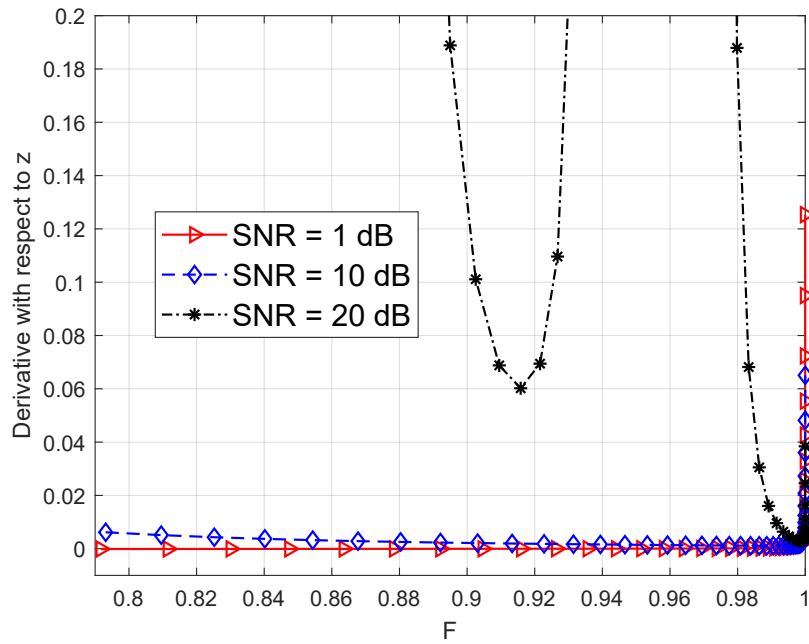
(a) 8-QAM.



(b) 16-QAM.



(c) 32-QAM.



(d) 64-QAM.

Fig. 4.4: Choice of location by investigating derivative with respect to z .

4.4.3 Selection of z

The location on the CDF, z , impacts the accuracy of the estimation. Basically, local extrema can be found by setting (4.13) to zero. However, finding such an optimal or sub-optimal location is challenging since it depends on the actual value of σ , which is unknown. Nonetheless, it is still necessary for the estimation to use the sampling locations where the derivative of (13) is close to zero. According to Fig. 4.1, the lowest CRLB is attained when F is close to 1. Therefore, this particular range of F from approximately 0.8 to 1 is worthy to be investigated. Figure 4.4 shows the numerical value of (4.13) for the four QAM formats with three typical SNRs. The derivative is very large when F is 1. Based on the results, it can be seen that the selection requirement is loose at low SNR, while it is tighter at high SNR. Because the actual SNR is not known, a practical approach for the estimator is to choose a location when F is close to 1, such as $F = 0.99$.

4.4.4 Performance vs. SNR

Figure 4.5 shows the mean and normalized MSE (NMSE) of SNR estimate (i.e., $1/\hat{\sigma}^2$) versus the SNR for the four QAM formats. The NMSE is obtained by normalizing the MSE with respect to σ^2 . Accordingly, the corresponding CRLB is normalized with respect to σ^2 as well.² For reference, results for M2M4 are also displayed. From these results, it can be seen that the proposed algorithm is asymptotically unbiased within SNR ranging from 1 dB to 25 dB, while M2M4 is biased when increasing the SNR. As for the MSE performance, the proposed algorithm approximately achieves the CRLB for the four QAM formats, which agrees with the discussion in Section 4.3. Furthermore, the proposed algorithm outperforms the M2M4 for all four modulation formats in general, impressively in the low and high SNR

²It should be noted that $\text{CRLB}(\hat{\text{SNR}}) = \left(\frac{\partial(1/\sigma^2)}{\partial\sigma}\right)^2 \text{CRLB}(\hat{\sigma}) = 4\sigma^{-6} \text{CRLB}(\hat{\sigma})$, which can be easily shown based on the parameter transformation method for CRLB [77].

range.

4.4.5 Performance vs. Number of Observed Samples

The impact of the number of observed samples is also investigated. The SNRs for 8-QAM, 16-QAM, 32-QAM, and 64-QAM are chosen as 9 dB, 12 dB, 14 dB and 16 dB, respectively. Figure 4.6 shows the mean and variation of the NMSE versus the number of observed samples. As can be seen, the estimate is asymptotically unbiased when the number of observed samples is between 1000 and 10000. In addition, the NMSE decreases for all modulation formats with increasing the number of observed samples, which verifies the analysis in Section 4.3. The proposed algorithm achieves the corresponding CRLB for the four QAM formats, respectively. Note that the algorithm outperforms M2M4 for all modulation formats.

4.5 Numerical Results and Discussions for Nyquist WDM System

The advantages of the proposed algorithm over M2M4 for the AWGN channel have been verified above. In an optical fiber communication system, the linear impairments can efficiently be compensated for, leaving the fiber nonlinearity as the main contributor for system performance degradation. In this section, the performance of the proposed algorithm is investigated for a Nyquist WDM system with various launch powers. The simulation setup is shown in Fig. 4.7. Dual polarization 8-QAM, 16-QAM, 32-QAM, and 64-QAM Nyquist signals at 28 Gbaud with a roll-off factor of 0.01 are generated to modulate an optical carrier through IQM. The carrier is provided by an ECL with 1550.12 nm center wavelength and 100 kHz linewidth. Dual polarization is achieved by employing the PBS and the PBC. Then, the modulated signal from five Tx spaced without any guard band (alternatively speaking,

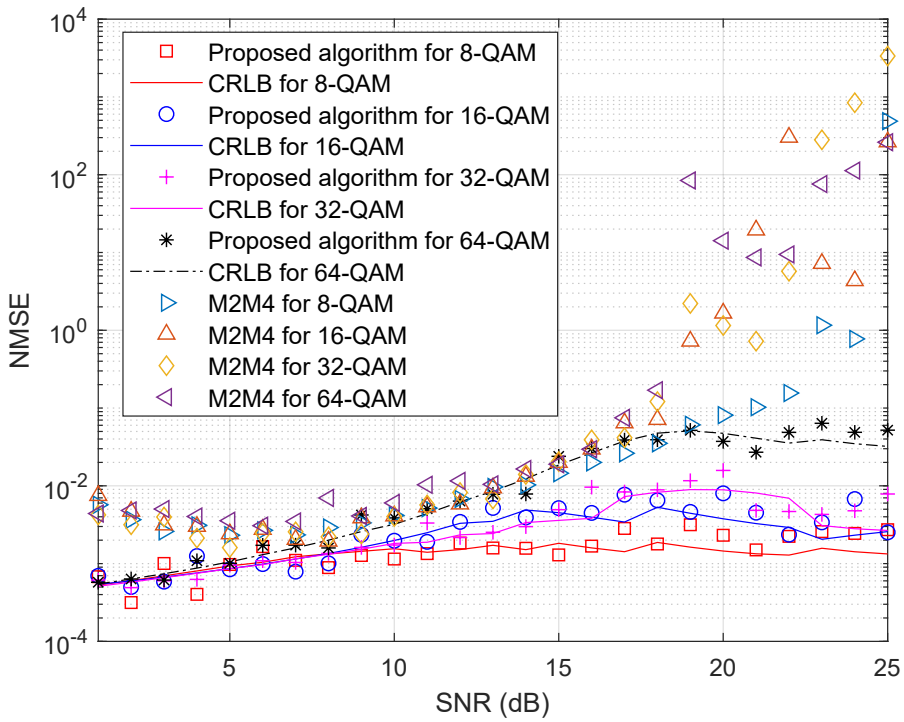
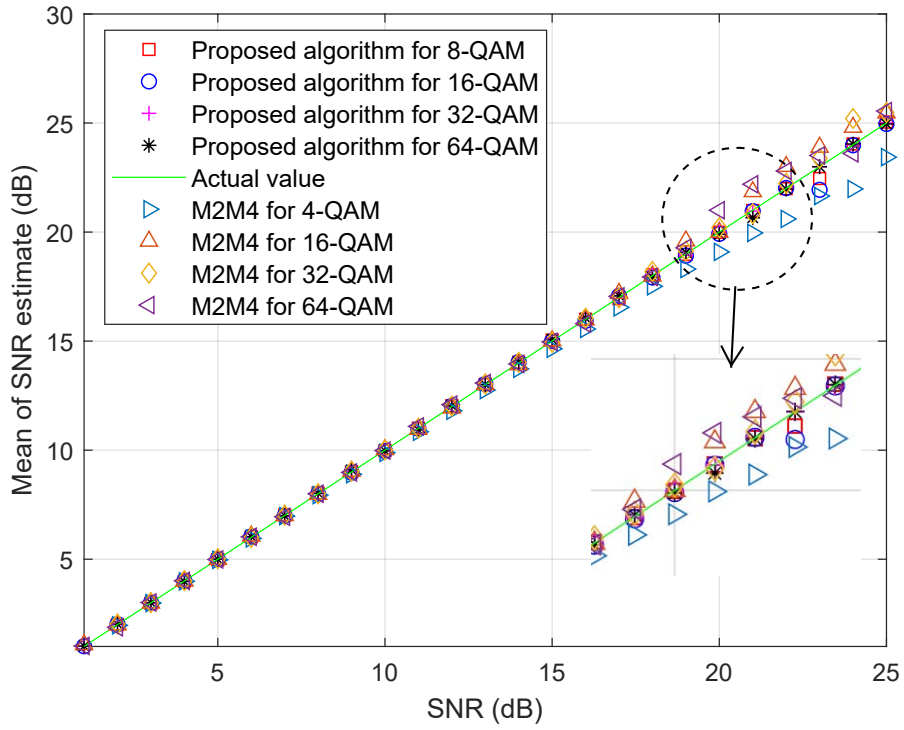


Fig. 4.5: OSNR estimation performance versus SNR.

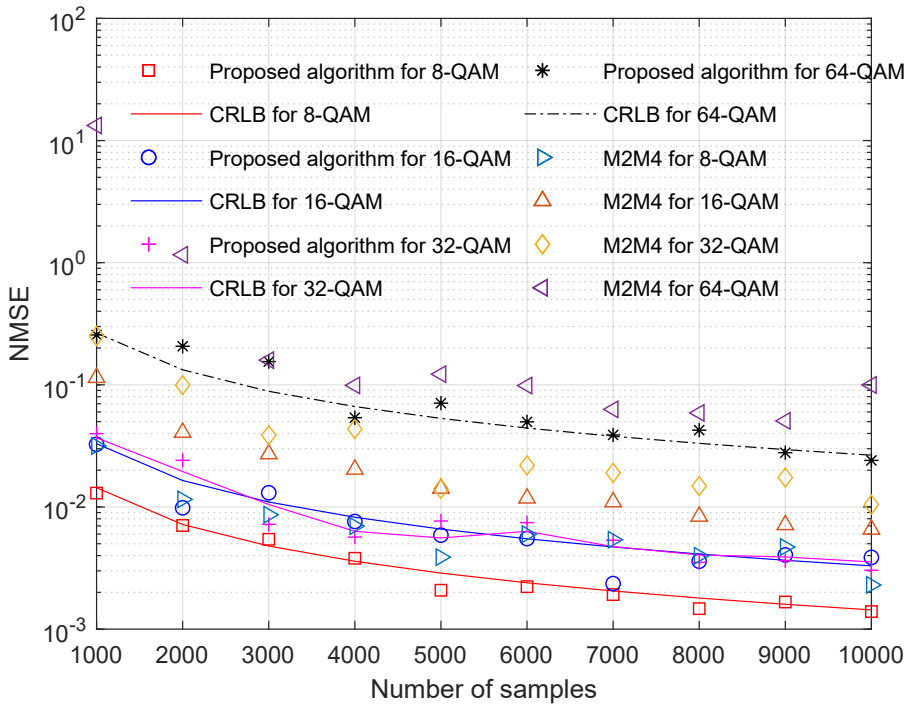
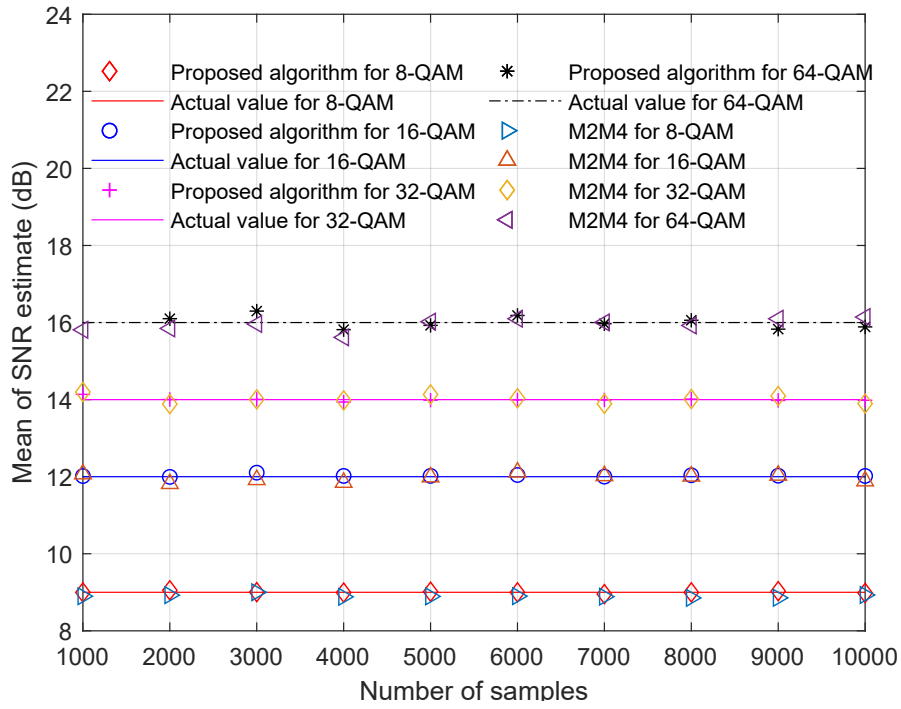


Fig. 4.6: OSNR estimation performance versus number of observed samples.

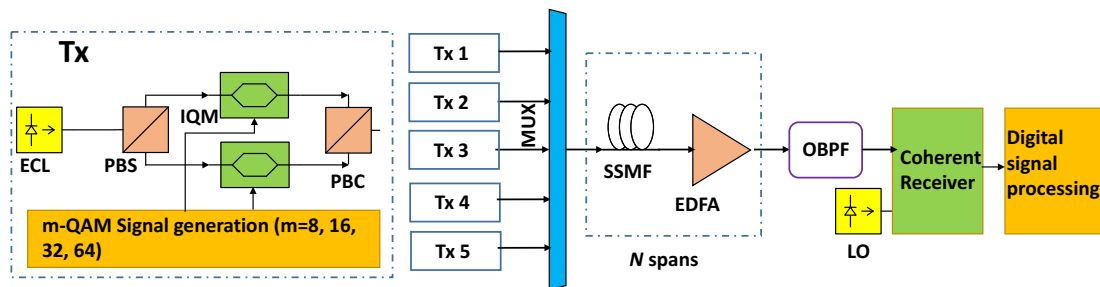
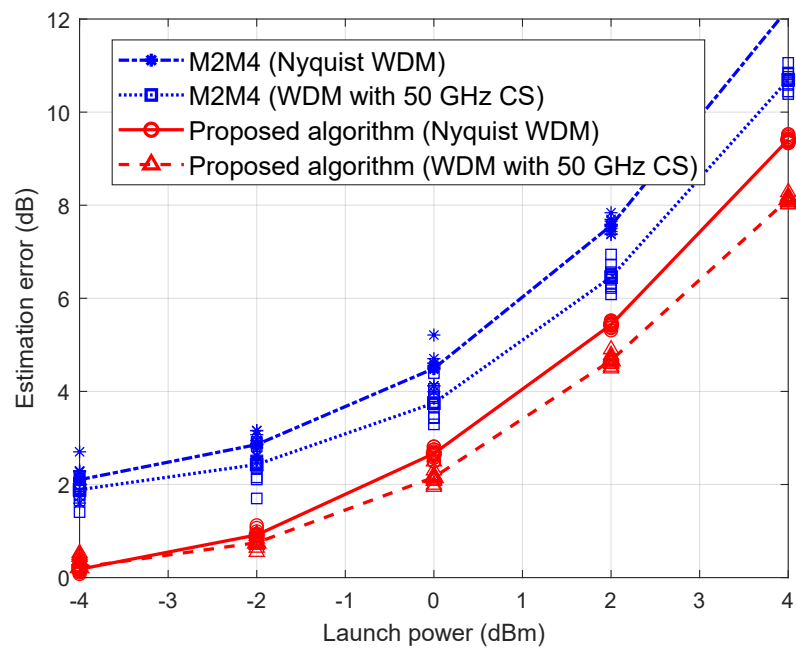
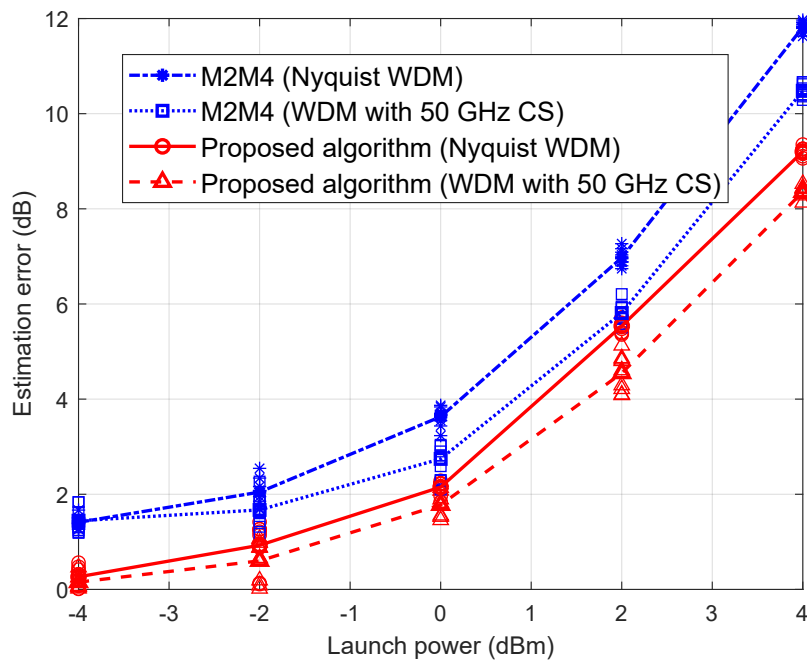


Fig. 4.7: Simulation setup for Nyquist WDM system. Tx: transmitter; PBC: polarization beam combiner; IQM: in-phase quadrature modulator; MUX: multiplexer.

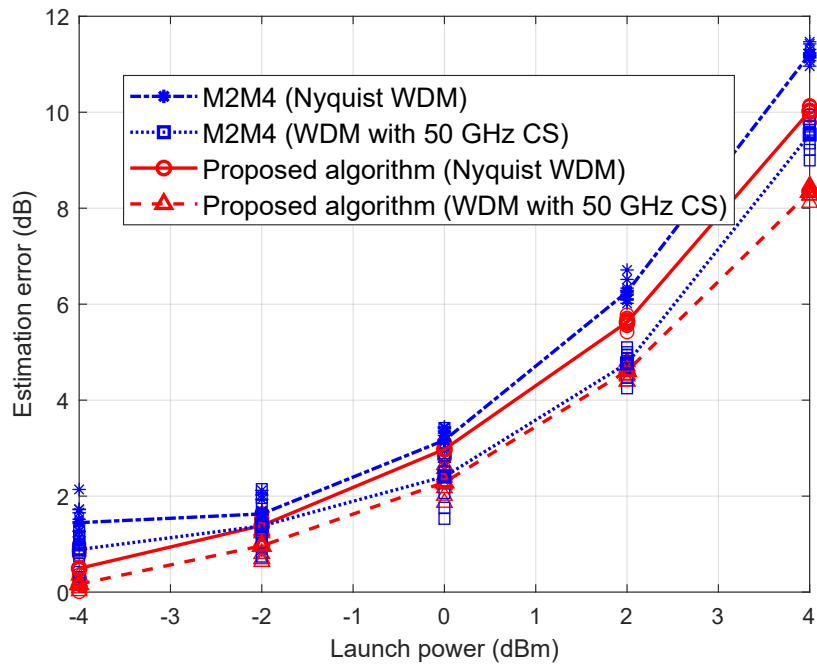
the channel spacing is 28 GHz) is multiplexed and fed into the recirculating loops with SSMF and EDFA. The SSMF is 80 km long with an attenuation coefficient of 0.2 dB/km, a dispersion parameter of 16 ps/nm/km, and a nonlinear coefficient of 1.4 /W/km. The PMD coefficient is 0.1 ps/ $\sqrt{\text{km}}$. The EDFA has a 6 dB noise figure and 16 dB gain. The number of loops for 8-QAM, 16-QAM, 32-QAM, and 64-QAM are 25, 20, 15, and 8, respectively. An LO laser with a linewidth of 100 kHz is used and its frequency offset with respect to the transmitter laser is set to 200 MHz. The received signal is collected and processed off-line. The processing at the receiver includes static equalization for CD compensation and adaptive equalization for polarization demultiplexing. Then, the amplitudes of the processed signal are extracted and used for the SNR estimation. Afterwards, the OSNR is calculated from SNR according to (4.2). In simulation, 10000 samples are employed to obtain the empirical CDF; the launch power varies from -4 dBm to 4 dBm; and 10 realizations are performed for each launch power. The OSNR estimation error in dB is presented in Fig. 4.8, where the mean values of the estimation error are connected by curves. For reference, results for a WDM system with 50 GHz channel spacing are also shown. According to Fig. 4.8, both the proposed algorithm and M2M4 are affected when the launch power increases. This is due to fiber nonlinearity, which results in Gaussian noise-like non-linear interference



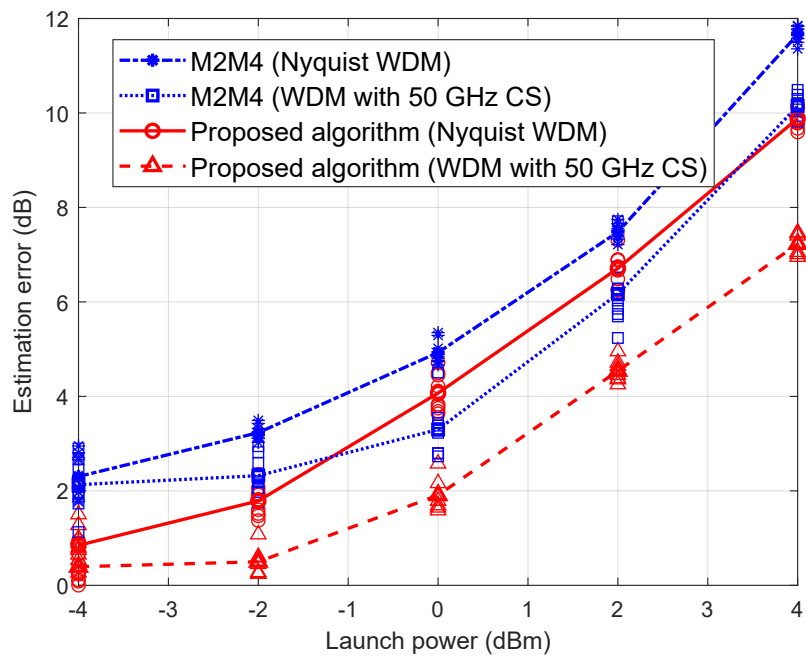
(a) 8-QAM (No. of loops = 25).



(b) 16-QAM (No. of loops = 20).



(c) 32-QAM (No. of loops = 15).



(d) 64-QAM (No. of loops = 8).

Fig. 4.8: OSNR estimation error (dB) versus launch power. CS: channel spacing.

(NLI) to the signal [78]. In such case, the SNR is given by

$$\text{SNR}_{total} = \frac{P_{ch}}{P_{ASE} + P_{NL}}, \quad (4.19)$$

where P_{ch} , P_{ASE} , and P_{NL} represent the signal power, ASE noise power, and NLI power, respectively. The proposed algorithm and M2M4 estimate the total variance, i.e., the denominator part of (4.19). However, because the OSNR is defined by measuring the impact from the ASE noise without considering NLI, the estimated OSNR becomes biased when increasing the launch power, as shown in Fig. 4.8. Furthermore, when the channel spacing increases from 28 GHz to 50 GHz, the inter-channel NLI reduces and the performance of both algorithms improves. Nonetheless, it is noticed that the proposed algorithm is more robust to fiber nonlinearity than M2M4. Similar to M2M4, the proposed algorithm can be combined with the approach from [68] to improve the performance in the presence of fiber nonlinearity. On the other hand, high OSNR does not guarantee that the signal quality is good. When the OPM requires the information on the signal characteristics affected by both ASE and fiber nonlinearity, estimating SNR_{total} is important. Accordingly, the proposed algorithm is suitable for such practical case.

4.6 Complexity Analysis

The complexity of the proposed algorithm is analyzed, taking into account both the coarse and fine estimation stages. Assume that N samples are observed, the number of bins used for CDF is B , the number of iterations is P , and the number of coarse estimate candidates at the first stage is J . Since the second stage is an iterative process, only one iteration is needed to be analyzed for the computational complexity. With the signal's amplitude as input, Table 4.1 shows the computational complexity for the proposed algorithm and M2M4. It can be seen that M2M4 requires a number of real multiplications and additions of $4N$ and

$2N$, respectively, as it involves power operation for each sample. On the other hand, the proposed algorithm (both the coarse and fine stage) employs the CDF with a bin number of B , which is significantly smaller than N . With $N = 10000$, $P = 10$, $B = 100$, and $J = 4$ in the simulations, the proposed algorithm attains better performance with significantly less real multiplications, though with more additions and look-up table operations. The details are presented in Table 4.2. Furthermore, it should be noted that real multiplications require significantly more computational resources than real additions [79]. Overall speaking, the proposed algorithm involves less complexity compared to M2M4.

Table 4.1: Complexity for the proposed algorithm and M2M4.

		Multiplications	Additions	Look-up table operations
Proposed algorithm	Coarse stage	0	$(2B + 1)J + N\log B$	JB
	Fine stage	$2P$	$2P$	$2P$
	Overall	$2P$	$(2B + 1)J + N\log B + 2P$	$2P + JB$
M2M4		$4N$	$2N$	0

Table 4.2: Complexity with typical values for the proposed algorithm and M2M4.

		Multiplications	Additions	Look-up table operations
Proposed algorithm	Coarse stage	0	70804	400
	Fine stage	20	20	20
	Overall	20	70824	420
M2M4		40000	20000	0

4.7 Feasibility to PCS Systems and TDHM Systems

Non-uniformly distributed QAM constellations, such as PCS QAMs and time domain hybrid modulations (TDHM) QAMs, are also very popular in current designs in order to achieve an improved trade-off between capacity and required OSNR. The proposed algorithm is applicable for the two systems. The reasons are presented in the sequel.

Taking PCS 64-QAM as an example, the possible amplitudes for its constellation are the same as uniformly-distributed 64-QAM and denoted as $\mathcal{M}_{ps} = \{1/\sqrt{42} (\sqrt{2}, \sqrt{10}, \sqrt{18}, \sqrt{26}, \sqrt{34}, \sqrt{50}, \sqrt{58}, \sqrt{74}, \sqrt{98})\}$. Accordingly, the amplitudes of the transmitted signal, \mathbf{a}_n , represent a sequence drawn from \mathcal{M}_{ps} with probability \mathbf{p}_{ps} . The probabilities for the elements in \mathcal{M}_{ps} depend on the system configuration and are denoted as $\mathbf{p}_{ps} = [p1_{ps}, p2_{ps}, p3_{ps}, p4_{ps}, p5_{ps}, p6_{ps}, p7_{ps}, p8_{ps}, p9_{ps}]$. By providing the designed probabilities for different amplitudes, all the calculations aforementioned can be applied as well.

Without loss of generality, an TDHM system with 4-QAM and 16-QAM is considered, which has equal duration for each QAM. The constellation is shown in Fig. 4.9, where the red dots represent 4-QAM signal, and the blue dots represent 16-QAM signal. Since the duration is identical for both QAM formats, the probability of each dot is uniform. According to the constellation, there are three amplitudes $(\sqrt{2/10}, 1, \sqrt{18/10})$, and the probabilities for the amplitudes are 1/5, 3/5, and 1/5, respectively. for an unevenly-composited TDHM QAM formats, one can attain the amplitudes and corresponding probabilities by similar reasoning, given the uniform QAM formats and their durations. Therefore, the proposed algorithm is applicable for TDHM QAM formats as well.

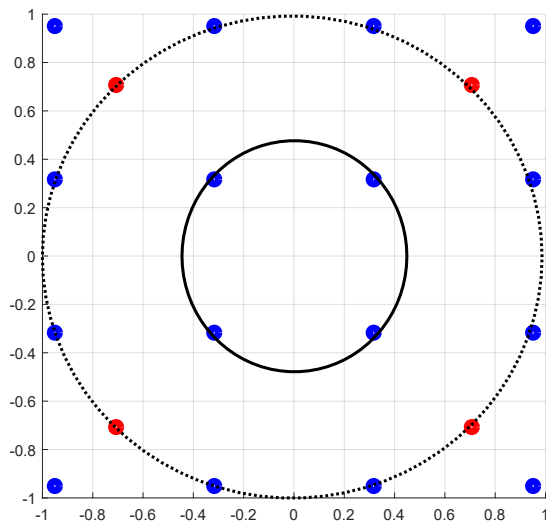


Fig. 4.9: Constellations for TDHM with 4-QAM and 16-QAM.

4.8 Summary

Although the moment-based OSNR estimation algorithm is an attractive choice due to its robustness to frequency offset and laser phase noise, it is only efficient for constant modulus constellations. In this chapter, an OSNR estimation algorithm based on the empirical CDF of the received signal's amplitude has been proposed, which can be efficiently implemented with significantly reduced complexity. The proposed algorithm first acquires a coarse estimate of the noise variance from several predefined values; then, a fine estimate is obtained by using the Newton's method. Mathematical analysis shows that the estimator achieves the CRLB, and extensive numerical investigations verify its improved performance over the conventional M2M4. Above all, the proposed algorithm is compatible with standard digital signal processing procedures without requiring any additional overhead. The advantages in terms of both performance and complexity over M2M4 make the proposed algorithm an appealing NDA OSNR estimation option for optical fiber communications systems employing spectral-efficient multilevel constellations.

Chapter 5

Joint Modulation Classification and OSNR Estimation for Coherent Optical Systems

5.1 Background

Chapters 3 and 4 only tackle one task each: either MC or OSNR estimation. The proposed algorithms for the two task both employ the CDF of the signal's amplitude as the feature. System complexity can be reduced if the two parameters are determined jointly. Recently, joint estimation of the modulation format and OSNR by employing machine learning (ML)-based algorithms have been reported. Artificial neural networks and principal component analysis are used in heterogeneous fiber-optic networks for modulation format identification and OSNR estimation [80]. Utilizing eight features that are extracted from the direct-detected eye-diagram, [81] applies neural networks and support vector machine (SVM) to estimate the OSNR and classify the modulation format, respectively. However, these

methods exploit statistical features of directly detected signals, and are not applicable to dispersion-unmanaged coherent optical systems. In [82], deep neural networks (DNN) are applied to identify the modulation format and monitor the OSNR based on the histograms of the signal's amplitude. However, the OSNR monitoring is performed after the MC. Therefore, a misclassification of the modulation format can result in failure of the OSNR estimation.

In this chapter, an algorithm enabled by SVM is proposed to jointly classifies the modulation format and estimate the OSNR. Compared with neural networks, SVM has the advantage of a stronger ability to find the global minimum and of being insensitive to the over-fitting problem [83]. Moreover, SVM is considered computationally efficient compared with many other kernel-based algorithms because it stores only support vectors, which is a subset of the training matrix [81]. It is proven that SVM exhibits strong ability in classifications and regression in optical fiber communication systems [81, 84]. The CDF is used widely in applications to differentiate the distribution, such as in the well-studied Kolmogorov-Smirnov test [76]. In wireless communication systems, the CDF of the received signal is usually applied to identify the modulation format [49]. In this paper, the CDF of the received signal after polarization demultiplexing is used as the feature for SVM. Compared with the constellation used in [62], the CDF reduces the dimensionality of the feature space. In order to analyze the capability of the proposed algorithm, both numerical simulations and experiments are carried out. QAM formats are widely used in coherent optical communications due to their spectral efficiency [82]. Three modulation formats, namely, 4-QAM, 16-QAM, and 64-QAM, as well as the OSNR ranges of interest are considered. The results show that the algorithm achieves good performance for the multi-parameter estimation tasks.

5.2 Proposed Algorithm

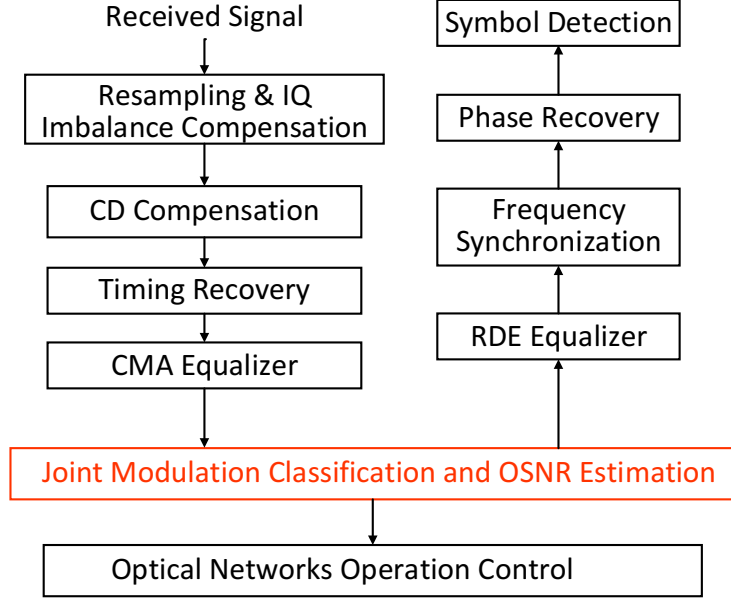


Fig. 5.1: DSP structure including the joint MC and OSNR estimation subsystem.

The DSP flow in the coherent receiver, including the proposed algorithm, is presented in Fig. 5.1. Note that the algorithms before the joint MC and OSNR estimation subsystem are modulation format-independent. The signal affected by the frequency offset, phase noise, and the ASE noise after the CMA equalizer can be express as in (4.1).

The CDFs for different QAM formats and different OSNRs are distinct, as shown in Fig. 5.2. A specific CDF can indicate the corresponding modulation format and OSNR, especially in higher OSNR range. To identify the modulation format and estimate the OSNR, an SVM-based algorithm is proposed. The proposed algorithm employs support vector classifier (SVC) and support vector regressor (SVR) to address the MC and OSNR estimation task, respectively. The schematic of the algorithm is shown in Fig. 5.3. Unlike the DNN-based algorithm in [82], the MC and OSNR estimation are performed simulta-

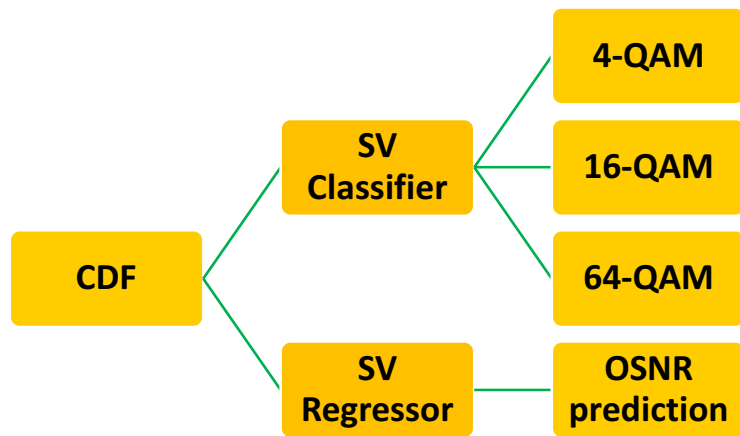
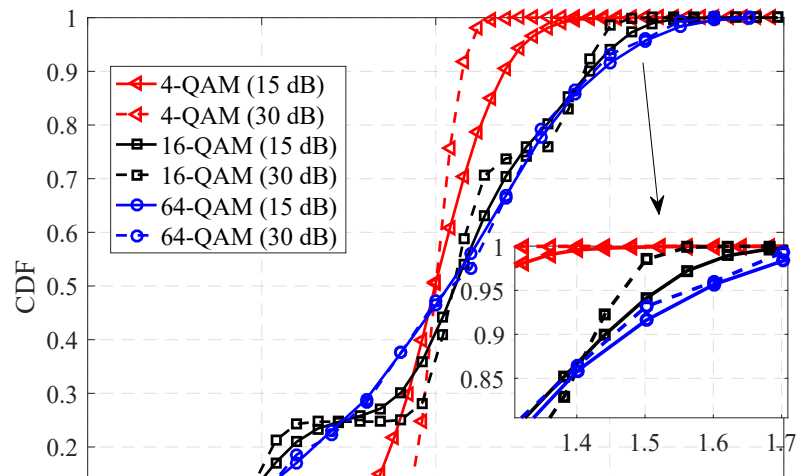


Fig. 5.3: SVM-based classifier and regressor.

neously. In general, both classifier and regressor establish a mapping model between the training data and the label, according to the extracted features. Once the mapping is built, the testing data is determined and labeled.

For the training of the SVC and SVR, a group of training CDFs are firstly generated, which correspond to all possible modulation format candidates and OSNRs. Each CDF is represented by the bin-count vector \mathbf{x} , and the corresponding labels are: y_1 for modulation type and y_2 for the OSNR value. More specifically, $y_1 = 0, 1, 2$ represents 4-QAM, 16-QAM, and 64-QAM, respectively. For the classification tasks, the one-over-rest strategy is applied to perform the three-class SVC [85]. Kernel function is used to map the training data into a higher dimensional space, where a hyperplane is built to distinguish the target class from the rest of classes. For OSNR estimation, an epsilon-SVR [85] is used to construct a mapping based on the input vectors and their corresponding scalar labels. After the supervised training procedure, a group of testing data sets is utilized to evaluate the behavior of the SVM-based system. The output \hat{y}_1 indicates the modulation format, while the output \hat{y}_2 provides the estimated OSNR value. Lastly, both classification and estimation outputs are compared with actual ones, respectively. After the module of joint MC and OSNR estimation, the acquired information on the modulation format is beneficial for the following DSP procedures, such as carrier phase recovery and symbol detection. On the other hand, the estimated OSNR provides feedback to the networking operation decision. For example, when the OSNR is high enough, reducing the transmit power can improve the tolerance to fiber non-linearity and still meet the desired BER requirements; alternatively, a higher modulation format can be adopted to increase the data rate. It should be noted that, the training procedure of the proposed algorithm is carried out offline and beforehand. Thus the actual OSNR estimation and MC process in an optical network employing trained SVM does not cause any overhead.

5.3 Performance Evaluation

In this section, the performance of the proposed algorithm is evaluated by numerical simulations and experiments.

5.3.1 Simulation Results and Discussion

To begin with, the performance of the proposed algorithm is investigated through numerical simulations. The simulation model considers a 32 Gbaud PDM system. 800 km standard single mode fiber with typical CD and PMD is used as in [70]. The attenuation and fiber nonlinearity are neglected to simplify the investigations. The OSNR is adjusted by loading the noise. The frequency offset is 1 GHz, and the linewidth of the lasers is 100 kHz. At the receiver, 10000 samples after the CMA equalizer are used to create the CDF. Note that the bin size is 100. A data set including 78 CDFs that correspond to 3 modulation candidates and 26 OSNRs (from 5 dB to 30 dB, with a step size of 1 dB) are generated to train the classifier and regressor. Throughout the paper, the OSNR is measured with a noise reference bandwidth of 0.1 nm, and the corresponding SNR is provided in the results.

For the SVM-based algorithm, the open-source LIBSVM is employed [85]. In the simulation, the kernel function is the default radial basis function kernel. In addition, the 5-fold cross-validation method is used to ensure the model fits the training data well. The cross validation divides the training data set into 5 subsets with identical size. Then, 4 subsets are utilized for the training process, while 1 subset is used for validation. This procedure occurs 5 times, and eventually the model is summarized based on the five iterations. Figure 5.4 illustrates the 5-fold cross validation, and more details can be found in Chapter 5 of [86]. Once the training is finished, a testing data set is generated to evaluate the performance. 100 realizations are performed for each OSNR value and each modulation format, therefore the number of total testing CDFs is 7800. Simulations for DNN is also conducted as

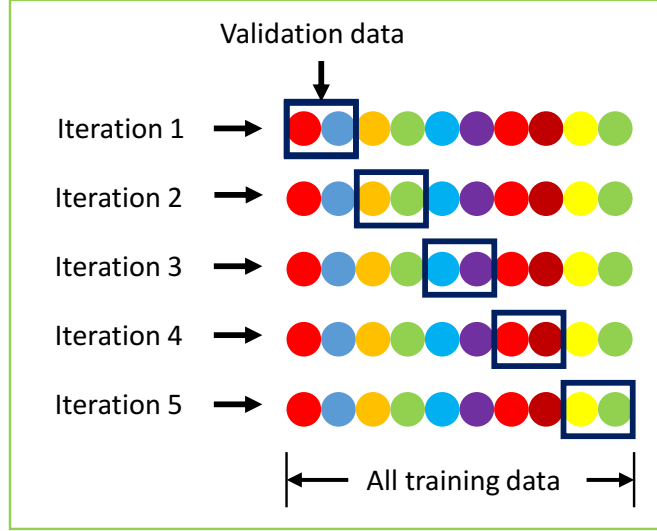


Fig. 5.4: Illustration of the 5-fold cross validation.

a reference by using the same training and testing data. The DNN structures are based on [82], which includes two hidden layers. Optimization for the numbers of neurons in the hidden layers is performed using grid searching. The number of neurons varies from 5 to 80 with a step size of 5, and the combination providing the best results is selected. The final parameters are shown in Table. 5.1.

Figure 5.5 demonstrates the MC accuracies for the three modulation formats. The proposed algorithm requires 5 dB, 17 dB, and 5 dB to achieve 100% correct MC rate for 4-QAM, 16-QAM, and 64-QAM, respectively. It is worth mentioning that the errors for 16-QAM come from the misclassification with 64-QAM, because the CDF shape for 64-QAM within a wide OSNR range is similar to that of 16-QAM at lower OSNR. In the case of modulation classification, during the training stage, the training data are signals with 3 modulation formats spanning a wide range of OSNR. Within this OSNR range, CDFs for 4-QAM change obviously, but are still distinct; CDFs for 64-QAM change relatively unnoticeably; CDFs for 16-QAM are distinct in high OSNR, while close to 64-QAM in

Table 5.1: Parameters of optimized DNNs.

	Hidden layer 1	Hidden layer 2
Modulation classification	10	30
OSNR estimation for 4-QAM	60	10
OSNR estimation for 16-QAM	50	10
OSNR estimation for 64-QAM	60	10

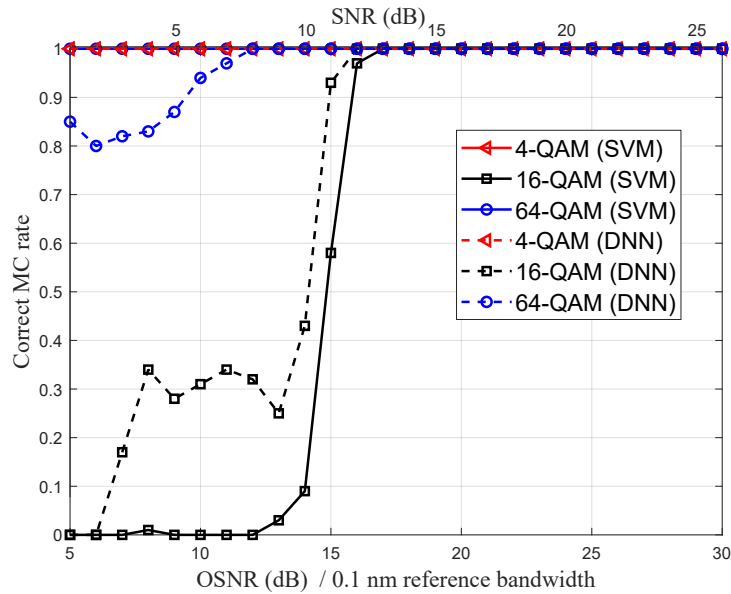


Fig. 5.5: Correct modulation classification rate vs. OSNR.

lower OSNR. Fig. 5.2 demonstrates this trend. Alternatively speaking, the CDF shape for 64-QAM over a wide OSNR range is similar to that of 16-QAM at lower OSNR. When this kind of CDFs are obtained, the SVM tends to decide the modulation format as 64-QAM to reduce the overall chance of misclassification. Note that the OSNR of the test signal is unknown when the modulation classification is performed. On the other hand, the theoretical SD FEC thresholds corresponding to a BER of 2.4×10^{-2} in 32 Gbaud dual-

polarization systems for 4-QAM, 16-QAM, and 64-QAM are around 10 dB, 16 dB, and 22 dB, respectively. As can be seen, both SVM-based and DNN-based algorithms achieve virtually 100% correct classification for the three modulation formats at OSNRs below their corresponding FEC thresholds.

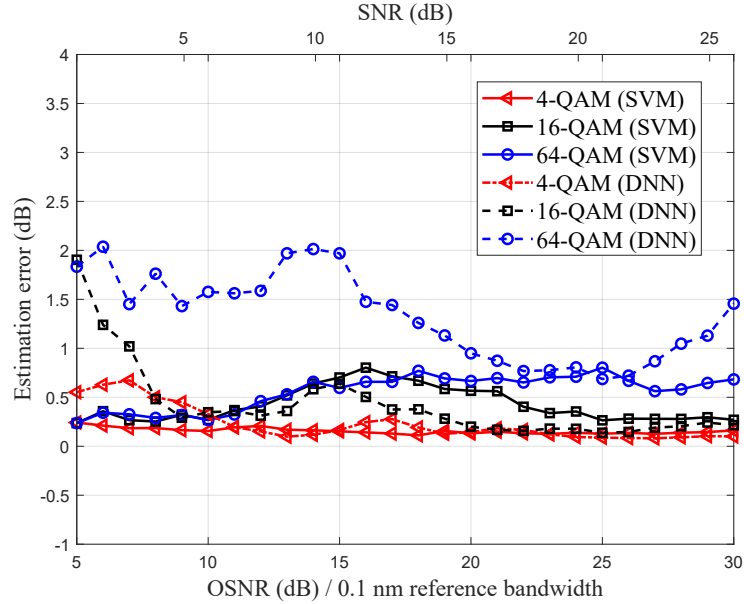
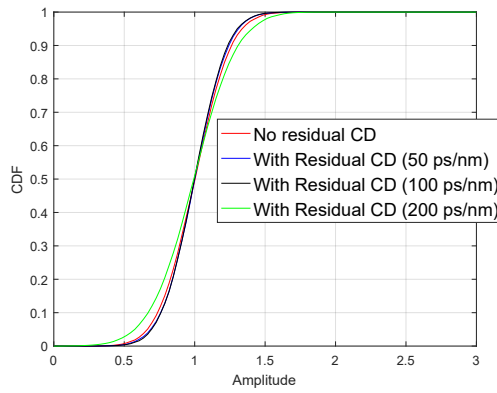


Fig. 5.6: Mean of estimated OSNR vs. actual OSNR.

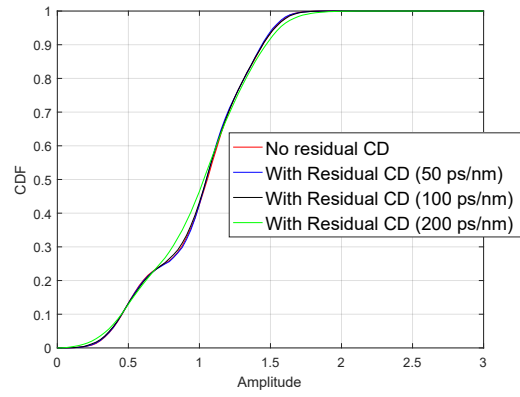
Figure 5.6 shows OSNR estimation errors versus the actual OSNR for the three modulation formats. It is observed that, compared with the proposed algorithm, estimation by the DNN-based algorithm exhibits more errors. The proposed algorithm attains maximum estimation errors of 0.24 dB, 0.8 dB, and 0.8 dB for 4-QAM, 16-QAM, and 64-QAM, respectively; however, the maximum estimation errors obtained by the DNN-based algorithm for the three modulations formats are higher, namely, 0.67 dB, 1.9 dB, and 2.05 dB, respectively. Generally speaking, DNN requires relatively large training data set to learn nonlinear transformations. Alternatively, it could suffer performance degradation when training data sets are relatively small.

The transmission in EON could embed some dispersive distortion such as the residual chromatic dispersion, which widens the pulses and causes inter-symbol interference. As a result, the amplitude of the received signal is affected. Fig. 5.7 shows the CDFs with three residual CD amounts. Specifically, Fig. 5.7 (a), (b), and (c) show the CDFs for 4-QAM, 16-QAM, and 64-QAM, all with the residual CD amounts of 50 ps/nm, 100 ps/nm, and 200 ps/nm. The OSNR are 14 dB, 18 dB, and 24 dB, respectively. It can be seen that the CDFs change slightly with a residual CD of 50 ps/nm, while a considerable deviation is observed when the residual CD is 200 ps/nm. Therefore, severe residual CD could result in performance degradation. However, it should be mentioned that many algorithms have been proposed to estimate the residual CD in elastic optical network systems, which will eliminate the impact of the residual CD on the following signal processing modules [26]. In addition, an adaptive equalizer like CMA also compensates some amount of the residual CD. To further investigate the robustness of the proposed algorithm, simulation verification is performed with a residual CD of 100 ps/nm. MC and OSNR estimation results are shown in Fig. 5.8 and Fig. 5.9, respectively. In Fig. 5.8, the correct MC rates for 4-QAM, 16-QAM, and 64-QAM at the FEC thresholds are 100%, around 92%, and 100%, respectively. In Fig. 5.9, the OSNR estimation error versus OSNR is shown. One can notice that the mean of the estimation error for the three modulation formats are still within 1 dB. In general, the proposed algorithm is still applicable in the presence of a moderate amount of residual CD.

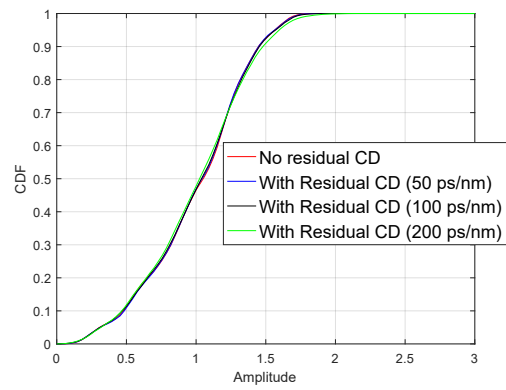
It is worth noting that the proposed algorithm performs MC and OSNR estimation simultaneously, i.e., the estimation of OSNR does not rely on the prerequisite knowledge of modulation format. On the other hand, the DNN-based algorithm achieves them sequentially, starting with MC. The proposed algorithm can avoid estimation errors if misclassification occurs. Indeed, such OSNR estimation error can not be ignored. Supervised learning



(a) 4-QAM



(b) 16-QAM



(c) 64-QAM

Fig. 5.7: Impact of residual CD on CDF.

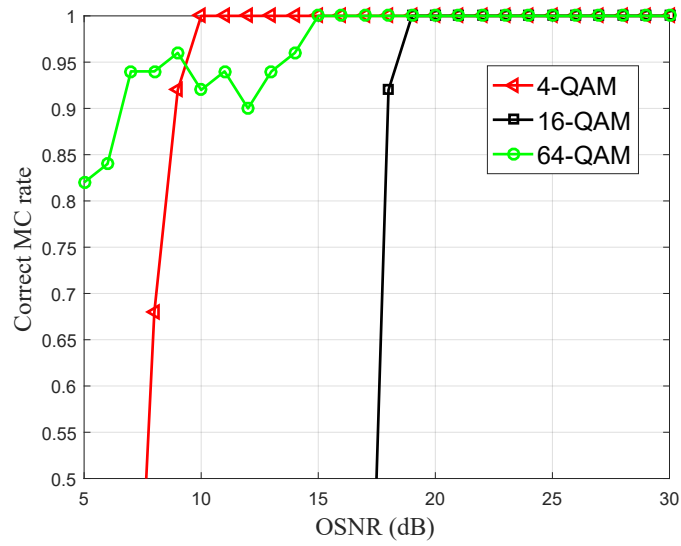


Fig. 5.8: MC performance when the residual CD is 100 ps/nm.

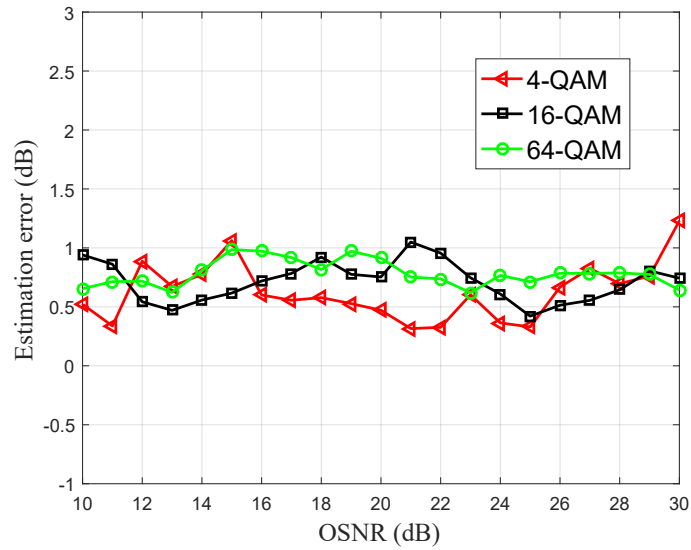


Fig. 5.9: OSNR estimation performance when the residual CD is 100 ps/nm.

algorithms, such as the DNN, perform a prediction based on the training data. It is difficult for the DNN to predict a category of data when it is trained by a different data category. For example, a training data set including CDFs for 16-QAM will help the DNN establish a mapping relationship between the OSNRs and the CDFs for 16-QAM only. When CDFs for 4-QAM is tested, the DNN will generate error in the OSNR prediction, since the CDFs for 4-QAM and 16-QAM are distinct from each other, as can be seen in Fig. 5.2. To illustrate that, simulation results are provided in Fig. 5.10. One can see that the estimation error is not negligible especially at high OSNR, where the CDFs for different modulation formats are distinguishable. When 64-QAM is misclassified as 16-QAM, simulation results show a maximum OSNR estimation error of about 7 dB, as it is difficult for the DNN to predict a category of data when it is trained by another category.

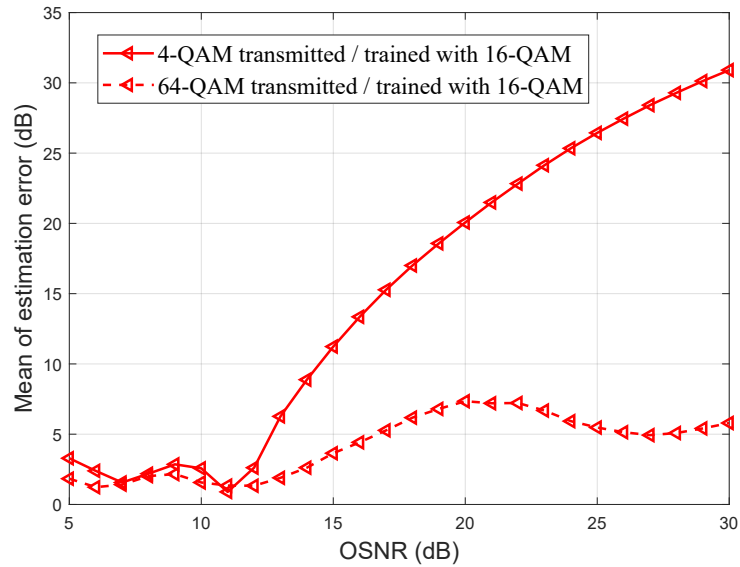


Fig. 5.10: The OSNR estimation error when modulation misclassification occurs.

Table 5.2: Experimental results for MC.

	Transmitted MF	Classified MF		
		4-QAM	16-QAM	64-QAM
SVM / DNN	4-QAM	45 (100%)	0	0
	16-QAM	0	33 (97%)	1 (3%)
	64-QAM	0	0	29 (100%)

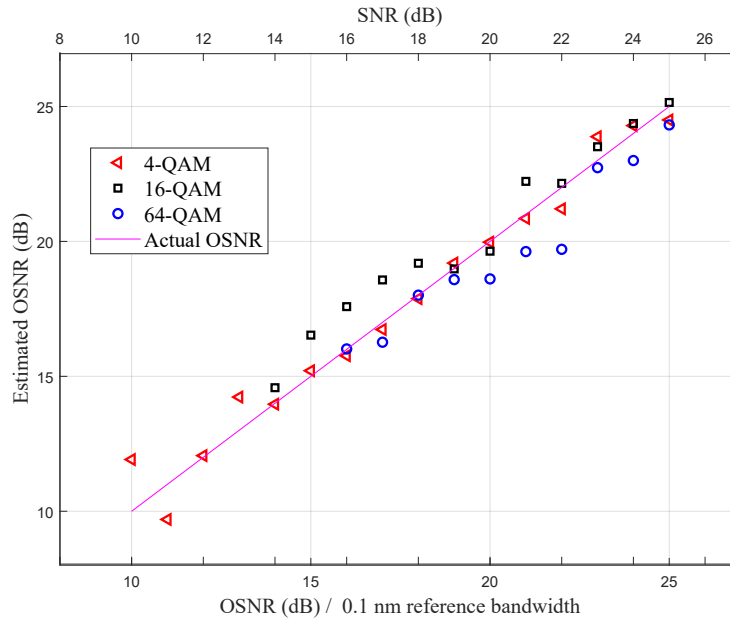


Fig. 5.11: Experimental results for OSNR estimation.

5.3.2 Experimental Results and Discussion

The experimental setup of the dual-polarization optical B2B system is similar to the one in Chapter 3. The OSNR ranges for 4-QAM, 16-QAM and 64-QAM are 10 ~ 25 dB, 14 ~ 25 dB, and 16 ~ 25 dB, respectively. 10000 samples are used to form the CDF with 100 bins. Similar to [82], a total data set including 144 CDFs for 4-QAM, 16-QAM, and 64-QAM modulations for all OSNRs is collected. 36 CDFs (25%) is randomly selected and used to

train the SVM-based classifier and regressor. 5-fold cross-validation is also applied. The remaining 108 CDFs (75%) are used to conduct the evaluation. DNNs are also optimized using grid searching. Note that the OSNR estimation with DNNs is under the assumption that perfect knowledge of the modulation format is known, which is not always the case in practice.

Table 5.2 summarizes the MC results for the proposed algorithm and the DNN-based one, which obtain same performance. Note that MF stands for modulation formats here. The proposed algorithm achieves 100% accuracy classification for 4-QAM and 64-QAM, and makes 1 misclassification for 16-QAM. The average MC accuracy is 99%. Similar to simulation results, the experimental results indicate that the probability of misclassification for 16-QAM is higher than that of the other two modulation formats.

The OSNR estimation results for the three modulation formats with the proposed algorithm are shown in Fig. 5.11. The mean estimation errors for 4-QAM, 16-QAM, and 64-QAM are 0.38 dB, 0.68 dB, and 0.62 dB, respectively; and the overall mean estimation error is 0.54 dB. The DNN-based algorithm obtains a higher overall mean estimate error of 0.63 dB; more specifically, the mean estimate errors for 4-QAM, 16-QAM, and 64-QAM are 0.52 dB, 0.68 dB, and 0.75 dB, respectively.

5.3.3 Complexity

In the training stage, the complexity of SVM is $O(N_s^3 + N_s^2 \cdot N_t + N_s \cdot d \cdot N_t)$ [83], where N_s is the number of support vector, N_t the number of training samples, and d the dimension of the input data. Note that in most cases, the number of support vectors is far less than the number of samples. In the testing stage, $O(N_s \cdot d \cdot N)$ operation is required when RBF kernel is applied [83], where N is the number of testing samples. Therefore the complexity of SVM is linear with the input samples, which is similar to that of the DNN [87].

5.4 Conclusion

In this chapter, a joint MC and OSNR estimation algorithm for coherent optical receivers is proposed. The proposed algorithm relies on the CDF of the received signal's amplitude in combination with SVM-based classification and regression. Numerical simulations and experiments are carried out to evaluate its performance. Results show that good classification accuracies for three widely-used modulation formats are achieved. Moreover, a very small mean estimation error is obtained within the OSNR range of practical interest. Compared with the DNN-based algorithm, the proposed one achieves better performance. The presented algorithm can be applied in the presence of frequency offset and laser phase noise, and is compatible with existing digital coherent receivers. Therefore, it represents an advisable choice for joint MC and OSNR estimation in future optical communication systems.

Chapter 6

Carrier Phase Estimation for Coherent 16-QAM Systems

6.1 Background

The emergence of bandwidth-intensive applications has driven optical fiber communications to employ spectrally-efficient modulation formats instead of the PDM QPSK. However, these systems set stringent requirement on the performance of CPE algorithms, since the Euclidean distance between the constellation points reduces as the modulation order increases. Therefore, CPE algorithms for spectrally-efficient modulation formats that exhibit better laser phase noise tolerance and low-complexity, are essential in high-speed coherent optical transmission systems [27]. The existing CPE algorithms for spectrally-efficient modulation formats can be categorized as DA [88] and NDA [89–93]. The NDA algorithms, which have the advantages of overhead reduction and improved spectral efficiency, are of particular interest. The most prominent NDA CPE algorithms are based on the blind phase search (BPS) or the M th-power [94]. The BPS proposed in [89] demonstrates a good phase noise tolerance, but at the price of very high computational complexity. Other NDA

algorithms are based on QPSK partitioning [90, 91], which enables the application of the conventional Viterbi-Viterbi phase estimation (VVPE) after constellation partition. While this reduces the complexity, it increases the sensitivity to phase noise. Multi-stage estimation algorithms, which combine a coarse estimation stage and a fine estimation stage, provide a trade-off between complexity and phase noise tolerance [92, 94–99].

Systems employing the 16-QAM format represent a solution of interest for WDM long-haul transmission systems beyond 100 Gb/s [100–102]. On the other hand, complexity reduction on 16-QAM coherent optical systems is essential [27].

In this chapter, a low-complexity two-stage CPE algorithm is proposed for 16-QAM coherent systems. Firstly, after frequency offset compensation, symbols are partitioned and a coarse estimation is performed. After that, particular symbols are rotated properly in order to perform the second power operation, which removes the modulation phase. Simulations and optical B2B experiments are carried out. Results show that the proposed algorithm provides a comparable performance with reduced complexity when compared with the conventional fourth power-based CPE algorithm.

6.2 Proposed Algorithm

Assuming that channel equalization and frequency offset compensation are performed, the signal contaminated by both AWGN and laser phase noise can be expressed as

$$y_n = x_n e^{j\phi_n} + w_n, \quad 1 \leq n \leq N, \quad (6.1)$$

where x_n is the transmitted symbol, w_n is the AWGN, ϕ_n is the laser phase noise which is modeled as a Wiener process [27], and N is the number of observed samples. The phase difference between adjacent symbols is treated as an independent and identically distributed Gaussian random variable with zero mean and variance $\sigma_p^2 = 2\pi\delta fT$, where δf

is the combined linewidth of the transmitted laser and local oscillator, and T is the symbol duration.

6.2.1 QPSK Partition for 16-QAM

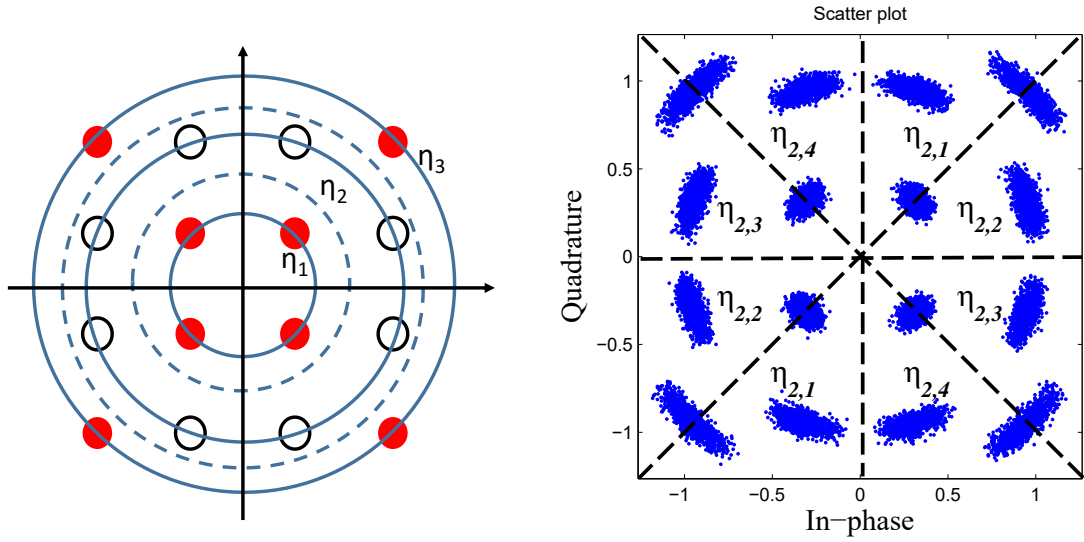
As shown in Fig. 6.1(a), the symbols for 16-QAM can be divided into three classes, based on their amplitudes. Without loss of generality, it is assumed that $E\{|x_n|^2\} = 1$, where $E\{\cdot\}$ is the expectation operator. The boundaries for the three classes are $(1 + \sqrt{2/10})/2$ and $(1 + \sqrt{18/10})/2$ (the two dash circles in Fig. 6.1(a)). The symbols of the inner circle (η_1) and those of the outer circle (η_3) are QPSK-like, and therefore, their modulation phase can be removed by the fourth power operation and their carrier phase estimated afterwards by the VVPE algorithm. However, these symbols account for 50% of the total symbols, and might not be enough to provide the phase information when the phase noise variance is large. The algorithm in [92] exploits the symbols on the middle circle (η_2) by rotating them after the fourth power operations, resulting in enhanced performance. A two-stage algorithm employing second power operation is proposed to achieve a more efficient processing.

6.2.2 Proposed Two-stage CPE Algorithm for 16-QAM

After the constellation is partitioned into three classes, the coarse estimation is achieved by using the symbols of the outer circle, since they have a relatively higher SNR than those of the inner circle. Furthermore, an average with a block of length L_1 is used to reduce the impact of the AWGN. Similar to [92], the coarse estimate ϕ_{est1} is obtained as

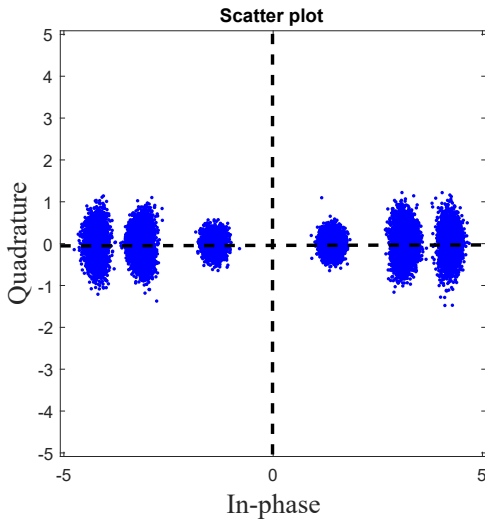
$$\phi_{est1} = \frac{1}{4} \arg \sum_{k=1}^{L_1} y_k^4, \quad y_k \in \eta_3. \quad (6.2)$$

Note that if the processed symbol does not belong to η_3 , the value of the symbol is set to zero in order to avoid the influence from the symbols of other circles [103].



(a) Constellation for 16-QAM.

(b) Constellation for 16-QAM after coarse compensation.



(c) Constellation for 16-QAM after rotations.

Fig. 6.1: Illustrative diagram for the proposed CPE algorithm.

After a coarse phase estimation and compensation, the constellation contains a residual phase noise, as shown in Fig. 6.1(b). The symbols are then properly rotated. More specifically, for η_1 and η_3 , the clusters $\eta_{1,1}$, $\eta_{3,1}$ are rotated by $-\pi/4$, while $\eta_{1,2}$, $\eta_{3,2}$ are rotated by $\pi/4$; for η_2 , the clusters $\eta_{2,1}$, $\eta_{2,2}$, $\eta_{2,3}$ and $\eta_{2,4}$ are rotated by $-\arctan 3$, $-\arctan 1/3$, $\arctan 1/3$, and $\arctan 3$, respectively. The constellation after rotation is illustrated in Fig. 6.1(c). Then, these symbols are raised to the second power for modulation phase removal. The second-stage phase estimate with a block length of L_2 is obtained as

$$\phi_{\text{est}2} = \frac{1}{2} \arg \sum_{k=1}^{L_2} y_{\text{rotated},k}^2, \quad (6.3)$$

where $y_{\text{rotated},k}$ represents the k th symbol, rotated as in Fig. 6.1(c).

The proposed algorithm is illustrated in Fig. 6.2. The phase unwrapping adopts the algorithm from [90], and it ensures that the phase estimation follows the trajectory of the physical phase. Most of the existing QPSK partition-based CPE algorithms use the fourth power operation to remove the modulation phase, and involve higher complexity than the second power operation. This is further discussed in the next sections.

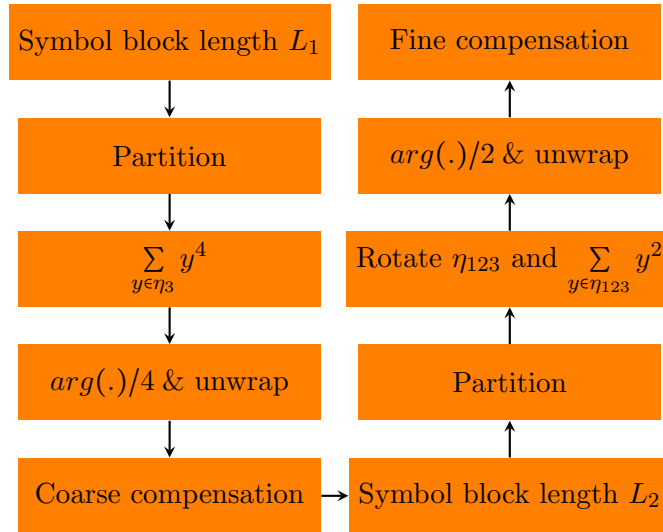


Fig. 6.2: Principle of the proposed two-stage algorithm.

6.3 Performance Evaluation

In this section, the performance of the proposed algorithm is evaluated by numerical simulations and experiments.

6.3.1 Simulation Results

In this section, the performance of the proposed ' $\eta_3^4 + \eta_{123}^2$ ' algorithm (η_3^4 represents the symbols used for coarse estimation at the first stage and η_{123}^2 represents the second power operations at the second stage) is examined through Monte Carlo simulations and compared with that of two conventional algorithms. One algorithm is the BPS [89], while the other one is proposed in [92] and referred to as ' $\eta_3^4 + \eta_{123}^4$ ' (η_{123}^4 represents the fourth power operations at the second stage). In the simulations, phase noise and AWGN are considered. The required SNR for each algorithm at a BER of 10^{-2} is shown in Fig. 6.3 versus the linewidth-symbol duration product. The number of test phases used by the BPS is 32 [89], and similar to [92], the block lengths for all algorithms are optimized. The SNR is 14.9 dB at BER = 10^{-2} when the phase noise is absent. Differential encoding is applied to deal with the cyclic slip [94].

It can be seen that with 0.5 dB SNR penalty at BER = 10^{-2} , the BPS algorithm can tolerate a linewidth-symbol duration product of 1.1×10^{-4} ; the proposed $\eta_3^4 + \eta_{123}^2$ algorithm's tolerance is 8×10^{-5} , while the $\eta_3^4 + \eta_{123}^4$ has a tolerance of 7×10^{-5} . Considering a coherent system working at 32 Gbaud/s, the equivalent linewidths for the three algorithms are 3.52 MHz, 2.56 MHz, and 2.24 MHz, respectively. The BPS algorithm requires the smallest SNR when compared with the partition-based algorithms, but is significantly more complex. The proposed algorithm shows slightly better performance than the $\eta_3^4 + \eta_{123}^4$.

Furthermore, the partition-based algorithms require a relatively large SNR when the linewidth-symbol duration product is large, compared with the BPS algorithm. The reason

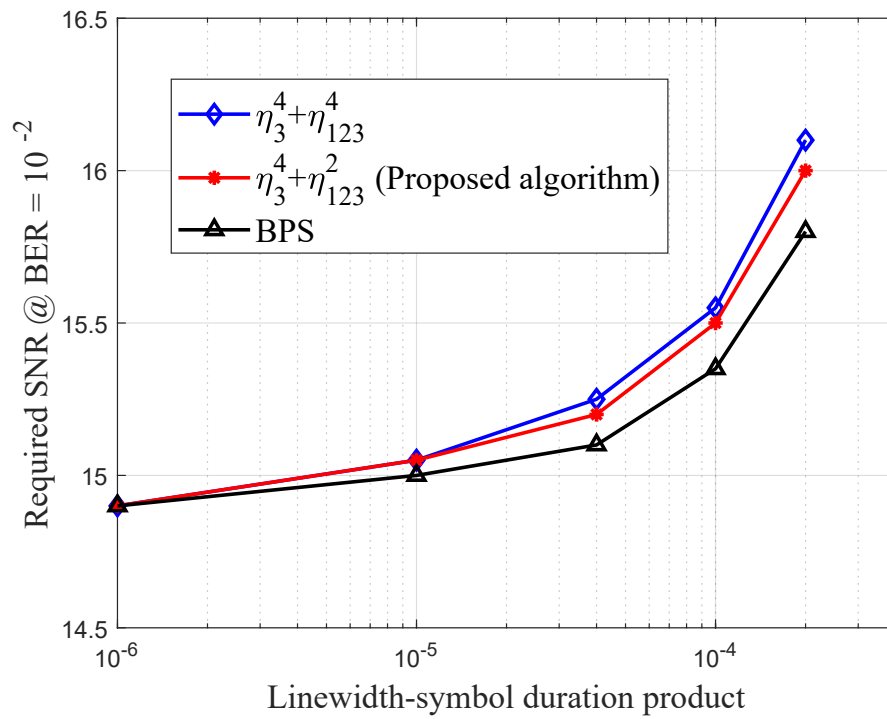


Fig. 6.3: SNR versus linewidth-symbol duration product at $\text{BER} = 10^{-2}$ for different CPE algorithms.

is that a large residual phase noise might exist when the linewidth symbol duration product is large [92]. Therefore, at the second stage, some symbols of η_{123} might rotate excessively and cross the boundary (the dashed line in Fig. 6.1(b)). For example, the symbols belonging to $\eta_{2,1}$ can cross the vertical dash line and be considered as part of $\eta_{2,4}$.

The lengths of the block for the proposed algorithm at the two different stages are also studied. In Table 6.1, the optimal lengths at the first and second stages, which minimize the BER, are given when the SNR is 16 dB. It can be seen that the block lengths are smaller for larger linewidth-symbol duration product. The reason is that, although it can reduce the impact of AWGN, a long block length results in a performance degradation of the CPE tracking.

Table 6.1: Optimal block lengths at SNR = 16 dB.

$\Delta f T_s$	2e-4	1e-4	4e-5	1e-5	1e-6
L_1	30	30	70	110	120
L_2	10	20	20	30	80
BER	9.5e-3	7.2e-3	5.2e-3	4.3e-3	3.5e-3

6.3.2 Experimental Results

Optical PDM B2B experiments are carried out to verify the system performance of the proposed CPE algorithm. The experimental setup is similar to the one in Chapter 3. In the off-line processing, the collected signal is processed by a matched filter, and then down-sampled to one sample per symbol. After the timing recovery, the constant modulus algorithm is employed to separate the two polarizations. Then, the frequency offset is compensated by using the method in [45]. Subsequently, the phase noise is estimated.

After compensating for the phase noise, the demodulation is performed and the BER is calculated.

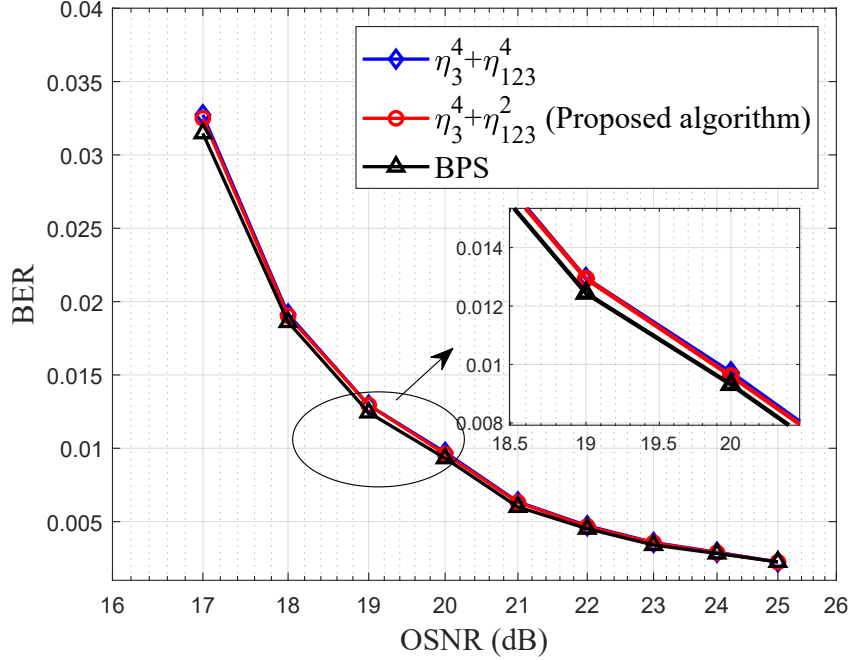


Fig. 6.4: The BER vs. OSNR for different CPE algorithms.

The experimental results for the BPS, $\eta_3^4 + \eta_{123}^4$, and the proposed $\eta_3^4 + \eta_{123}^2$ are depicted in Fig. 6.4. The results show that the BPS attains the lowest BER. The proposed algorithm exhibits approximately 0.1 dB penalty when compared with the BPS, and similar performance with the $\eta_3^4 + \eta_{123}^4$. Since the linewidth-symbol duration product in the experiments is around 1.6×10^{-5} , the differences among all those algorithms are trivial; however, this observation complies with the simulation results at the same linewidth-symbol duration product range.

6.4 Complexity Analysis

The complexities of the BPS, $\eta_3^4 + \eta_{123}^4$, and proposed $\eta_3^4 + \eta_{123}^2$ algorithms are compared in Table 6.2. The complexities are evaluated in the case of single polarization with phase unwrapping. Here, B denotes the number of trial phase, and L is the window length used by the BPS. L_1 and L_2 are the block lengths for all partition-based algorithms at the first stage and second stage, respectively. N is the number of the observed symbol. It can be observed that the BPS requires remarkably larger number of multiplications than the others. The proposed second power-based algorithm involves less multiplications than its fourth power-based counterpart. It is worth mentioning that the number of real multiplications for one fourth power operation is 8 in [90, 91], while [92] pointed out that this can be reduced to 6 by using some optimum implementation. In the comparisons here, the latter is adopted. Nonetheless, complexity reduction is achieved since one second power operation requires only 4 real multiplications.

Table 6.2: Complexity comparison for the CPE algorithms.

	$\eta_3^4 + \eta_{123}^4$	Proposed $\eta_3^4 + \eta_{123}^2$	BPS
Real multiplications	$21N + \frac{1}{2}N + (\frac{1}{L_1} + \frac{1}{L_2})N$	$19N + \frac{1}{2}N + (\frac{1}{L_1} + \frac{1}{L_2})N$	$6BN + 4N$
Real additions	$13N + \frac{1}{2}N + 3(\frac{1}{L_1} + \frac{1}{L_2})N$	$13N + \frac{1}{2}N + 3(\frac{1}{L_1} + \frac{1}{L_2})N$	$(2L + 1)BN + 6N$
Comparisons	$2N + \frac{1}{2}N + 2(\frac{1}{L_1} + \frac{1}{L_2})N$	$6N + \frac{1}{2}N + 2(\frac{1}{L_1} + \frac{1}{L_2})N$	$5BN + 2N$
Look-up table operations	$(\frac{1}{L_1} + \frac{1}{L_2})N$	$(\frac{1}{L_1} + \frac{1}{L_2})N$	0

6.5 Summary

In this chapter, a novel two-stage CPE algorithm for 16-QAM coherent optical systems is proposed. Different from the conventional fourth power-based CPE algorithms, the pro-

posed algorithm considers the second power operation to remove the modulation phase of the symbols at the second stage. Simulations and optical B2B experiments verify the performance of the proposed algorithm consistently. With a significantly reduced complexity, the proposed algorithm exhibits only approximately 0.1 dB performance penalty when compared with the BPS in the experiments. Compared with the conventional fourth power-based algorithm, the proposed algorithm provides comparable performance with reduced complexity.

Chapter 7

Flexible Transmission Scheme for Optical Metro Networks

7.1 Introduction

After dominating long-haul optical transmission networks for several years, coherent optical systems with DSP techniques are extending their domination to optical metro networks [24]. On the other hand, the optical metro networks are evolving into an open and disaggregated architecture to achieve high flexibility, interoperability, and diversity for the increasing metro applications [28]. The demand for wavelength services among businesses has been driven primarily by the rise of cloud computing. As the cloud ecosystem develops, many organizations prefer wavelength services for interconnecting their data centres to public cloud providers [104]. In this context, service providers need the metro optical networks to provide more wavelength connectivity to their customers instead of just speed. However, the existing wavelength-to-users allocation is orthogonal, and frequency resources could be soon saturated with the increasing number of users. When large number of users require service connectivities, a typical solution is to share the wavelength resources with users

and sort these users with different priorities [105]. However, for many businesses, the downtime is unacceptable and the continuous connectivity is essential for productivity. The mission-critical applications, such as high-frequency trading, can be severely affected by just a few nanoseconds of downtime. To deal with this challenge, non-orthogonal multiple access (NOMA) approach is one promising solution to support multi users' connectivity simultaneously without service interruption.

Power-domain NOMA in optical fiber communications has been investigated very recently [106] [107]. It supports multiple users with the same time and frequency resources by allocating different power levels to users based on their channel conditions. In [106], power domain NOMA is employed in optical access networks, and provides improved system performance when compared to the orthogonal frequency domain multiple access. In [107], it is shown that non-orthogonal digital domain power division multiplexing provides much higher spectral efficiency, and is compatible with current dual polarization WDM and space division multiplexing systems. However, clustering and pairing of users based on their channel conditions are needed in the presence of large number of users, and thus the system complexity increases. On the other hand, only the scenario with 2 users is investigated in [106] and [107]. Systems involving more than 2 users need to be developed.

In this chapter, a novel transmission scheme, which is based on sparse code multiple access (SCMA), for metro coherent optical systems is proposed. In the proposed scheme, digital subcarrier multiplexing (SCM) [108] is employed, and several users are served with the same subcarrier. Simulations involving 2 users, 4 users, and 6 users are conducted, and the results show that in the transmission ranges of interest for metro applications, the proposed transmission scheme attains BER lower than the FEC threshold.

7.2 Principle of Operation

7.2.1 Proposed Scheme

Without loss of generality, an SCM system with N subcarriers, which provides connectivity to J users, where $1 \leq N \leq J$, is employed. At the transmitter, the input bits, \mathbf{b}_j , from the j th user are mapped to an M point p -dimensional signal constellation. The mapping is denoted as $f_j : \mathbb{B}^{\log_2(M)} \rightarrow \mathbf{c}_j, \mathbf{c}_j \in \mathcal{C}_j$, where $\mathbb{B} = \{0, 1\}$ and \mathcal{C}_j is p -dimensional complex constellation set for the j th user. After the mapping, each p -dimensional constellation point is spread to an N -dimensional codeword by applying the spreading matrix $\mathbf{V}_j \in \mathbb{B}^{N \times p}$. The overall process from bits to codewords can be expressed as $\mathbf{x}_j = \mathbf{V}_j f_j(\mathbf{b}_j)$, $\mathbf{x}_j \in \mathcal{X}_j$, where \mathcal{X}_j represents the codebook set for the j th user. Because only p dimensions of the N -dimensional codeword are used to carry data information while the remaining $N - p$ dimensions are set to zeros, the codeword is sparse. The sparsity of the codewords is important, as it helps to reduce the interference from other users and the complexity at the detection stage. To describe the allocation of users to subcarriers, an $N \times J$ binary matrix, \mathbf{A} , is defined as the user-to-subcarrier indicator matrix. The elements in the rows of \mathbf{A} represent the users assigned to each subcarrier, while those in columns denote the subcarriers assigned to each user. Each column of \mathbf{A} , i.e. \mathbf{a}_j , is calculated by $\mathbf{a}_j = \text{diag}(\mathbf{V}_j \mathbf{V}_j^T)$, where superscript T represents transpose of the vector and/or matrix, and $\text{diag}()$ denotes the vector containing the diagonal elements of the objective matrix. The (n, j) th element of \mathbf{A} is denoted as $a_{n,j}$, and it is 1 if the j th user contributes its data to the n th subcarrier. Furthermore, $\phi_n = \{j : 1 \leq j \leq J, a_{n,j} = 1\}$ is defined to represent the index set of users contributing to the n th subcarrier. Similarly, $\psi_j = \{n : 1 \leq n \leq N, a_{n,j} = 1\}$ is defined to show the index set of subcarriers occupied by the j th user.

After upsampling and passing through a pulse shaping filter, the codewords on different

subcarriers are shifted to different center frequencies in the spectrum and multiplexed before being transmitted through the channel.

At the receiver, all subcarriers are captured simultaneously. After bulk chromatic dispersion compensation and frequency offset compensation, each subcarrier is successively shifted to the baseband and filtered out by a digital low-pass filter (LPF). Next, each subcarrier is equalized individually. Assuming that the channel impairments are compensated and the synchronizations are performed, the received signal on a symbol-by-symbol base is expressed as

$$\mathbf{y} = \sum_{j=1}^J \mathbf{x}_j + \mathbf{z}, \quad (7.1)$$

where $\mathbf{y} = [y[1], \dots, y[N]]^T$ is the received signal, \mathbf{x}_j is the N -dimensional codewords of user j , and \mathbf{z} is independent and identically distributed complex Gaussian noise with zero-mean and a covariance matrix $\sigma^2 \mathbf{I}$.

7.2.2 Codebook Design

The design of SCMA codebook has been discussed in [109] and [110]. In general, the design goal is to obtain the optimum multidimensional constellations, \mathbf{c}^\dagger and the optimum user-to-subcarrier spreading matrix, \mathbf{V}^\dagger . Accordingly, the process is formulated as

$$\mathbf{c}^\dagger, \mathbf{V}^\dagger = \arg \max_{\mathbf{c}, \mathbf{V}} d(\lambda(\mathbf{c}, \mathbf{V}; J, N, M, p)), \quad (7.2)$$

where d denotes a given design criteria and λ represents the SCMA system. In [110], a sub-optimal optimization method is introduced, which consists of two steps. To begin with, a mother constellation of size M , \mathcal{C}^+ , is designed from the Cartesian product of two p -dimensional real constellations with a desired Euclidean distance. Then, user-specific unitary rotations are performed on the mother constellation. These rotations are used to generate decodable symbols for users over the same subcarrier. Assuming that $J = 4$, $N = 2$,

and $M = 4$, based on the above procedures, the M -point p -dimensional constellation sets, \mathcal{C}_j , where $j = 1, 2, 3, 4$, are provided in (7.3) [111].

$$\mathcal{C}_1 = \{-0.1815 - 0.1318j, \quad -0.6351 - 0.4615j, \quad 0.6351 + 0.4615j, \quad 0.1815 + 0.1318j\}$$

$$\mathcal{C}_2 = \{-0.0055 - 0.2242j, \quad -0.0193 - 0.7848j, \quad 0.0193 + 0.7848j, \quad 0.0055 + 0.2242j\}$$

$$\mathcal{C}_3 = \{0.7851, \quad -0.2243, \quad 0.2243, \quad -0.7851\}$$

$$\mathcal{C}_4 = \{0.1392 - 0.1759j, \quad 0.4873 - 0.6156j, \quad -0.4873 + 0.6156j, \quad -0.1392 + 0.1759j\}. \quad (7.3)$$

In addition, the spreading matrix, \mathbf{V} , is given by

$$\mathbf{V} = \begin{bmatrix} 0 & 1 & 1 & 0 \\ 1 & 0 & 0 & 1 \end{bmatrix}. \quad (7.4)$$

Accordingly, the allocation matrix is obtained as

$$\mathbf{A} = \begin{bmatrix} 0 & 1 & 1 & 0 \\ 1 & 0 & 0 & 1 \end{bmatrix}. \quad (7.5)$$

In this example, \mathbf{V} is identical to \mathbf{A} ; however, this is not always the case, as the example involving 6 users provided in [111] illustrates. After the spreading, the codebook sets for the j th user, \mathcal{X}_j , are shown in (7.6).

$$\mathcal{X}_1 = \left\{ \begin{bmatrix} 0 \\ -0.1815 - 0.1318j \end{bmatrix}, \begin{bmatrix} 0 \\ -0.6351 - 0.4615j \end{bmatrix}, \begin{bmatrix} 0 \\ 0.6351 + 0.4615j \end{bmatrix}, \begin{bmatrix} 0 \\ 0.1815 + 0.1318j \end{bmatrix} \right\}$$

$$\mathcal{X}_2 = \left\{ \begin{bmatrix} -0.0055 - 0.2242j \\ 0 \end{bmatrix}, \begin{bmatrix} -0.0193 - 0.7848j \\ 0 \end{bmatrix}, \begin{bmatrix} 0.0193 + 0.7848j \\ 0 \end{bmatrix}, \begin{bmatrix} 0.0055 + 0.2242j \\ 0 \end{bmatrix} \right\}$$

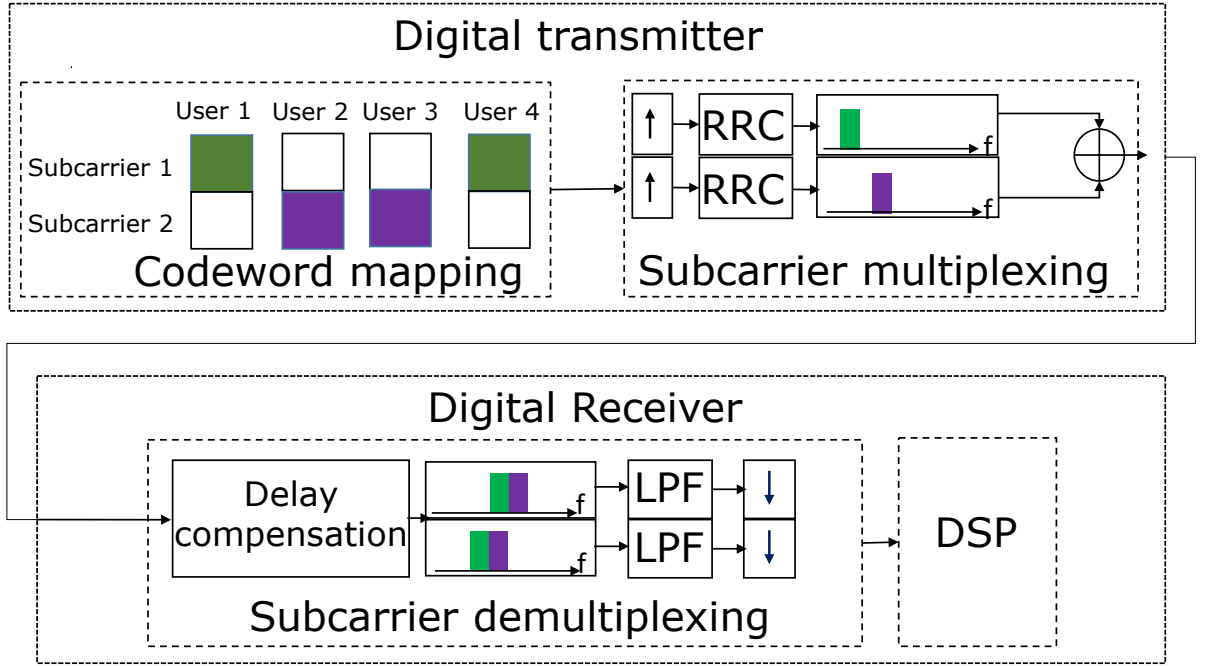


Fig. 7.1: System model for the proposed transmission scheme.

$$\mathcal{X}_3 = \left\{ \begin{bmatrix} 0.7851 \\ 0 \end{bmatrix}, \begin{bmatrix} -0.2243 \\ 0 \end{bmatrix}, \begin{bmatrix} 0.2243 \\ 0 \end{bmatrix}, \begin{bmatrix} -0.7851 \\ 0 \end{bmatrix} \right\}$$

$$\mathcal{X}_4 = \left\{ \begin{bmatrix} 0 \\ 0.1392 - 0.1759j \end{bmatrix}, \begin{bmatrix} 0 \\ 0.4873 - 0.6156j \end{bmatrix}, \begin{bmatrix} 0 \\ -0.4873 + 0.6156j \end{bmatrix}, \begin{bmatrix} 0 \\ -0.1392 + 0.1759j \end{bmatrix} \right\}. \quad (7.6)$$

7.2.3 DSP Subsystems in the Receiver

Figure 7.1 shows the system architecture for the proposed scheme, when 4 users transmit over 2 subcarriers (\uparrow and \downarrow represent upsampling and downsampling, respectively). The DSP consists of CD compensation, coarse frequency offset compensation, subcarrier demultiplexing, adaptive equalization, and phase recovery. More details can be found in [108].

However, since the constellation is non square-QAM, conventional blind algorithms such as CMA and RDE are vulnerable. A TS-least mean squares (LMS) equalizer [17, 18] is more appropriate to achieve polarization demultiplexing for non square-QAM formats.

As decision is involved and thus carrier phase recovery is required in the butterfly equalizer, a one-tap adaptive filter is added on both polarizations after the butterfly filter. For the butterfly equalizer, the output is given by

$$\begin{aligned} E_{ho}[i] &= \mathbf{w}_{hh}\mathbf{E}_{hi} + \mathbf{w}_{hv}\mathbf{E}_{vi} \\ E_{vo}[i] &= \mathbf{w}_{vh}\mathbf{E}_{hi} + \mathbf{w}_{vv}\mathbf{E}_{vi}, \end{aligned} \quad (7.7)$$

where $E_{ho}[i]$ and $E_{vo}[i]$ are the i th output of the equalizer, the suffixes h and v represent the two orthogonal polarizations; w_{hh} , w_{hv} , w_{vh} , and w_{vv} are the tap weights with length of L ; \mathbf{E}_{hi} (\mathbf{E}_{hv}) denotes a sliding block of L symbols, $\{E_{hi}[k-L+1], E_{hi}[k-L+2], \dots, E_{hi}[k]\}$, entering the equalizer. The weights are updated according to

$$\begin{aligned} w_{hh} &= w_{hh} + \gamma\epsilon_h E_{ho}^*, \\ w_{hv} &= w_{hv} + \gamma\epsilon_h E_{ho}^*, \\ w_{vh} &= w_{vh} + \gamma\epsilon_v E_{vo}^*, \\ w_{vv} &= w_{vv} + \gamma\epsilon_v E_{vo}^*, \end{aligned} \quad (7.8)$$

where γ is the step size and $*$ represents the complex conjugation operation. The error is given by

$$\begin{aligned} \epsilon_{h,v} &= \hat{y}_{h,v}|\Gamma_{h,v}|/\Gamma_{h,v} - E_{h,vo}, \\ \Gamma_{h,v} &= \Gamma y_{h,v} + \beta\xi_{h,v}E_{h,vo}^*/|E_{h,vo}|^2, \\ \xi_{h,v} &= \hat{y}_{h,v} - \Gamma y_{h,v}E_{h,vo}. \end{aligned} \quad (7.9)$$

In the above equations, $\Gamma_{h,v}$ represents the tap coefficient of the one-tap equalizer that handles phase noise [88] and is controlled by the error $\xi_{h,v}$ and step size β , $\hat{y}_{h,v}$ denotes

either the training symbols or the decided symbols. The structure of the equalizer is shown in Fig. 7.2, where Ψ represents the operation of $|\Gamma|/\Gamma$ on Γ .

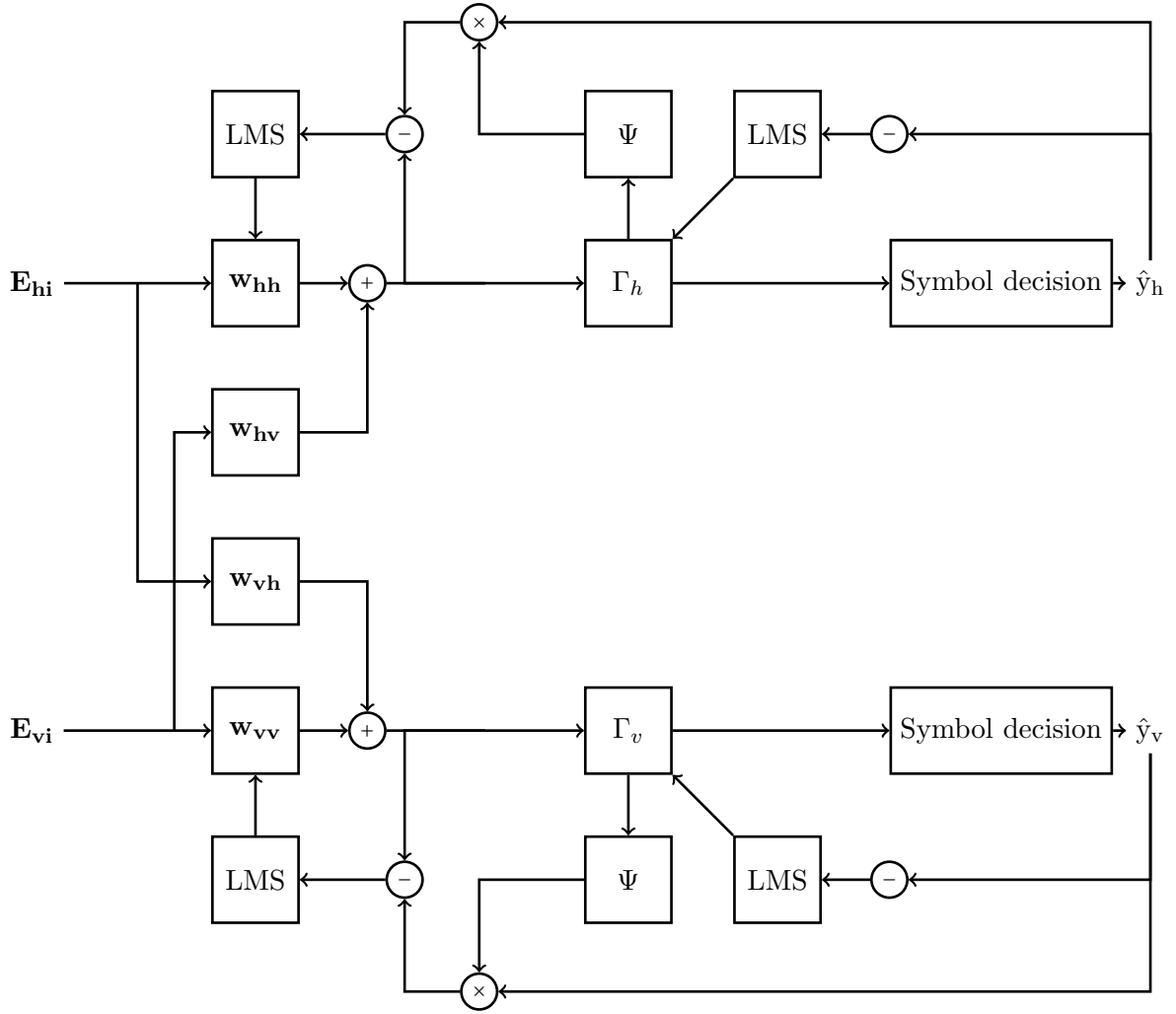


Fig. 7.2: The structure of the decision-directed adaptive equalizer.

7.2.4 MPA Detection

Given the equalized and synchronized signal on each subcarrier, the maximum *a posteriori* (MAP) detection estimates the transmitted codewords for the j th user, expressed by

$$\hat{\mathbf{x}}_j = \arg \max_{\mathbf{b} \in \mathcal{X}_j} \sum_{\mathbf{x}_j = \mathbf{b}, \mathbf{X} \in \mathcal{X}} p(\mathbf{X}|\mathbf{y}), \quad (7.10)$$

where $\mathbf{X} = \sum_{j=1}^J \mathbf{x}_j$ and $\mathcal{X} = \mathcal{X}_1 \times \mathcal{X}_2 \times \dots \times \mathcal{X}_J$.

With the assumption that the noise vector on each subcarrier is identically independently distributed and uncorrelated with the transmitted codewords, $p(\mathbf{y}|\mathbf{X})$ is factorized as

$$p(\mathbf{y}|\mathbf{X}) = \prod_{n=1}^N p(y[n]|\mathbf{X}), \quad (7.11)$$

where $p(y[n]|\mathbf{X})$ is the probability of receiving $y[n]$ on the n -th subcarrier given that the transmitted codewords are \mathbf{X} , and is given in (7.12). In practice, the knowledge of the noise variance can be obtained through parameter estimation methods or measurement from optical spectrum analyzer [112].

$$p(y[n]|\mathbf{X}) = \frac{1}{\sqrt{2\pi\sigma^2}} \exp\left(-\frac{1}{2\sigma^2} \left|y[n] - \sum_{j \in \phi_n} \mathbf{x}_j\right|^2\right). \quad (7.12)$$

By using Bayes' rule and removing all the unnecessary constant scalars, the estimate of the codeword is given by

$$\hat{\mathbf{x}}_j = \arg \max_{\mathbf{b} \in \mathcal{X}_j} \sum_{\mathbf{x}_j = \mathbf{b}, \mathbf{X} \in \mathcal{X}} p(\mathbf{X}) \prod_{n=1}^N p(y[n]|\mathbf{X}), \quad (7.13)$$

where $p(\mathbf{X}) = \prod_{j=1}^J p(\mathbf{x}_j)$.

Solving (7.13) is proportional to M^J and thus the complexity grows exponentially with the number of users. Due to the sparse feature of the proposed scheme, a message passing algorithm (MPA) [113] is employed instead, as the complexity is only proportional to the number of users colliding on each subcarrier. Figure 7.3 shows the factor graph with $N = 2$ function nodes (FNs) and $J = 4$ resource nodes (VNs); FNs and VNs represent the subcarriers and users, respectively. In MPA, the soft information of codewords are iteratively exchanged between FNs and VNs. After a given number of iterations, the log-likelihood ratio of the bit is obtained [114].

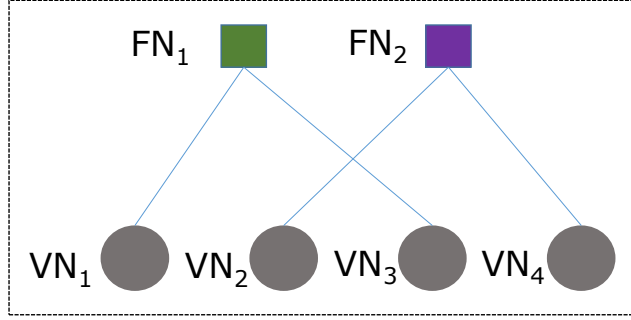


Fig. 7.3: Factor graph of MPA with 2 function nodes and 4 resources nodes.

To formulate the MPA, the message flow from the n th FN to the j th VN at the τ th iteration is denoted as $S_{f_n \rightarrow v_j}^{(\tau)}$. Similarly, the message flow from the j th VN to the n th FN at the τ th iteration is denoted as $S_{v_j \rightarrow f_n}^{(\tau)}$. Initially, all messages from VNs to FNs are assumed to be equiprobable:

$$S_{v_j \rightarrow f_n}^{(0)}(\mathbf{x}_j) = 1/M. \quad (7.14)$$

Then, the FNs update and send message to the connected VNs:

$$S_{f_n \rightarrow v_j}^{(\tau+1)}(\mathbf{x}_j) = \sum_{\mathbf{x}_1 \in \mathcal{X}_1, \forall i \in \phi_n \setminus j} p(y_n | \mathbf{X}) \times \prod_{i \in \phi_n \setminus j} S_{v_i \rightarrow f_n}^{(\tau)}(x_i). \quad (7.15)$$

The update of the n th FN is based on the extrinsic information. Taking Fig. 7.3 as an example, when FN₁ sends information to VN₁, message from VN₃ is extrinsic. Next, message passes from the j th VN to the connected n th FN:

$$S_{v_j \rightarrow f_n}^{(\tau+1)}(\mathbf{x}_j) = p(\mathbf{x}_j) \prod_{l \in \psi_j \setminus n} S_{f_l \rightarrow v_j}^{(\tau+1)}(\mathbf{x}_j). \quad (7.16)$$

After a number of iterations, τ_{max} , the output of the MPA for the j th user is given by

$$S_j(\mathbf{x}_j) = p(\mathbf{x}_j) \prod_{n \in \psi_j} S_{f_n \rightarrow v_j}^{(\tau_{max})}(\mathbf{x}_j). \quad (7.17)$$

Then, the log-likelihood-ratios (LLR) of the m th bit for the j th user is calculated by

$$LLR(b_{j,m}) = \log \frac{\sum_{\mathbf{x}_j \in \mathcal{X}_{j,m}^1} S_j(\mathbf{x}_j)}{\sum_{\mathbf{x}_j \in \mathcal{X}_{j,m}^0} S_j(\mathbf{x}_j)}, \quad (7.18)$$

where $\mathcal{X}_{j,m}^1$ represent subsets of \mathcal{X}_j for $b_{j,m} = 1$ and $\mathcal{X}_{j,m}^0$ are those for $b_{j,m} = 0$. Next, the BER is calculated from the LLR. It is also worth noting that the exponential function in MPA might require large memory; therefore, MPA in log-domain is preferred in practical implementation [115].

7.3 Performance Evaluation

The feasibility and performance of the proposed scheme is investigated by numerical simulation. Three scenarios are considered: 2 users over 1 carrier, 4 users over 2 subcarriers, and 6 users over 4 subcarriers. The sampling rate is 50 GS/s in all scenarios. Without loss of generality, the simulation setup for 2 users over 1 subcarriers is introduced. The digital transmitter and receiver are the same as in Fig. 7.1. For each user, every 2 bits are mapped into a codeword and modulated onto the subcarriers. Then, the symbols are up-sampled by a factor of 4 and digitally shaped by a raised cosine filter with a roll-off factor of 0.1. The SSMF in one span is 100 km long. For the fiber parameters, the attenuation coefficient is 0.2 dB/km, the dispersion parameter is 16 ps/nm/km, the polarization mode dispersion coefficient is 0.1 ps/ $\sqrt{\text{km}}$, and the nonlinear coefficient is 1.4 /W/km. The noise figure and the gain of the EDFA are 5 dB and 20 dB, respectively. The frequency offset and the laser linewidth is set to 200 MHz and 100 kHz, respectively. After subcarriers demultiplexing, the signal is sampled at 2 samples/symbol, and the CD is compensated in frequency domain. Then, the signal is downsampled to 1 sample/symbol and the frequency offset is compensated by applying the algorithm in [42]. After that, the signal is processed by the adaptive equalizer mentioned in Sec. 7.2.3. The transmission distances are selected based on the fact that metro networks range is less than 500 km [24] and the scale of metro networks with a range of about 100 km grows rapidly [28]. More specifically, the transmission distances are set to 400 km and 800 km for both 2 users over 1 carrier and 4 users over 2 subcarriers. In

the case of 6 users over 4 subcarriers, because the Euclidean distance between constellation points reduces considerably, 200 km transmission distance is used. The system performance is shown in Figs. 7.4-7.6 in terms of BER versus various launch powers. Figures 7.4 and 7.5 show the results for the scenarios of 2 users over 1 carrier and 4 users over 2 subcarriers, respectively. In Fig. 7.6, the results for 6 users over 4 subcarriers are shown. In this case, 3 users collide on 1 subcarrier and the interference is higher than for the two aforementioned scenarios. Note that the typical SD FEC threshold with 20% overhead is 2.4×10^{-2} , while HD FEC threshold with 7% overhead is 3.8×10^{-3} . It can be seen that in all scenarios, the obtained BER is lower than the HD FEC threshold with the optimal launch powers.

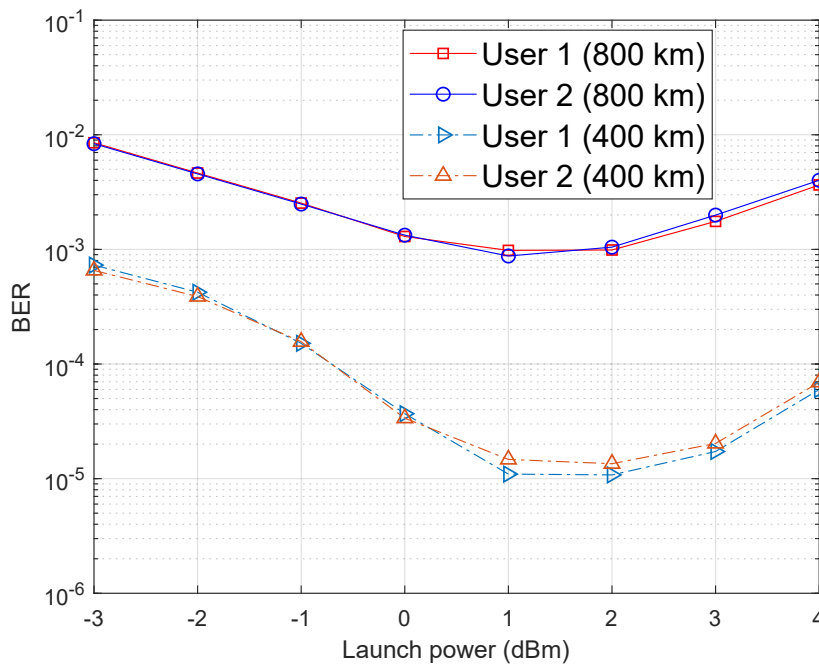


Fig. 7.4: Simulation results for 2 users.

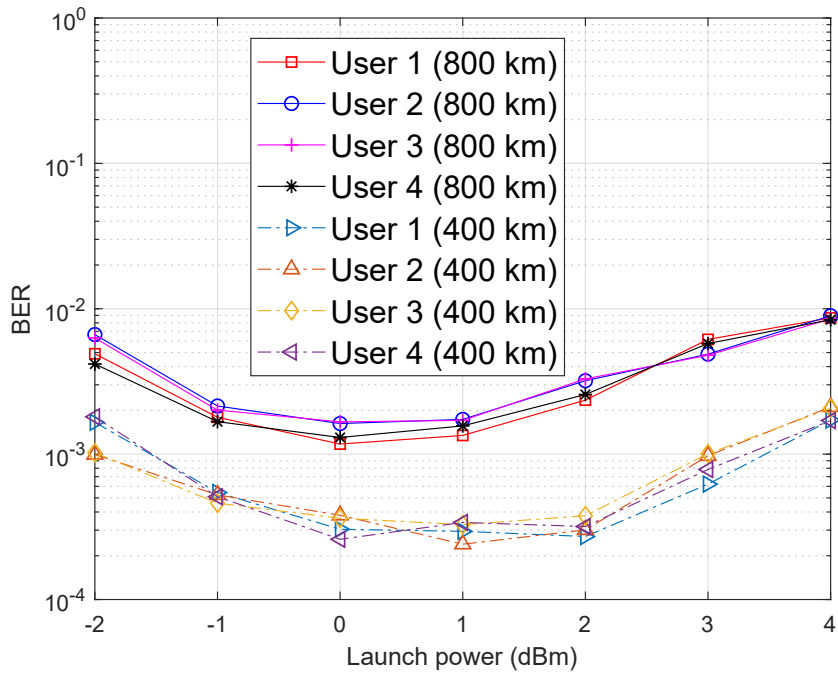


Fig. 7.5: Simulation results for 4 users.

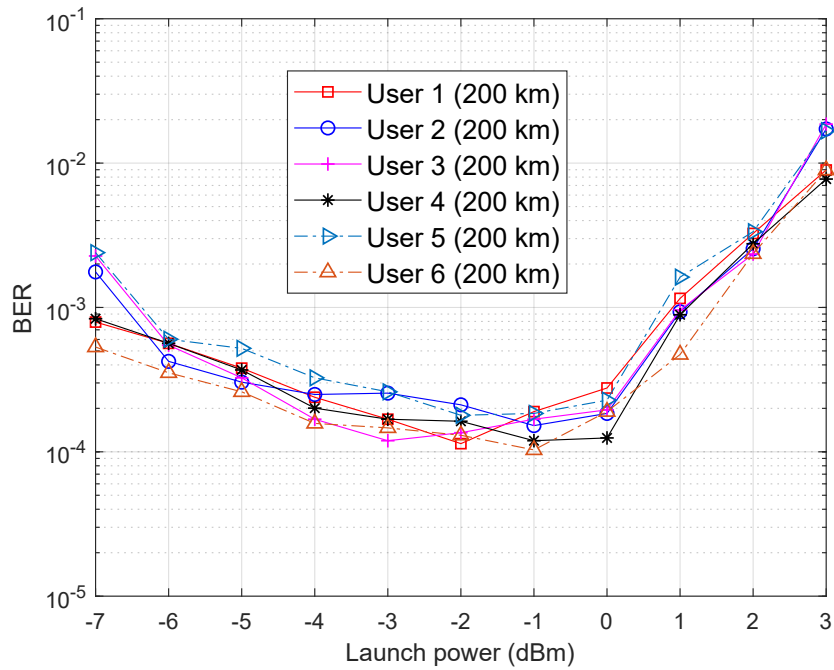


Fig. 7.6: Simulation results for 6 users.

7.4 Summary

In order to provide connectivity for more users, a novel transmission scheme for metro optical coherent systems is proposed. In this framework, the construction of SCMA codewords is first introduced. By exploring the sparse structure of the codewords, the MPA is implemented. The complexity of MPA grows exponentially only with the number of users occupying each subcarrier, which is significantly less than that of MAP. Three scenarios with different numbers of users are investigated numerically. Simulation results show that the attained BER before FEC is lower than FEC thresholds within the transmission reaches of interest. By providing simultaneous connectivity for 2 users and beyond with limited resources, the proposed scheme can improve the flexibility and interoperability for the open and disaggregated metro coherent optical systems.

Chapter 8

Conclusion

The development of communication electronics will reach a bottleneck, as Moore's Law cannot continue forever. Therefore, future optical networks will face challenges to meet the IP traffic demands by only relying on high symbol rate devices. In addition, static system configuration in legacy WDM systems are becoming barrier for efficiency improvement on the network resources utilization. In response to this problem, next generation optical fiber networks are expected to be flexible and adaptive. In such flexible networks, transmission parameters are not longer predefined, but adaptive based on the existing demands and channel conditions. For example, 1 Tb/s and beyond transmission can be realized by flexible grid Nyquist superchannel with flexible modulation format, according to the scenarios. This flexibility of the network requires performance monitoring to help perceive transmission parameters such as modulation format and OSNR. Persistent and continuous self-observation is essential for the networks to operate in an efficient way. The advent of coherent detection with DSP has dramatically boosted the networks throughput, and paves the way for networks to achieve flexibility by DSP approaches. In addition, coherent optical systems have been widely employed in long-haul networks, and are swinging their impact to metro networks even access networks; hence, it is important to investigate and develop

advanced DSP techniques to for next-generation flexible optical networks.

8.1 Summary

This thesis studies advanced DSP techniques for flexible optical networks. Parameter estimation for performance monitoring has been investigated. These parameters include the modulation format, OSNR, and carrier phase noise. Additionally, a novel flexible transmission scheme for coherent optical systems has been explored.

1. In Chapter 3, an MC algorithm based on the CDF of the received signal's normalized amplitude has been proposed for coherent optical receivers. The proposed algorithm requires a fairly small number of samples and can be performed in the presence of frequency offset and phase noise.
2. In Chapter 4, an OSNR estimation algorithm has been introduced, which can be efficiently implemented with significantly-reduced complexity. Furthermore, it shows improved performance over the conventional M2M4 estimator.
3. In Chapter 5, a joint MC and OSNR estimation algorithm has been developed by applying SVM. Results show a good classification accuracy for three widely-used modulation formats. Moreover, a very small mean estimation error is obtained within the OSNR range of practical interest.
4. In Chapter 6, CPE for coherent optical systems employing 16-QAM has been investigated. The proposed algorithm considers the second power operation to remove the modulation phase of the symbols at the second stage, and it provides slightly better performance with reduced complexity when compared with the conventional fourth power-based algorithm.

5. In Chapter 7, a novel transmission scheme for optical metro network has been proposed. Three scenarios with different numbers of users are investigated. Simulation results show that the proposed scheme attains BER lower than the FEC thresholds within the transmission reaches of interest. By providing simultaneous connectivity for multiple users with limited resources, the proposed scheme can improve the flexibility and interoperability for the open and disaggregated metro coherent optical systems.

8.2 Future Directions of Research

8.2.1 Effective SNR Estimation

In the absence of fiber nonlinearity, the transmission performance is largely determined by the OSNR since almost all linear impairments can be compensated well. However, OSNR does not provide any insight into the impact from other sources such as fiber nonlinearity. Knowledge of the probability distribution of noise sources is important for characterizing the system performance. Recently, several works have reported progress on estimating the effective SNR, considering individual impacts from both ASE noise and nonlinear noise [58, 116, 117]. More specifically, employing the amplitude correlation among neighbouring symbols, the nonlinear noise variance can be estimated [58]. Further, ML-based methods such as artificial neural networks are employed to calculate the nonlinear noise variance [116, 117]. The effective SNR can be calculated after equalization and carrier phase recovery in the DSP. It reflects the overall signal quality, considering the impact from different sources such as ASE noise, nonlinear noise, and even DSP itself. In such a case, some interesting potential topics can be explored:

1. The approach proposed in [58] requires a calibration process to connect the ampli-

tude correlation with the true nonlinear noise variance for each individual system configuration, which is impractical for real implementation. On the other hand, the ML-based techniques in [116,117] employed the amplitude correlation and phase correlation among symbols as features. Are there any other features that can be employed to represent the impact of fiber nonlinearity? If so, it is expected that a better performance or reduced complexity can be achieved based on these features.

2. The above-mentioned works only consider four-wave mixing (FWM) among signals in the WDM system, and do not account for the FWM between the signal and the co-propagating noise. Evaluating the impact of the signal-noise interaction will be helpful to quantify the system performance degradation in various system configurations (e.g., different symbol rates, number of spans, and amplification schemes).

8.2.2 SCMA Codebook Design

A novel transmission scheme based on SCMA for metro optical coherent systems is proposed in Chapter 7. In this framework, the codebooks are designed for AWGN channel. For better results, the codebooks suitable for optical fiber channel with nonlinearity considered are worthy to be investigated.

Appendix

Partial Differentials of Marcum's Q Function

Here, information for obtaining (4.8) is provided. A Marcum Q function is defined as

$$Q(a, b) = \int_b^\infty \exp\left\{-\frac{a^2 + b^2}{2}\right\} x I_0(ax) dx. \quad (\text{A.1})$$

The partial derivative of $Q(a, b)$ with respect to b is given by integrating the $Q(a, b)$ at b :

$$\frac{\partial Q(a, b)}{\partial b} = -b I_0(ab) \exp\left\{-\frac{a^2 + b^2}{2}\right\}. \quad (\text{A.2})$$

By using the identity

$$Q(a, b) = 1 + \exp\left\{-\frac{a^2 + b^2}{2}\right\} I_0(ab) - Q(b, a), \quad (\text{A.3})$$

the partial derivative of $Q(a, b)$ with respect to a is found to be

$$\frac{\partial Q(a, b)}{\partial a} = b I_1(ab) \exp\left\{-\frac{a^2 + b^2}{2}\right\}. \quad (\text{A.4})$$

Fisher Information Derivation

Here, the details on obtaining (4.18) are provided. For simplification, F is used instead of F_k in the appendix. The derivative for the first term of (4.17) with respect to σ is given by

$$\begin{aligned}
& \frac{\partial(-\frac{1}{2}\ln\frac{F(1-F)}{N})}{\partial\sigma} \\
&= \frac{\partial(-\frac{1}{2}\ln F(1-F))}{\partial\sigma} \\
&= -\frac{1}{2}\frac{\partial\ln F}{\partial\sigma} - \frac{1}{2}\frac{\partial\ln(1-F)}{\partial\sigma} \\
&= -\frac{F'}{2}\frac{1}{F} + \frac{F'}{2}\frac{1}{1-F} \\
&= \frac{F'(2F-1)}{2F(1-F)}. \tag{A.5}
\end{aligned}$$

Similarly, the derivative for the second term of (4.17) with respect to σ is given by

$$\begin{aligned}
& \frac{\partial(-\frac{N(F_E-F)^2}{2F(1-F)})}{\partial\sigma} \\
&= \frac{N}{2}\frac{\partial\frac{(F_E-F)^2}{F(F-1)}}{\partial\sigma} \\
&= \frac{N}{2}\frac{\partial\left(\frac{F}{F-1} - \frac{2F_E}{F-1} - \frac{F_E^2}{F} + \frac{F_E^2}{F-1}\right)}{\partial\sigma} \\
&= \frac{N}{2}\frac{\partial\left(1 + \frac{1-2F_E+F_E^2}{F-1} - \frac{F_E^2}{F}\right)}{\partial\sigma} \\
&= \frac{N}{2}\left(\frac{1-2F_E+F_E^2}{(F-1)^2}(-F') - \frac{F_E^2}{F^2}(-F')\right) \\
&= \frac{-NF'}{2}\left(\frac{1-2F_E+F_E^2}{(F-1)^2} - \frac{F_E^2}{F^2}\right). \tag{A.6}
\end{aligned}$$

Then, the sum of the above two terms is

$$\begin{aligned}
& \frac{F'(2F-1)}{2F(1-F)} + \frac{-NF'}{2} \left(\frac{1-2F_E+F_E^2}{(F-1)^2} - \frac{F_E^2}{F^2} \right) \\
&= \frac{F'}{2} \left(\frac{(2F-1)}{F(1-F)} - N \left(\frac{1-2F_E+F_E^2}{(F-1)^2} - \frac{F_E^2}{F^2} \right) \right) \\
&= \frac{F'}{2} \left(\frac{(2F-1)F(1-F) - N(1-2F_E+F_E^2)F^2 + N(1-F)^2F_E^2}{F^2(1-F)^2} \right) \\
&= \frac{F'}{2} \left(\frac{-2F^3+3F^2-F-N(1-2F_E+F_E^2)F^2 + N(1-F)^2F_E^2}{F^2(1-F)^2} \right) \\
&= \frac{F'}{2} \left(\frac{(N-2NF)F_E^2 + 2NF^2F_E - 2F^3 + 3F^2 - F - NF^2}{F^2(1-F)^2} \right). \tag{A.7}
\end{aligned}$$

Next, the expectation of the power of the sum is given by

$$\mathbb{E} \left\{ \left(\frac{F'}{2} \right)^2 \left(\frac{(2NF-N)F_E^2 + 2NF^2F_E - 2F^3 + 3F^2 - F - NF^2}{F^2(1-F)^2} \right)^2 \right\}. \tag{A.8}$$

The following variables are defined: $a = N - 2NF$, $b = 2NF^2$, $c = -2F^3 + 3F^2 - F - NF^2$, and $d = F^2(1-F)^2$. Thus, (A.8) is expressed as

$$\begin{aligned}
& \mathbb{E} \left\{ \left(\frac{F'}{2} \right)^2 \left(\frac{aF_E^2 + bF_E + c}{d} \right)^2 \right\} \\
&= \mathbb{E} \left\{ \left(\frac{F'}{2} \right)^2 \left(\frac{a^2F_E^4 + b^2F_E^2 + c^2 + 2abF_E^3 + 2acF_E^2 + 2bcF_E}{d^2} \right) \right\} \\
&= \left(\frac{F'}{2d} \right)^2 \mathbb{E} \{ a^2F_E^4 + 2abF_E^3 + (b^2 + 2ac)F_E^2 + 2bcF_E + c^2 \} \\
&= \left(\frac{F'}{2d} \right)^2 \mathbb{E} \{ a^2(F + \delta)^4 + 2ab(F + \delta)^3 + (b^2 + 2ac)(F + \delta)^2 + 2bc(F + \delta) + c^2 \} \\
&= \left(\frac{F'}{2d} \right)^2 \mathbb{E} \{ a^2(F^4 + 4F^3\delta + 6F^2\delta^2 + 4F\delta^3 + \delta^4) + \\
& \quad 2ab(F^3 + 3F^2\delta + 3F\delta^2 + \delta^3) + (b^2 + 2ac)(F^2 + 2F\delta + \delta^2) + 2bc(F + \delta) + c^2 \} \\
&= \left(\frac{F'}{2d} \right)^2 \mathbb{E} \{ a^2\delta^4 + (4Fa^2 + 2ab)\delta^3 + (6F^2a^2 + 6Fab + b^2 + 2ac)\delta^2 \\
& \quad + (4F^3a^2 + 6F^2ab + 2Fb^2 + 4Fac + 2bc)\delta + F^4a^2 + 2F^3ab + F^2b^2 + 2F^2ac + 2Fbc + c^2 \}, \tag{A.9}
\end{aligned}$$

where $E\{\delta^4\} = 3\frac{F^2(1-F)^2}{N^2}$, $E\{\delta^3\} = 0$, $E\{\delta^2\} = \frac{F(1-F)}{N}$, $E\{\delta\} = 0$. Finally, the simplified expression is obtained as

$$\begin{aligned}
& E\left\{\left(\frac{F'}{2}\right)^2 \left(\frac{aF_E^2 + bF_E + c}{d}\right)^2\right\} \\
&= \left(\frac{F'}{2d}\right)^2 \left\{ 3a^2 \frac{F^2(1-F)^2}{N^2} + (6F^2a^2 + 6Fab + b^2 + 2ac) \frac{F(1-F)}{N} \right. \\
&\quad \left. + F^4a^2 + 2F^3ab + F^2b^2 + 2F^2ac + 2Fbc + c^2 \right\} \\
&= \frac{NF'^2}{F(1-F)}. \tag{A.10}
\end{aligned}$$

Bibliography

- [1] Cisco Visual Networking Index. “The zettabyte era: Trends and analysis,” *Cisco White Paper*, 2017.
- [2] KC Kao and George A Hockham. Dielectric-fibre surface waveguides for optical frequencies. In *Proc. Inst. Elect. Eng.*, volume 113, pages 1151–1158, Jun. 1966.
- [3] R Berry *et al.* Optical fiber system trials at 8 Mbits/s and 140 Mbits/s. *IEEE Trans. Commun.*, 26(7):1020–1027, Jul. 1978.
- [4] Robert J Mears *et al.* Low-noise erbium-doped fibre amplifier operating at 1.54 μm . *Electron. Lett.*, 23(19):1026–1028, Sep. 1987.
- [5] RW Tkach *et al.* Transmission of eight 20-Gb/s channels over 232 km of conventional single-mode fiber. *IEEE Photon. Technol. Lett.*, 7(11):1369–1371, Nov. 1995.
- [6] Barrie P Keyworth. ROADM subsystems and technologies. In *Proc. Opt. Fiber Commun. Conf.*, Mar. 2005, paper OWB5.
- [7] Thomas A Strasser *et al.* Wavelength-selective switches for ROADM applications. *IEEE J. Sel. Top. Quant. Electron.*, 16(5):1150–1157, Sep. 2010.
- [8] Peter J Winzer *et al.* Fiber-optic transmission and networking: the previous 20 and the next 20 years. *Opt. Express*, 26(18):24190–24239, Aug. 2018.

- [9] Seb J Savory. Digital coherent optical receivers: Algorithms and subsystems. *IEEE J. Sel. Top. Quantum Electron.*, 16(5):1164–1179, May 2010.
- [10] Michael G Taylor. Coherent detection method using DSP for demodulation of signal and subsequent equalization of propagation impairments. *IEEE Photon. Technol. Lett.*, 16(2):674–676, Feb. 2004.
- [11] Dany-Sebastien Ly-Gagnon *et al.* Coherent detection of optical quadrature phase-shift keying signals with carrier phase estimation. *J. Lightw. Technol.*, 24(1):12, Jan. 2006.
- [12] Han Sun *et al.* Real-time measurements of a 40 Gb/s coherent system. *Opt. Express*, 16(2):873–879, Nov. 2008.
- [13] Vittorio Curri *et al.* Dispersion compensation and mitigation of nonlinear effects in 111-Gb/s WDM coherent PM-QPSK systems. *IEEE Photon. Technol. Lett.*, 20(17):1473–1475, Sep. 2008.
- [14] Giancarlo Gavioli *et al.* NRZ-PM-QPSK 16×100 Gb/s Transmission Over Installed Fiber With Different Dispersion Maps. *IEEE Photon. Technol. Lett.*, 22(6):371–373, Feb. 2010.
- [15] Yi-Hsiang Wang and Ilya Lyubomirsky. Impact of DP-QPSK pulse shape in nonlinear 100 G transmission. *J. Lightw. Technol.*, 28(18):2750–2756, Sep. 2010.
- [16] Peter J Winzer. High-spectral-efficiency optical modulation formats. *J. Lightw. Technol.*, 30(24):3824–3835, Dec. 2012.
- [17] Deyuan Chang *et al.* Robust faster-than-Nyquist PDM-mQAM systems with Tomlinson-Harashima precoding. *IEEE Photon. Technol. Lett.*, 28(19):2106–2109, Oct. 2016.

- [18] S Zhang *et al.* Training symbol-based equalization for quadrature duobinary PDM-FTN systems. *IEEE Photon. Technol. Lett.*, 29(5):454–457, Mar. 2017.
- [19] Chunpo Pan and Frank R Kschischang. Probabilistic 16-QAM shaping in WDM systems. *J. Lightw. Technol.*, 34(18):4285–4292, Sep. 2016.
- [20] Tobias Fehenberger *et al.* On probabilistic shaping of quadrature amplitude modulation for the nonlinear fiber channel. *J. Lightw. Technol.*, 34(21):5063–5073, Nov. 2016.
- [21] J-X Cai *et al.* 70.4 Tb/s capacity over 7,600 km in C+ L band using coded modulation with hybrid constellation shaping and nonlinearity compensation. In *Proc. Opt. Fiber Commun. Conf.* OSA, 2017, paper Th5B.2.
- [22] Junho Cho *et al.* Trans-atlantic field trial using high spectral efficiency probabilistically shaped 64-QAM and single-carrier real-time 250-Gb/s 16-QAM. *J. Lightw. Technol.*, 36(1):103–113, Jan. 2018.
- [23] Junho Cho *et al.* On line rates, information rates, and spectral efficiencies in probabilistically shaped QAM systems. *Opt. Express*, 26(8):9784–9791, Apr. 2018.
- [24] David V Plant *et al.* Optical communication systems for datacenter networks. In *Proc. Opt. Fiber Commun. Conf.*, Mar. 2017, paper W3B.1.
- [25] Ori Gerstel *et al.* Elastic optical networking: A new dawn for the optical layer? *IEEE Commun. Mag.*, 50(2):s12–s20, Feb. 2012.
- [26] Zhenhua Dong *et al.* Optical performance monitoring: A review of current and future technologies. *J. Lightw. Technol.*, 34(2):525–543, Jan. 2016.
- [27] Md Saifuddin Faruk *et al.* Digital signal processing for coherent transceivers employing multilevel formats. *J. Lightw. Technol.*, 35(5):1125–1141, Mar. 2017.

- [28] Heidi Adams. “Trends in Metro Optical Networks,” Mar. 2018.
- [29] Kazuro Kikuchi. Fundamentals of coherent optical fiber communications. *J. Lightw. Technol.*, 34(1):157–179, Aug. 2015.
- [30] A Davis *et al.* Phase diversity techniques for coherent optical receivers. *J. Lightw. Technol.*, 5(4):561–572, Apr. 1987.
- [31] Irshaad Fatadin *et al.* Compensation of quadrature imbalance in an optical QPSK coherent receiver. *IEEE Photon. Technol. Lett.*, 20(20):1733–1735, Oct. 2008.
- [32] Govind P Agrawal. *Lightwave technology: Telecommunication systems*. New York: John Wiley & Sons, 2005.
- [33] Seb J Savory. Digital filters for coherent optical receivers. *Opt. Express*, 16(2):804–817, Jan. 2008.
- [34] Seb J Savory *et al.* Electronic compensation of chromatic dispersion using a digital coherent receiver. *Opt. Express*, 15(5):2120–2126, Mar. 2007.
- [35] Maxim Kuschnerov *et al.* DSP for coherent single-carrier receivers. *J. Lightw. Technol.*, 27(16):3614–3622, Jun. 2009.
- [36] Amir Eghbali *et al.* Optimal least-squares FIR digital filters for compensation of chromatic dispersion in digital coherent optical receivers. *J. Lightw. Technol.*, 32(8):1449–1456, Apr. 2014.
- [37] Gilad Goldfarb *et al.* Chromatic dispersion compensation using digital IIR filtering with coherent detection. *IEEE Photon. Technol. Lett.*, 19(13):969–971, Jun. 2007.
- [38] Ezra Ip *et al.* Coherent detection in optical fiber systems. *Opt. Express*, 16(2):753–791, Jan. 2008.

- [39] Floyd Gardner. A BPSK/QPSK timing-error detector for sampled receivers. *IEEE Trans. Commun.*, 34(5):423–429, May 1986.
- [40] Xian Zhou *et al.* All-digital timing recovery and adaptive equalization for 112 Gbit/s POLMUX-NRZ-DQPSK optical coherent receivers. *J. Opt. Commun. Netw.*, 2(11):984–990, Nov. 2010.
- [41] Peter Winzer *et al.* Spectrally efficient long-haul optical networking using 112-Gb/s polarization-multiplexed 16-QAM. *J. Lightw. Technol.*, 28(4):547–556, Sep. 2009.
- [42] Shu Zhang *et al.* Training-Aided Joint Frame and Frequency Synchronization for THP FTN Coherent Optical Systems. In *Proc. IEEE Int. Conf. Transparent Opt. Netw.*, pages 1–4, Bucharest, Romania, Jul. 2018.
- [43] Irshaad Fatadin and Seb J Savory. Compensation of frequency offset for 16-QAM optical coherent systems using QPSK partitioning. *IEEE Photon. Technol. Lett.*, 23(17):1246–1248, Sep. 2011.
- [44] Jilong Han *et al.* Frequency offset estimation with multi-steps interpolation for coherent optical systems. *IEEE Photon. Technol. Lett.*, 27(19):2011–2014, Oct. 2015.
- [45] Mehrez Selmi *et al.* Accurate digital frequency offset estimator for coherent polmux QAM transmission systems. In *Proc. Eur. Conf. Opt. Commun.*, Sep. 2009.
- [46] Tao Yang *et al.* Hardware-Efficient Multi-Format Frequency Offset Estimation for M-QAM Coherent Optical Receivers. *IEEE Photon. Technol. Lett.*, 30(18):1605–1608, Sep. 2018.
- [47] Abdelkerim Amari *et al.* A machine learning-based detection technique for optical fiber nonlinearity mitigation. *IEEE Photon. Technol. Lett.*, 31(8):627–630, Mar. 2019.

- [48] Octavia A. Dobre. Signal identification for emerging intelligent radios: Classical problems and new challenges. *IEEE Instrum. Meas. Mag.*, 18(2):11–18, Apr. 2015.
- [49] Octavia A Dobre *et al.* Survey of automatic modulation classification techniques: classical approaches and new trends. *IET Commun.*, 1(2):137–156, Apr. 2007.
- [50] Octavia A Dobre *et al.* Blind modulation classification: a concept whose time has come. In *Proc. IEEE SARNOFF Symp.*, pages 223–228, Apr. 2005.
- [51] Faisal Nadeem Khan *et al.* Modulation format identification in coherent receivers using deep machine learning. *IEEE Photon. Technol. Lett.*, 28(17):1886–1889, Sep. 2016.
- [52] Robert Borkowski *et al.* Stokes space-based optical modulation format recognition for digital coherent receivers. *IEEE Photon. Technol. Lett.*, 25(21):2129–2132, Nov. 2013.
- [53] Tianwai Bo *et al.* Modulation format recognition for optical signals using connected component analysis. *IEEE Photon. Technol. Lett.*, 29(1):11–14, Jan. 2017.
- [54] Xiaofeng Mai *et al.* Stokes space modulation format classification based on non-iterative clustering algorithm for coherent optical receivers. *Opt. Express*, 25(3):2038–2050, Feb. 2017.
- [55] Syed Muhammad Bilal *et al.* Blind modulation format identification for digital coherent receivers. *Opt. Express*, 23(20):26769–26778, Oct. 2015.
- [56] Jie Liu *et al.* Modulation format identification based on received signal power distributions for digital coherent receivers. In *Proc. Opt. Fiber Commun. Conf.*, Mar. 2014, paper Th2A.29.

- [57] David J Ives *et al.* Estimating OSNR of equalised QPSK signals. *Opt. Express*, 19(26):B661–B666, Dec. 2011.
- [58] Zhenhua Dong *et al.* OSNR monitoring for QPSK and 16-QAM systems in presence of fiber nonlinearities for digital coherent receivers. *Opt. Express*, 20(17):19520–19534, Aug. 2012.
- [59] Qiong Wu *et al.* Training symbol assisted in-band OSNR monitoring technique for PDM-CO-OFDM system. *J. Lightw. Technol.*, 35(9):1551–1556, May 2017.
- [60] Wanli Wang *et al.* Joint OSNR and interchannel nonlinearity estimation method based on fractional fourier transform. *J. Lightw. Technol.*, 35(20):4497–4506, Oct. 2017.
- [61] C Do *et al.* Data-aided OSNR estimation for QPSK and 16-QAM coherent optical system. *IEEE Photon. J.*, 5(5):6601609–6601609, Sep. 2013.
- [62] Danshi Wang *et al.* Modulation format recognition and OSNR estimation using CNN-based deep learning. *IEEE Photon. Technol. Lett.*, 29(19):1667–1670, Oct. 2017.
- [63] Xiang Lin *et al.* Joint modulation classification and OSNR estimation enabled by support vector machine. *IEEE Photon. Technol. Lett.*, 30(24):2127–2130, Oct. 2018.
- [64] Chen Zhu *et al.* Statistical moments-based OSNR monitoring for coherent optical systems. *Opt. Express*, 20(16):17711–17721, Jul. 2012.
- [65] Md Saifuddin Faruk *et al.* In-band estimation of optical signal-to-noise ratio from equalized signals in digital coherent receivers. *IEEE Photon. J.*, 6(1):1–9, Feb. 2014.
- [66] Md Saifuddin Faruk *et al.* Estimation of OSNR for Nyquist-WDM transmission systems using statistical moments of equalized signals in digital coherent receivers. In *Proc. Opt. Fiber Commun. Conf.*, Mar. 2014, paper Th2A.29.

- [67] Xiang Lin *et al.* OSNR estimation algorithm for higher-order modulation formats in coherent optical systems. In *Proc. Asia Commun. and Photon. Conf.*, Nov. 2017, paper Su2A.26.
- [68] HG Choi *et al.* Nonlinearity-tolerant OSNR estimation technique for coherent optical systems. In *Proc. Opt. Fiber Commun. Conf.*, Mar. 2015, paper W4D.2.
- [69] Marcos Álvarez-Díaz *et al.* SNR estimation for multilevel constellations using higher-order moments. *IEEE Trans. Sig. Process.*, 58(3):1515–1526, Mar. 2010.
- [70] Xiang Lin *et al.* Modulation classification using received signal’s amplitude distribution for coherent receivers. *IEEE Photon. Technol. Lett.*, 29(21):1872–1875, Nov. 2017.
- [71] Fanggang Wang *et al.* Fast and robust modulation classification via Kolmogorov-Smirnov test. *IEEE Trans. Commun.*, 58(8):2324–2332, Aug. 2010.
- [72] Andrzej P Ruszczyński and Andrzej Ruszczyński. *Nonlinear Optimization*. New Jersey, USA: Princeton University Press, 2006.
- [73] Mohamed Sahnoudi and Moeness G Amin. Fast iterative maximum-likelihood algorithm (FIMLA) for multipath mitigation in the next generation of GNSS receivers. *IEEE Trans. Wireless Commun.*, 7(11):4362–4374, Dec. 2008.
- [74] Zijun Gong *et al.* Design, analysis, and field testing of an innovative drone-assisted zero-configuration localization framework for wireless sensor networks. *IEEE Trans. Veh. Technol.*, 66(11):10322–10335, Jul. 2017.
- [75] WK Pratt. Partial differentials of Marcum’s Q function. *Proc. IEEE*, 56(7):1220–1221, Jul. 1968.

- [76] Aad W Van der Vaart. *Asymptotic Statistics*. Cambridge, UK: Cambridge University Press, 2000.
- [77] Steven M Kay. *Fundamentals of Statistical Signal Processing: Estimation Theory*. New Jersey, USA: Prentice Hall PTR, 1993.
- [78] Pierluigi Poggiolini. The GN model of non-linear propagation in uncompensated coherent optical systems. *J. Lightw. Technol.*, 30(24):3857–3879, Dec. 2012.
- [79] Mark Horowitz. Computing’s energy problem (and what we can do about it). In *Proc. IEEE International Solid-State Circuits Conference (ISSCC)*, pages 10–14, Feb. 2014.
- [80] Faisal Nadeem Khan *et al.* Experimental demonstration of joint OSNR monitoring and modulation format identification using asynchronous single channel sampling. *Opt. Express*, 23(23):30337–30346, Nov. 2015.
- [81] Jakob Thrane *et al.* Machine learning techniques for optical performance monitoring from directly detected PDM-QAM signals. *J. Lightw. Technol.*, 35(4):868–875, Feb. 2017.
- [82] Faisal Nadeem Khan *et al.* Joint OSNR monitoring and modulation format identification in digital coherent receivers using deep neural networks. *Opt. Express*, 25(15):17767–17776, Jul. 2017.
- [83] Christopher JC Burges. A tutorial on support vector machines for pattern recognition. *Data Mining and Knowledge Discovery*, 2(2):121–167, Jun. 1998.
- [84] Tu Nguyen *et al.* Fiber nonlinearity equalizer based on support vector classification for coherent optical OFDM. *IEEE Photon. J.*, 8(2):1–9, Apr. 2016.
- [85] Chih-Chung Chang and Chih-Jen Lin. Libsvm: a library for support vector machines. *ACM Trans. Intell. Syst. Technol.*, 2(3):1–27, Apr. 2011.

- [86] Gareth James *et al.* *An Introduction to Statistical Learning*. Springer, 2013.
- [87] Ian Goodfellow *et al.* *Deep Learning*. MIT Press Cambridge, 2016.
- [88] Yojiro Mori *et al.* Novel configuration of finite-impulse-response filters tolerant to carrier-phase fluctuations in digital coherent optical receivers for higher-order quadrature amplitude modulation signals. *Opt. Express*, 20(24):26236–26251, Nov. 2012.
- [89] Timo Pfau *et al.* Hardware-efficient coherent digital receiver concept with feedforward carrier recovery for M -QAM constellations. *J. Lightw. Technol.*, 27(8):989–999, Apr. 2009.
- [90] Irshaad Fatadin *et al.* Laser linewidth tolerance for 16-QAM coherent optical systems using QPSK partitioning. *IEEE Photon. Technol. Lett.*, 22(9):631–633, May 2010.
- [91] Yuliang Gao *et al.* Low-complexity and phase noise tolerant carrier phase estimation for dual-polarization 16-QAM systems. *Opt. Express*, 19(22):21717–21729, Oct. 2011.
- [92] Kangping Zhong *et al.* Linewidth-tolerant and low-complexity two-stage carrier phase estimation based on modified QPSK partitioning for dual-polarization 16-QAM systems. *J. Lightw. Technol.*, 31(1):50–57, Jan. 2013.
- [93] Tao Yang *et al.* Linewidth-tolerant and multi-format carrier phase estimation schemes for coherent optical m -QAM flexible transmission systems. *Opt. Express*, 26(8):10599–10615, Apr. 2018.
- [94] Meng Xiang *et al.* Low-complexity feed-forward carrier phase estimation for M -ary QAM based on phase search acceleration by quadratic approximation. *Opt. Express*, 23(15):19142–19153, Jul. 2015.

- [95] Qunbi Zhuge *et al.* Low computation complexity two-stage feedforward carrier recovery algorithm for M-QAM. In *Proc. Opt. Fiber Commun. Conf.*, Mar. 2011, paper OMJ5.
- [96] Syed Muhammad Bilal *et al.* Dual stage CPE for 64-QAM optical systems based on a modified QPSK-partitioning algorithm. *IEEE Photon. Technol. Lett.*, 26(3):267–270, Feb. 2014.
- [97] Xiaofei Su *et al.* A multistage CPE scheme based on crossed constellation transformation for M-QAM. *IEEE Photon. Technol. Lett.*, 27(1):77–80, Jan. 2015.
- [98] Jie Feng *et al.* Carrier phase estimation for 32-QAM optical systems using quasi-QPSK-partitioning algorithm. *IEEE Photon. Technol. Lett.*, 28(1):75–78, Jan. 2016.
- [99] Jaime Rodrigo Navarro *et al.* High performance and low complexity carrier phase recovery schemes for 64-QAM coherent optical systems. In *Proc. Opt. Fiber Commun. Conf.*, Mar. 2017, paper W2A.53.
- [100] Rafael Rios-Müller *et al.* Spectrally-efficient 400-gb/s single carrier transport over 7200 km. *J. Lightw. Technol.*, 33(7):1402–1407, Apr. 2015.
- [101] Maxim Kuschnerov. Digital coherent transceivers: From algorithm design to economics. In *Proc. Opt. Fiber Commun. Conf.*, Mar. 2017, paper M2C.5.
- [102] Abdelkerim Amari *et al.* A survey on fiber nonlinearity compensation for 400 Gb/s and beyond optical communication systems. *IEEE Commun. Surveys Tuts.*, 19(4):3097–3113, Jun. 2017.
- [103] Syed Muhammad Bilal *et al.* Carrier phase estimation through the rotation algorithm for 64-QAM optical systems. *J. Lightw. Technol.*, 33(9):1766–1773, May. 2015.

- [104] Bell Canada. “Building a more resilient optical network,” 2017.
- [105] Bill Arnaud *et al.* Customer-controlled and -managed optical networks. *J. Lightw. Technol.*, 21(11):2804–2810, Nov. 2003.
- [106] Feng Lu *et al.* Power-division non-orthogonal multiple access (NOMA) in flexible optical access with synchronized downlink/asynchronous uplink. *J. Lightw. Technol.*, 35(19):4145–4152, Oct. 2017.
- [107] Qiong Wu *et al.* Digital domain power division multiplexed dual polarization coherent optical OFDM transmission. *Sci. Rep.*, 8(1):1–8, Oct. 2018.
- [108] Meng Xiang *et al.* Filtering tolerant digital subcarrier multiplexing system with flexible bit and power loading. In *Proc. Opt. Fiber Commun. Conf.*, Mar. 2017, paper W4A.7.
- [109] Hosein Nikopour *et al.* Sparse code multiple access. In *Proc. IEEE Pers. Indoor and Mobile Radio Commun.*, pages 332–336, Sep. 2013.
- [110] Mahmoud Taherzadeh *et al.* SCMA codebook design. In *Proc. IEEE Veh. Technol. Conf.*, pages 1–5, Sep. 2014.
- [111] Monirosharieh Vameghestahbanati *et al.* Multidimensional constellations for uplink SCMA systems—A comparative study. *IEEE Commun. Surveys Tuts.*, 21(3):2169 – 2194, Apr. 2019.
- [112] Xiang Lin *et al.* A Non-Data-Aided OSNR Estimation Algorithm for Coherent Optical Fiber Communication Systems Employing Multilevel Constellations. *J. Lightw. Technol.*, Jun. 2019.
- [113] Frank R Kschischang *et al.* Factor graphs and the sum-product algorithm. *IEEE Trans. Inf. Theory*, 47(2):498–519, Feb. 2001.

- [114] Ibrahim Al-Nahhal *et al.* Low-cost uplink sparse code multiple access for spatial modulation. *IEEE Trans. Veh. Technol.*, Jul. 2019, DOI: 10.1109/TVT.2019.2930285.
- [115] Fan Wei and Wen Chen. Low complexity iterative receiver design for sparse code multiple access. *IEEE Trans. Commun.*, 65(2):621–634, Feb. 2017.
- [116] FJ Vaquero Caballero *et al.* Machine learning based linear and nonlinear noise estimation. *J. Opt. Commun. Netw.*, 10(10):D42–D51, Oct. 2018.
- [117] Aazar Saadaat Kashi *et al.* Nonlinear signal-to-noise ratio estimation in coherent optical fiber transmission systems using artificial neural networks. *J. Lightw. Technol.*, 36(23):5424–5431, Dec. 2018.